The Astrophysical Journal, 698:865–894, 2009 June 10 doi:10.1088/0004-637X/698/1/865

HALO STREAMS IN THE SEVENTH SLOAN DIGITAL SKY SURVEY DATA RELEASE

R. Klement[1], H.-W. Rix[1], C. Flynn[2], B. Fuchs[3], T. C. Beers[4], C. Allende Prieto[5,6], D. Bizyaev[7], H. Brewington[7], Y. S. Lee[4], E. Malanushenko[7], V. Malanushenko[7], D. Oravetz[7], K. Pan[7], P. Re Fiorentin[1,8], A. Simmons[7], and S. Snedden[7]

[1] Max-Planck-Institut für Astronomie, Königstuhl 17, D-69117 Heidelberg, Germany; klement@mpia.de, rix@mpia.de
[2] Tuorla Observatory, V ais al antie 20, FI-21500 PIIKKI O, Finland; cflynn@utu.fi
[3] Astronomisches Rechen-Institut am Zentrum für Astronomie Heidelberg, Mönchhofstraße 12-14, D-69120 Heidelberg, Germany; fuchs@ari.uni-heidelberg.de
[4] Department of Physics and Astronomy, CSCE: Center for the Study of Cosmic Evolution, and JINA: Joint Institute for Nuclear Astrophysics, Michigan State University, E. Lansing, MI 48824, USA; beers@pa.msu.edu, lee@pa.msu.edu
[5] McDonald Observatory and Department of Astronomy, The University of Texas, 1 University Station, C1400, Austin, TX 78712-0259, USA; callende@astro.as.utexas.edu
[6] Mullard Space Science Laboratory, University College London, Holmbury St. Mary, Surrey RH5 6NT, UK
[7] Apache Point Observatory, Sunspot, NM 88349, USA; snedden@apo.nmsu.edu, dmbiz@apo.nmsu.edu, hjbrew@apo.nmsu.edu, viktorm@apo.nmsu.edu, elenam@apo.nmsu.edu, doravetz@apo.nmsu.edu, kpan@apo.nmsu.edu, asimmons@apo.nmsu.edu
[8] Department of Physics, University of Ljubljana, Jadranska 19, 1000 Ljubljana, Slovenia; paola.refiorentin@fmf.uni-lj.si
Received 2008 December 20; accepted 2009 April 1; published 2009 May 26

ABSTRACT

We have detected stellar halo streams in the solar neighborhood using data from the seventh public data release of the Sloan Digital Sky Survey (SDSS), which includes the directed stellar program Sloan Extension For Galactic Understanding and Exploration (SEGUE). In order to derive distances to each star, we used the metallicity-dependent photometric parallax relation from Ivezić et al. We examine and quantify the accuracy of this relation by applying it to a set of globular and open clusters observed by the SDSS/SEGUE and comparing the resulting sequence to the fiducial cluster sequences obtained by An et al. Our final sample consists of 22,321 nearby ($d \leqslant 2$ kpc), metal-poor ([Fe/H] $\leqslant -0.5$) main-sequence stars with six-dimensional estimates of position and space velocity ($\vec{r}, \vec{v}$). We characterize the orbits of these stars through suitable kinematic proxies for their "effective" integrals of motion, angular momentum, eccentricity, and orbital polar angle and compare the observed distribution to expectations from a smooth distribution in four [Fe/H] bins. The metallicities provide an additional dimension in parameter space that is well suited to distinguish tidal streams from those of dynamical origin. On this basis, we identify at least five significant "phase-space overdensities" of stars on very similar orbits in the solar neighborhood to which we can assign unambiguously peaked [Fe/H] distributions. Three of them have been identified previously, including the halo stream discovered by Helmi et al. at a significance level of $\sigma = 12.0$. In addition, we find at least two new genuine halo streams, judged by their kinematics and [Fe/H], at $\sigma = 2.9$ and 4.8, respectively. For one stream the stars even show coherence in the configuration space, matching a spatial overdensity of stars found by Juric et al. at $(R, z) \approx (9.5, 0.8)$ kpc. Our results demonstrate the practical power of our search method to detect substructure in the phase-space distribution of nearby stars *without* making a priori assumptions about the detailed form of the gravitational potential.

Key words: Galaxy: kinematics and dynamics – solar neighborhood

Online-only material: color figures

1. INTRODUCTION

The phase-space distribution of stars in the solar neighborhood encodes enormous amounts of information on the present dynamical state and the formation history of the Milky Way. A key role in this context is played by the existence of substructure in the phase-space distribution of stars, caused by stellar streams or moving groups, that is, groups of stars moving on similar orbits in the Milky Way's gravitational potential. Such moving groups have been known to exist in the velocity distribution of nearby stars for some time (Proctor 1869; Lindblad 1925; Eggen 1996, and references therein). Stellar streams, together with their chemical and dynamical properties, can be used to constrain various scenarios of the hierarchical buildup of the Milky Way (e.g., Helmi et al. 1999) as well as its gravitational potential (e.g., Antoja et al. 2008).

Moving groups in the solar neighborhood emerge for several reasons. The simplest case is an agglomeration of stars that were born in the same molecular cloud and only recently dissolved. In this case, the stars keep on moving in the direction of the once-bound cluster, until phase-mixing washes out their common orbital signature. While this scenario seems to be valid for some stellar streams (e.g., HR1614; De Silva 2007), the chemical and chronological properties of the largest moving groups are incompatible with it. For example, Chereul & Grenon (2001) reported an age range of 0.5 Gyr to more than 2–3 Gyr for Hyades supercluster, along with a rather large velocity dispersion, which they identified with the presence of several subgroups. Such subgroups have also been found by Dehnen (1998), who used subsamples of young and old stars based on their spectral types. He discovered an asymmetric drift relation for the moving groups, in the sense that those only present in the red subsamples (old stars) have larger radial velocity components, and lag with respect to the local standard of rest (LSR), than those also containing blue (younger) stars. In other words, old moving groups move on more eccentric orbits. To explain this observation, Dehnen (1998) proposed that these streams consist of stars that have been trapped onto nearly resonant orbits that oscillate about their parent resonant orbits, while the latter slowly change their eccentricity along with

the nonaxisymmetric potential. This interpretation is based on suggestions already made by Mayor (1972) and Kalnajs (1991). The latter tried to explain the bimodal velocity distribution of the Sirius (moving radially inward) and Hyades (moving radially outward) streams by putting the Sun at the position of the outer Lindblad resonance (OLR) of the Galactic bar. However, Famaey et al. (2004) later pointed out that these streams are better explained as stars on horseshoe orbits that cross-corotate in the rest frame of spiral density waves (for more details, see Sellwood & Binney 2002). They further argued that the clusters of coeval stars that have traditionally been connected to these streams would have been picked up by the spiral waves along with field stars of different ages, and therefore are just moving in these kinematic groups by chance. De Simone et al. (2004) also found that spiral waves can produce kinematic structures similar to those observed in the solar neighborhood, although they attributed this more to disk heating rather than radial migration.

Dehnen (2000) and Fux (2001) later used the position of the Hercules stream, which lags the LSR by $\sim$50 km s^{-1}, to constrain the inclination angle and position of the OLR of the Galactic bar. Similarly, Quillen & Minchev (2005) found that placing the Sun near the 4:1 inner Lindblad resonance with a two-armed spiral density wave could account for the velocity-space positions of the Hyades and Coma Berenices moving groups. Very recently, simulations of the birth and evolution of disk stars in a Milky Way potential including axisymmetric components for the disk, the bulge and halo, spiral arms, and a bar, were able to reproduce the shape of the Hercules, Coma Berenices, Hyades and Sirius moving groups in velocity space (Antoja et al. 2008). These examples show that the velocity distribution, as well as the age and chemical composition of dynamical streams in the solar neighborhood, can be used as tracers of the Galactic potential.

A third scenario for the formation of a stellar stream is a tidally disrupting cluster or satellite galaxy that deposits its debris on similar orbits (i.e., a "tidal" or "halo stream"). Helmi & White (1999) performed simulations of disrupting satellites crossing the solar neighborhood and showed that the debris loses its spatial coherence completely over a Hubble time. In contrast, the stream stars clump together in velocity space, resembling classical moving groups. The reason is that stars in a single stream obey the collisionless Boltzmann equation, a special case of Liouville's theorem, which states that the phase-space density of a stellar subpopulation is conserved at any given phase-space point. Initially, the stream stars are located in a small phase-space volume. However, as the spatial components of the stars disperse with time, they become more focused in their velocity components. Although in practice the velocity dispersion of a tidal stream tends to increase with time, due to the effect of phase mixing (Helmi & White 1999), such tidal streams will still form coherent features in velocity space, because to be in the solar neighborhood at the same time the azimuthal velocities of the stars must be similar. This has been confirmed with a number of different data sets, and stellar halo streams have been identified in the kinematic distribution of solar neighborhood stars (Helmi et al. 1999; Chiba & Beers 2000; Navarro et al. 2004; Arifyanto & Fuchs 2006; Helmi et al. 2006; Dettbarn et al. 2007; Klement et al. 2008, hereafter Paper I). Tidal streams also conserve the so-called integrals of motion of their progenitor, energy and angular momentum, allowing their recovery even if the halo has undergone complete mixing (Helmi & de Zeeuw 2000). Trying to confine Milky Way streams into a small range of energies could yield a best fit to the gravitational potential.

The primary goal of this paper is to search for substructure in the solar neighborhood that can be attributed to tidal halo streams. Helmi et al. (1999) predicted that $\sim$500 kinematically cold streams might exist in the solar neighborhood, yet only a few have been detected so far. Currently, however, the Sloan Digital Sky Survey (SDSS; York et al. 2000) and its extensions, which have thus far obtained spectra for over 400,000 stars, represent the most extensive database collected to date to increase the number of detected halo streams. As has been shown by simulations from various authors (e.g., Helmi & de Zeeuw 2000; Peñarrubia et al. 2006; Choi et al. 2007), a straightforward approach to finding stellar streams would be in the space of the integrals of motion (E, L, L_z), which are immune to phase mixing. In practice, however, the integrals of motion are not uniquely defined, because the potential is not exactly known. Furthermore, the error bars on six-dimensional measurements are drastically "anisotropic" across the different components. We therefore want to explore search strategies in a modified integrals-of-motion space that match the data and error bars.

This paper is organized as follows. Section 2 describes our data set, our methods for deriving distances, comparisons of our adopted photometric parallax relation with cluster fiducial sequences, and estimates of space velocities for the stars. Section 3 describes our strategy for searching for streams in the solar neighborhood. We apply our methods in Section 4, pointing out where several of our streams overlap with previously detected examples. We consider the potential effects of systematic distance errors in Section 5. Section 6 discusses our methods for the determination of the statistical significance associated with stream detection. In Section 7, we present four new likely streams and confirm the detection of three others identified in previous work (adding additional members to these structures). Our conclusions and a brief discussion are presented in Section 8.

2. THE DATA

SDSS-I was an imaging and spectroscopic survey that began routine operations in 2000 April and continued through 2005 June. The SDSS, and its extensions, uses a dedicated 2.5 m telescope (Gunn et al. 2006) located at the Apache Point Observatory in New Mexico. The telescope is equipped with an imaging camera and a pair of spectrographs, each of which is capable of simultaneously collecting 320 medium-resolution ($R = 2000$) spectra over the 7 deg^2 field of view (FOV), so that on the order of 600 individual target spectra and roughly 40 calibration-star and sky spectra are obtained on a given spectroscopic "plug-plate" (York et al. 2000). The imaging camera (Gunn et al. 1998) contains an imaging array of 30 4 megapixel CCDs and astrometric arrays that measure fluxes for calibration with standard astrometric catalog stars. The flux densities of objects observed are measured almost simultaneously in five bands [u, g, r, i, z], with effective wavelengths of [3540 Å, 4760 Å, 6280 Å, 7690 Å, 9250 Å], respectively (Fukugita et al. 1996; Gunn et al. 1998; Hogg et al. 2001). The camera sweeps the sky in great circles (in a drift scan mode) and a point on the sky passes the filters in the order of r, i, u, z, g. The brightness limit where the imaging camera saturates is at $g \sim 14$ mag. The completeness at this magnitude is $\sim$99.3% for point sources (Ivezić et al. 2001); it drops to 95% at magnitudes of [22.1, 22.4, 22.1, 21.2, 20.3].[9] The SDSS photometry is accurate to

[9] These values have been derived by comparing multiple scans of the same area obtained during the commissioning year with a typical seeing of $1\farcs5 \pm 0\farcs1$.

0.02 mag rms at the bright end,[10] with well controlled tails of the error distribution (Ivezić et al. 2003). Astrometric positions are accurate to about 0.″1 per coordinate for sources brighter than $r \sim 20.5$ mag (Pier et al. 2003). Morphological information from the images allows point source–galaxy separation to $r \sim 21.5$ mag (Lupton et al. 2002).

One of three subsurveys carried out during the first extension of the SDSS, known as SDSS-II, the Sloan Extension for Galactic Understanding and Exploration (SEGUE), ran from 2005 July to 2008 June. SEGUE obtained some 250,000 medium-resolution spectra of stars in the Galaxy, selected in order to explore the nature of stellar populations from 0.5 kpc to 100 kpc (Yanny et al. 2009). These data, along with the substantial numbers of suitable stars observed during the course of SDSS-I, allow the derivation of the full six-dimensional phase-space distribution of the various components of the Milky Way. Stellar physical parameters ($T_{\rm eff}$, $\log g$, [Fe/H]), based on SDSS photometry and spectroscopy, are derived by the application of the SEGUE Stellar Parameter Pipeline (SSPP) described by Lee et al. (2008a, 2008b) and Allende Prieto et al. (2008).

We start the sample selection for the present study from all stars targeted for spectroscopy by SDSS/SEGUE with a signal-to-noise ratio (S/N) greater than 10, accepted photometry in all five bands, and estimates for the radial velocity, [Fe/H], and proper motions. Note that the requirement for determinations of [Fe/H] is essentially one on effective temperature (or color), as the present SSPP provides confident estimates of metallicity over the range 4500 K $\leqslant T_{\rm eff} \leqslant$ 7500 K. These stars have been taken from the seventh data release (Abazajian et al. 2009); their proper motions have been corrected for a systematic error that occurred in the data reduction procedure (Munn 2008). There are a number of repeated observations, either for quality assurance or from reuse of photometric calibration stars by several plug-plates. These repeats are independent observations and are listed separately in the SDSS Catalog Archive Server, with different identification numbers. We only keep one object per position on the sky, to which we assign a radial velocity and stellar parameters averaged over all repeats. Figure 1 shows the sky coverage of the resultant sample of 154,888 stars. These data cover a large, almost contiguous area in the Northern Galactic Cap plus three stripes in the South Galactic Cap.

2.1. Distance Estimates

The majority of stars spectroscopically targeted by SDSS-I are main-sequence stars (or metal-poor main-sequence turnoff stars used as calibration objects; ∼99%; Finlator et al. 2000). Although the targets spectroscopically selected by SEGUE explicitly include giants, their fraction (based on spectroscopic surface gravity estimates) remains low. Only 8.8% of these stars have $\log g < 3.5$, the surface gravity where we divide between dwarfs and giants. This is a bit more stringent than the separation made, for example, by Ivezić et al. (2008) at $\log g = 3$, but we wish to ensure that only late-type dwarfs and subdwarfs are selected.[11] Presuming a sample dominated by main-sequence stars, we can apply a photometric parallax relation to derive distances. Because we want to concentrate on a wide range of metal-poor stars, the effect of metallicity

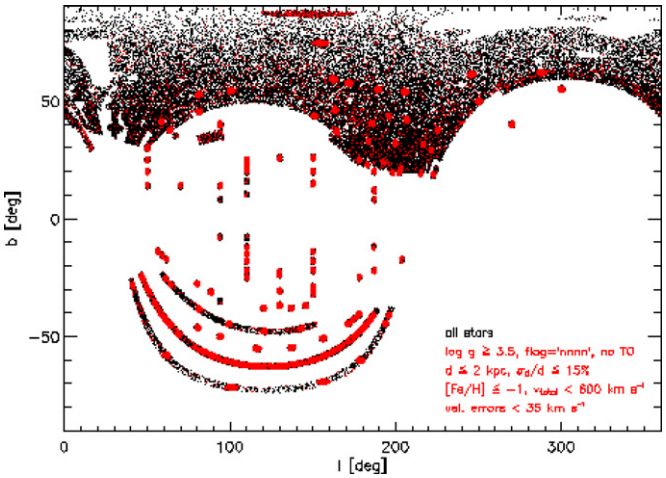

Figure 1. Sky coverage of our sample of SDSS/SEGUE stars. Each star is plotted individually. The red data points represent the positions of metal-poor stars that meet the selection criteria of our final sample (see Section 2.2). Note the sparse sampling obtained during SDSS-I vs. the focused sampling of the SDSS-II/SEGUE pointings.

on the absolute magnitude at a given color becomes important. We have spectroscopic metallicities available for each star, so we are motivated to adopt a photometric parallax relation that explicitly accounts for metallicity over a wide range of colors.

Such a relation has been derived by Ivezić et al. (2008). The shape of their color–magnitude relation, $M_r^0(g-i)$, is constrained by simultaneously fitting SDSS photometry data for five globular clusters, normalized to the same arbitrary magnitude scale by requiring the same median magnitude ($r = 0$) for stars in the color range $0.5 < g-i < 0.7$. By assuming that this shape depends only on color, and not metallicity, and its normalization depends only on metallicity, and not color, the absolute magnitude offset of each cluster from the mean relation can be expressed as a function of metallicity. The absolute magnitude of a star is then calculated as

$$M_r(g-i, [\mathrm{Fe/H}]) = M_r^0(g-i) + \Delta M_r([\mathrm{Fe/H}]). \quad (1)$$

With distances adopted from Harris (1996) and six additional open and globular cluster data from Vandenberg & Clem (2003), they derive the following absolute magnitude correction:

$$\Delta M_r([\mathrm{Fe/H}]) = 4.50 - 1.11[\mathrm{Fe/H}] - 0.18[\mathrm{Fe/H}]^2. \quad (2)$$

The correction (Equation (2)) suggests an offset from the mean relation of 4.5 for solar metallicity stars, due to the scaling to $r = 0$ described above. Ivezić et al. (2008) further expanded the mean photometric parallax relation to the color range $0.2 < g-i < 4.0$ by using constraints from trigonometric parallaxes given in Bochanski et al. (2008), additional cluster data observed in the SDSS from Clem et al. (2008), and an age correction for turnoff stars. The result is a fifth-order polynomial:

$$M_r^0(g-i) = -5.06 + 14.32(g-i) - 12.97(g-i)^2 + 6.127(g-i)^3 - 1.267(g-i)^4 + 0.0967(g-i)^5, \quad (3)$$

which, together with Equations (1) and (2), is our adopted photometric parallax relation.

We test the validity of this relation for our sample using different approaches, as described below.

[10] This value is determined using repeated observations of 3,000,000 point sources over time spans ranging from 3 hr to three years.

[11] A subdwarf is defined as a star with luminosity 1.5–2 mag lower than that of a solar-metallicity main-sequence star of the same spectral type.

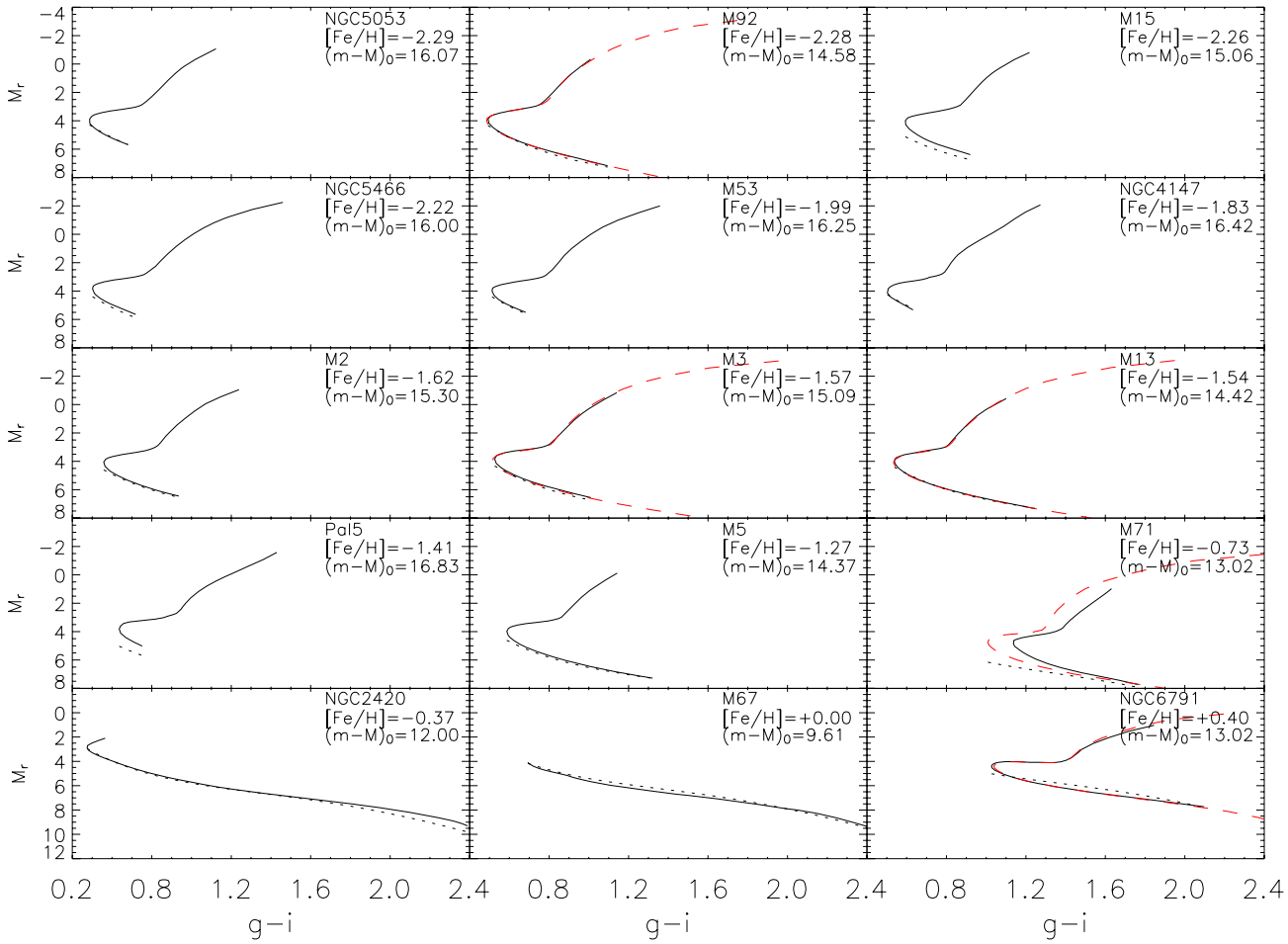

Figure 2. Comparison of cluster fiducial sequences taken from An08 (solid black lines) and Clem et al. (2008; dashed red line), respectively, and the [Fe/H]-dependent photometric parallax relation from Ivezić et al. (2008; dotted line). The panels show the absolute magnitude, M_r, as a function of the $g - i$ color. The adopted distance moduli and metallicities are taken from various sources in the literature (see An08, Section 2, for all references).

(A color version of this figure is available in the online journal.)

2.1.1. Comparison of the Photometric Parallax Relation with Cluster Fiducial Sequences

An et al. (2008, hereafter An08) have used crowded-field photometry techniques to analyze SDSS/SEGUE imaging data for 17 globular and three open clusters, and determined fiducial sequences from their color–magnitude diagrams (CMDs). These sequences give the r-band magnitude as a function of either $u-g$, $g-r$, $g-i$, or $g-z$ color. This is the first time that cluster fiducial sequences have been evaluated in the native SDSS $ugriz$ system, allowing for tests of the photometric parallax relation from Ivezić et al. (2008) without the need to rely on color transformations from other systems.

We use 15 of the cluster fiducials and compare them to the sequences derived from Equations (1)–(3). In addition, we consider the fiducial sequences from Clem et al. (2008) for five clusters, after transforming them onto the $ugriz$ system using the transformations given by Tucker et al. (2006). These sequences have been shown to match the An08 fiducials within the errors of the photometric zero points. Because they were obtained from observations with various integration times, the Clem et al. sequences extended over a broader magnitude range than the An08 sequences. We calculated the absolute magnitude, M_r, for each cluster by adopting the distance moduli and metallicities as given in An08. The results are shown in Figure 2, sorted by decreasing cluster metallicity.

For most of the clusters, the photometric parallax relation of Ivezić et al. (2008) fits the fiducial main sequences remarkably well. In the case of nearly all the metal-poor clusters with [Fe/H] < -1.0, the difference between the absolute magnitude predicted by the photometric parallax relation, $M_{r,\mathrm{phot}}$, and the absolute magnitude given by the cluster fiducial sequences, $M_{r,\mathrm{cluster}}$, stays below ∼0.2 mag for $g - i \gtrsim 0.4$. There are three exceptions to this trend. One is M15, where the turnoff is slightly redward of $g - i = 0.4$ and the absolute magnitude offset drops roughly from $M_{r,\mathrm{phot}} - M_{r,\mathrm{cluster}} = 0.48$ mag at $g - i = 0.51$ to 0.36 mag at $g - i = 0.77$. For Palomar 5, the discrepancy is more than 0.7 mag across the main sequence. However, this cluster is known to be in the process of tidal disruption (Odenkirchen et al. 2001; Grillmair & Dionatos 2006) and is sparsely populated in the observations; contamination by foreground and background stars is possible. Also, the color range spanned by the main sequence is very small compared with the giant branch, and it may not extend far enough from the turnoff for the photometric parallax relation to be valid. The An08 fiducial sequence for M71 has to be taken with caution, because according to these authors the zero points for the M71 photometry were very uncertain, and there was a strong contamination by likely background stars. The uncertain fiducial sequence could thus account for the offsets.

We find it more descriptive to express the systematic differences between the photometric parallax relation and the cluster

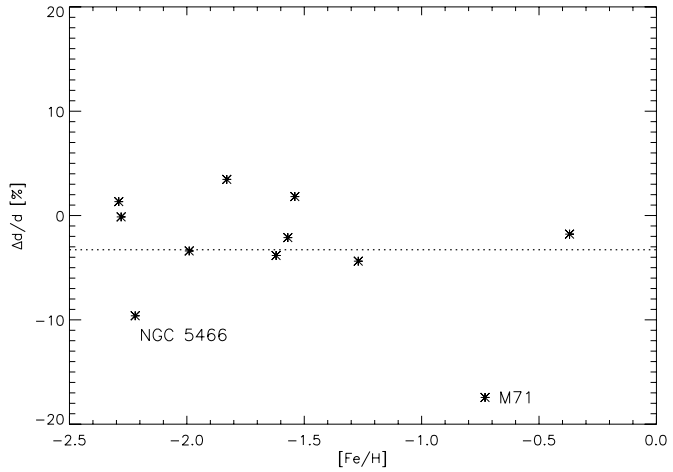

Figure 3. Relative distance errors, $\Delta d/d = (d_{\rm phot} - d_{\rm cluster})/d_{\rm cluster}$), vs. metallicity, [Fe/H], derived from 11 of the 13 clusters that lie in the metallicity range $-2.0 < {\rm [Fe/H]} < -0.3$. The errors of each cluster have been averaged over the color range $(g-i)_{\rm TO} + 0.05 < g-i < 1.5$. The two clusters M15 and Pal5 have not been considered, while M71 has been kept, because it has a sequence measured by Clem et al. (2008) with deep photometry. The dotted line indicates the distance offset averaged over all 11 clusters (including M71), which we adopt as the systematic distance error for the Ivezić et al. (2008) photometric parallax relation.

fiducial sequences through a distance offset rather than a magnitude offset. To derive an estimate of the systematic distance error of the photometric parallax relation, we average over the differences between the distance that is predicted by the relation, $d_{\rm phot}$, and the distance given by the distance modulus of each cluster, $d_{\rm cluster}$. To this end, we concentrate on the color range $(g-i)_{\rm TO} + 0.05 < g-i < 1.6$, where $(g-i)_{\rm TO}$ denotes the turnoff color, that is, the color at which a cluster's main sequence runs vertically.[12] The color $g-i = 1.6$ corresponds approximately to the reddest color in our sample. If available, we prefer the cluster sequences of Clem et al. (2008) for calculating $\Delta d/d$. After elimination of the two outliers mentioned above (M15 and Pal5), Figure 3 shows relative distance errors $\Delta d/d = (d_{\rm phot} - d_{\rm cluster})/d_{\rm cluster}$) over the range in metallicity $-2.0 < {\rm [Fe/H]} < -0.3$. Nine of the 11 cluster sequences considered suggest very small systematic errors, while the distances to NGC5466 and M71 are underestimated by 9.61% and 17.44%, respectively. Averaging over all clusters, the systematic distance error is

$$\left\langle \frac{\Delta d}{d} \right\rangle = \begin{cases} -3.28\% \pm 1.78\% & \text{including M71,} \\ -1.86\% \pm 1.19\% & \text{excluding M71.} \end{cases} \quad (4)$$

We found no indication in Clem et al. (2008) that their sequence for M71 might be unreliable, so we will use the more conservative value of −3.28% when considering the effects of velocity errors on our results. This value is indicated by the dotted line in Figure 3.

The photometric parallax relation of Ivezić et al. (2008) is constructed from stars that are redder than the main-sequence turnoff. Although the authors included a correction for age effects, and stated that their formula is valid over the color range $0.2 < g-i < 4.0$, we see from Figure 2 that the application of the relationship breaks down near the turnoff, the color of which depends on both metallicity and cluster age. Metal-poor F-type stars in the disk, for example, have a lifetime considerably shorter than the age of the thin disk and are already in the turnoff phase. Having turnoff stars in our sample can result in additional systematic distance (and hence velocity) errors, which could lead to false stream detections. Theoretical isochrones could be used to determine the color at which stars of a given metallicity and age are in the turnoff phase. For example, the Girardi et at. (2004) *ugriz* isochrones predict a turnoff color of $g-i \approx 0.36$ (0.22) for a 13.5 Gyr old stellar population with [Fe/H] = −1.0 (−2.0). However, An08 have shown that the theoretical isochrones of Girardi et at. (2000) are not consistent with their fiducial sequences; the model colors for the main sequence are 2%–5% too blue. Therefore, we apply a color cut to our sample that is based on the location of the turnoff and the behavior of the distance errors in Figure 2 rather than on theoretical models.

We apply a stringent color cut in order to remove turnoff stars. We choose the color cuts depending on the metallicity of the stars as follows:

$$g-i \geqslant \begin{cases} 0.55 & \text{if} \quad {\rm [Fe/H]} > -1.0 \\ 0.50 & \text{if} \quad -1.5 < {\rm [Fe/H]} \leqslant -1.0 \\ 0.45 & \text{if} \quad -2.0 < {\rm [Fe/H]} \leqslant -1.5 \\ 0.40 & \text{if} \quad {\rm [Fe/H]} \leqslant -2.0. \end{cases} \quad (5)$$

These color cuts ensure that we select stars that are at least 0.05 mag redward of the cluster turnoffs in the corresponding metallicity bins. We do not use stars from the most metal-rich bin for our stream search, so we do not divide this bin further. The color cut, however, should be valid for stars up to solar metallicity. For reference, the Sun (a G2 star) has a $g-i$ color of 0.57±0.02 (as measured from about 50 solar analogs; Holmberg et al. 2006).

To summarize, the photometric parallax relation from Ivezić et al. (2008) performs very well in fitting the main sequences for clusters with metallicities of [Fe/H] $\lesssim -0.3$. On average, it predicts distances that are incorrect by −3.28% ± 1.78%. We thus adopt it to determine distances to all the dwarfs and subdwarfs ($\log g > 3.5$) in our sample. For more metal-rich clusters ([Fe/H] $\gtrsim -0.3$) the uncertainties are generally higher, although they can vary along the main sequence. Further investigations with a larger number of clusters will be needed in order to better determine the accuracy of the relation for metal-rich stars.

2.1.2. Three-Dimensional Velocities from $v_{\rm rad}$, $d_{\rm phot}$, and $\vec{\mu}$

From the photometric parallax relation, Equations (1)–(3), and the dereddened *r*-band magnitudes, we calculate the distance to each star via

$$d({\rm kpc}) = \frac{1}{100} \times 10^{0.2(r-M_r)}. \quad (6)$$

We calculate the statistical distance error from Gaussian error propagation:

$$\sigma_d = \frac{1}{5} d \ln 10 \sqrt{(\sigma_r)^2 + (\sigma_{M_r})^2}, \quad (7)$$

where σ_r is given for each star in our sample. The estimated dispersion in the absolute magnitude, σ_{M_r}, follows from Equations (1)–(3), and the listed errors for [Fe/H] and $g-i$. The mean statistical relative distance error of our sample is 7.58% ± 0.01%. An intrinsic (systematic) scatter of 3.28% (Equation (4)) is less than half of this value, and can be neglected relative to the statistical errors (see Section 5). Later,

[12] This is the bluest color for which a value of the fiducial sequence exists.

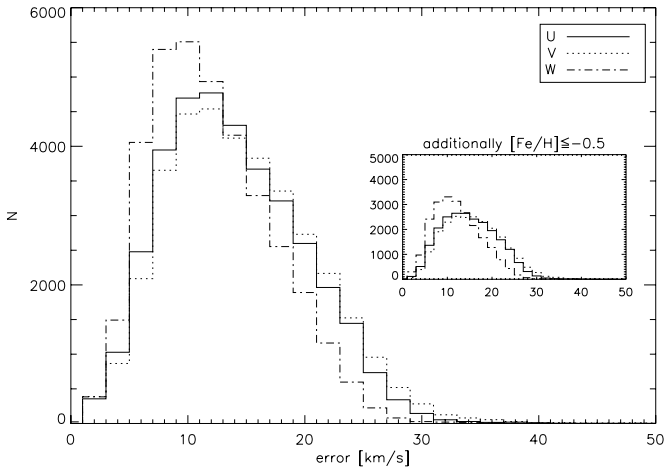

Figure 4. Distribution of errors for the velocity components U (solid), V (dotted), and W (dash-dotted) for all stars with flag = "nnnn," $\log g \geqslant 3.5$, $d \leqslant 2$ kpc, and $\frac{\sigma_d}{d} \leqslant 15\%$. The small window shows the same distribution, exclusively for stars with the additional restriction [Fe/H] $\leqslant -0.5$.

we restrict our selection to stars with statistical distance errors $\frac{\sigma_d}{d} \leqslant 15\%$ and distances $d \leqslant 2$ kpc, so in the worst case, when we add statistical and systematic errors, the actual distance could be 2.37 kpc instead of 2 kpc (with a total distance error of 28.28%).

Figure 4 shows the statistical velocity error distribution for 37,136 stars satisfying the SSPP flag = "nnnn" (indicating no peculiarities), $\log g \geqslant 3.5$, $d \leqslant 2$ kpc, $\sigma_d/d \leqslant 15\%$, and our color cuts (Equation (5)). Additionally, we show in the small window all 23,512 stars that also fulfill [Fe/H] $\leqslant -0.5$, because we cut at this metallicity for our final sample of metal-poor stars. The velocities and their errors have been calculated using the equations given in Paper I, Section 2.

The velocity error distribution rises to a peak around 10 km s^{-1} for W, and around 12–15 km s^{-1} for U and V and then falls off quickly. If we only select metal-poor stars from the above sample, the error distribution for U and V shifts to a peak around 13–15 km s^{-1}. For W, the errors increase only slightly. This follows since the more metal-poor stars are on average farther away. We choose to accept errors up to 35 km s^{-1} for all three velocity components.

2.2. A Sample of Metal-Poor Stars Within 2 kpc with Six-Dimensional Phase-Space Coordinates

In order to obtain the best available sample of stars, regarding the accuracy of distances and suitability for our stellar stream search, we only keep stars satisfying the following criteria (the number in parentheses indicates the number of stars that are left after each step):

1. $\log g \geqslant 3.5$, in order to only select dwarfs and subdwarfs to which we can apply the photometric parallax relation (141,286);
2. SSPP flag = "nnnn," indicating that there are no suspected problems with derived atmospheric parameters (118,584);
3. distance $d \leqslant 2$ kpc, because our search strategy requires nearby stars; also, the proper motions are more accurate for nearby stars (44,484);
4. relative distance errors $\sigma_d/d \leqslant 0.15$ (44,087);
5. total space velocity $v_{\rm total} < 600$ km s^{-1}, to exclude stars with apparently false proper motion measurements or distance estimates (44,034);
6. velocity errors smaller than 35 km s^{-1} for U, V, and W (43,512);
7. $g-i \geqslant (g-i)_{\rm TO}$, where $(g-i)_{\rm TO}$ depends on the metallicity of a star according to Equation (5), to exclude turnoff stars (35,864);
8. we restrict ourselves to [Fe/H] $\leqslant -0.5$, because we concentrate on thick-disk and halo substructure[13] (22,321).

A distance cut of 2 kpc is necessary, because our search strategy for streams assumes a constant rotation curve in the solar neighborhood, and that we can approximate the radial and rotational velocities by U and V, respectively. In addition, we gain higher accuracy in the velocities, because the proper motions are more accurate for nearby stars. The spatial distribution of our sample is shown in Figure 1 as the red dots. As can be appreciated by inspection of this figure, our sample is distributed over the same region as the full DR-7 sample.

Although our final sample is only 14% of the original 154,888 stars, we have a sample of nearby metal-poor stars of both unprecedented quantity and quality (compare to, e.g., Helmi et al. 1999; Chiba & Beers 2000; Arifyanto & Fuchs 2006; Dettbarn et al. 2007). Figure 5 shows the color, distance, and metallicity distribution of our final sample. The distribution peaks at $g-i = 0.7$ (the color of a G star) with a tail extending to $g-i \approx 1.3$ (K6–K7 stars). It is interesting that there remain some possible turnoff stars in the $g-r$ distribution at $g-r \approx 0.3$ for the most metal-rich bin ($-1.0 <$ [Fe/H] $\leqslant -0.5$),[14] although this is not the case in the $g-i$ distribution. The $g-i$ color has (somewhat) better signal-to-noise properties than the $g-r$ color, except in the region of the main-sequence turnoff (Ivezić et al. 2008). In any case, the fraction of possible turnoff stars is so small that the influence of their systematically incorrect distances on our analysis can be neglected.

3. SEARCH STRATEGY FOR STREAMS

To search for stellar halo streams in our sample, we effectively look for overdensities in eccentricity-, orbital inclination-, and guiding center radius- (or, equivalently, angular momentum-) space. We adopt a method based on the Keplerian approximation of Dekker (1976) and outlined by Dettbarn et al. (2007). This method is a generalization of the formalism outlined in Paper I to identify stellar streams in RAVE data. There it was assumed that the azimuthal velocity of a star could be approximated by $V + V_{\rm LSR}$, thereby projecting the orbits into the meridional plane. Halo stars move on random, more eccentric orbits, and we can apply the same formalism if we group them together according to the inclination of their orbital planes.

We assume a spherical potential and neglect any asphericity of the dark-halo potential and flattening of the disk potential. This is justified by the work of Chiba & Beers (2000), who showed that the distribution of halo stars in the space spanned by isolating integrals of motion in an *aspherical* Stäkel-type potential can be closely mapped into the integrals of motion space of a *spherical* potential. Also, even for stars that move in axisymmetric flattened potentials, $L_\perp$ is approximately conserved, and the orbits can be thought of as planar orbits precessing slowly around the z-axis (Binney & Tremaine 1987). As an example we refer to Paper I, where it was shown that stellar thick- and

[13] Also, higher metallicities are unreliable because of a calibration error that has only been fixed recently, and was not corrected in the Catalog Archive Server at the time we selected our stars (T. Beers 2008, private communication).

[14] For the more metal-poor bins, the turnoff lies blueward of $g-r = 0.3$.

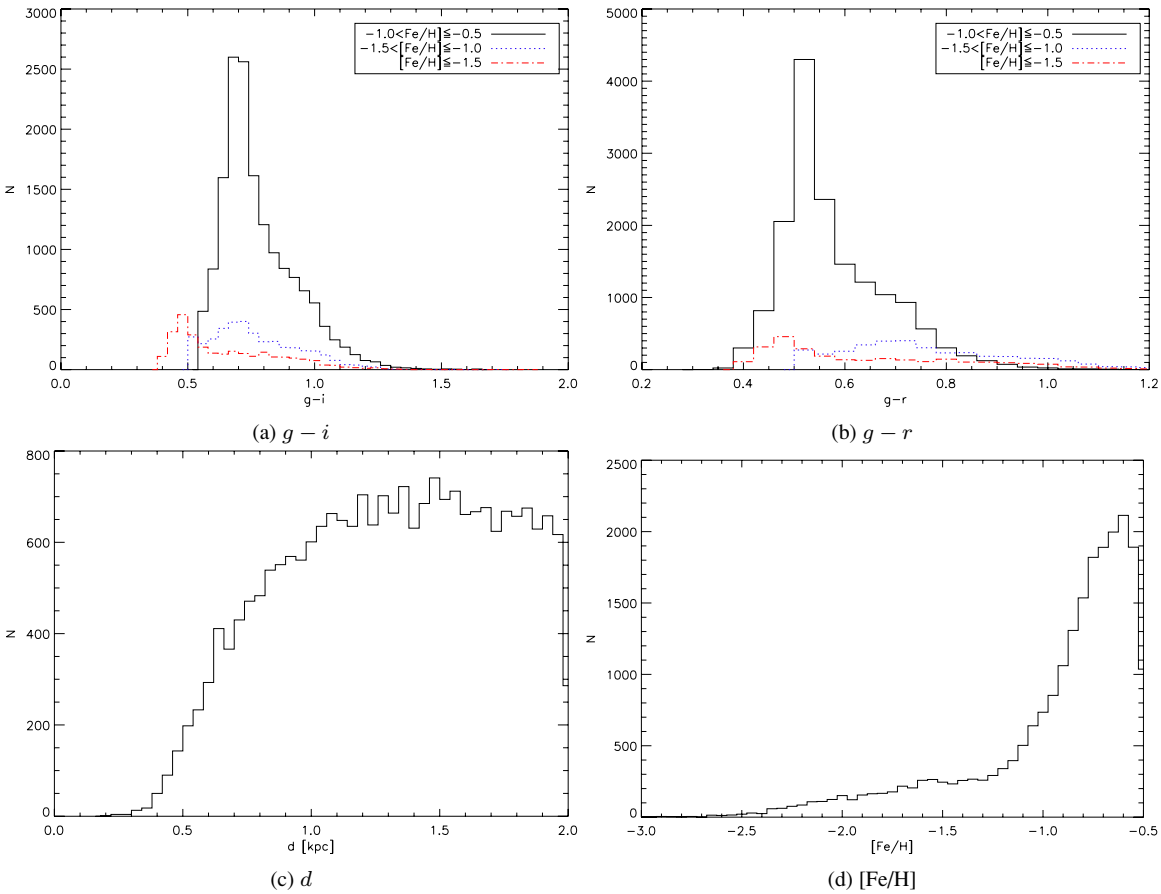

(a) $g-i$ (b) $g-r$ (c) d (d) [Fe/H]

Figure 5. Distribution of stars from our final sample in (a) colors $g-i$, (b) $g-r$, (c) distance d, and (d) metallicity [Fe/H]. Because of the applied color cuts, the sample consists of G- and K-type stars. Panels (a) and (b) display the color distribution for three bins in [Fe/H]. The different panels show that our sample is dominated by stars of the thick-disk population.

(A color version of this figure is available in the online journal.)

thin-disk streams detected in a projection of phase space are also clumped in $(L_z, L_\perp)$ space.

In a spherical potential, a star with Cartesian velocity components (U, V, W) moves in a fixed orbital plane that is inclined by an angle ν relative to the direction toward the North Galactic Pole. The angle ν is given by

$$\nu = \arctan\left(\frac{V + V_{\rm LSR}}{W}\right), \tag{8}$$

and ranges from 0° to 180°. Stars with polar angles $\nu > 180^\circ$ are treated as moving on retrograde orbits in a plane with polar angle $\nu - 180^\circ$. The azimuthal velocity of a star is

$$V_{\rm az} = \sqrt{(V + V_{\rm LSR})^2 + W^2}, \tag{9}$$

so if the star is near the Sun we can approximate its total angular momentum by

$$L = R_\odot \cdot V_{\rm az} = R_0 \cdot V_{\rm LSR}. \tag{10}$$

For the last step, we have assumed a constant rotation curve. Finally, we express the eccentricity, e, of any stellar orbit as

$$e = \frac{1}{\sqrt{2} V_{\rm LSR}} V_{\Delta E}, \tag{11}$$

where we have introduced the quantity

$$V_{\Delta E} = \sqrt{U^2 + 2(V_{\rm LSR} - V_{\rm az})^2}. \tag{12}$$

The parameter $V_{\Delta E}$ parametrizes the difference between the energy of a star at the guiding center of its orbit and at the solar radius, and is a measure of its orbital eccentricity. Also, we have shown (B. Fuchs, unpublished) that $V_{\Delta E}$ is related to the radial action integral, and is robust against slow changes in the gravitational potential.[15] Although the approximation 11 formally breaks down for highly eccentric orbits ($e > 0.5$ Dekker 1976), stars on similar orbits will still be projected into the same region of phase space (Klement 2009). Looking for "overdensities" in $(V_{\rm az}, V_{\Delta E}, \nu)$ space is a practical way to find stellar streams, because we do not need to assume any expression for the gravitational potential and any prehistory of the stream. The first successful application of the generalized Keplerian approximation was by Dettbarn et al. (2007), who were able to rediscover the "H99" stream, originally found by Helmi et al. (1999) in the $(L_z, L_\perp)$ space.

We use metallicities [Fe/H] to discriminate between stellar populations with different origins. We divide our sample into four subsamples (hereafter s1, s2, s3, s4) with decreasing metallicity:

1. s1: $-1.0 <$ [Fe/H] $\leqslant -0.5$ (15,856),
2. s2: $-1.5 <$ [Fe/H] $\leqslant -1.0$ (3676),

[15] Using Dekker's (Dekker 1976) theory of Galactic orbits, the radial action integral can be expressed in the notation of Arifyanto & Fuchs (2006) as

$$J_R = -\sqrt{2}\pi R_0^2 \kappa_0 + \frac{\pi R_0^3 \kappa_0^2}{\sqrt{E_0 - E + \frac{1}{2} R_0^2 \kappa_0^2}} \approx \frac{\pi R_\odot}{2 V_{\rm LSR}} V_{\Delta E}^2. \tag{13}$$

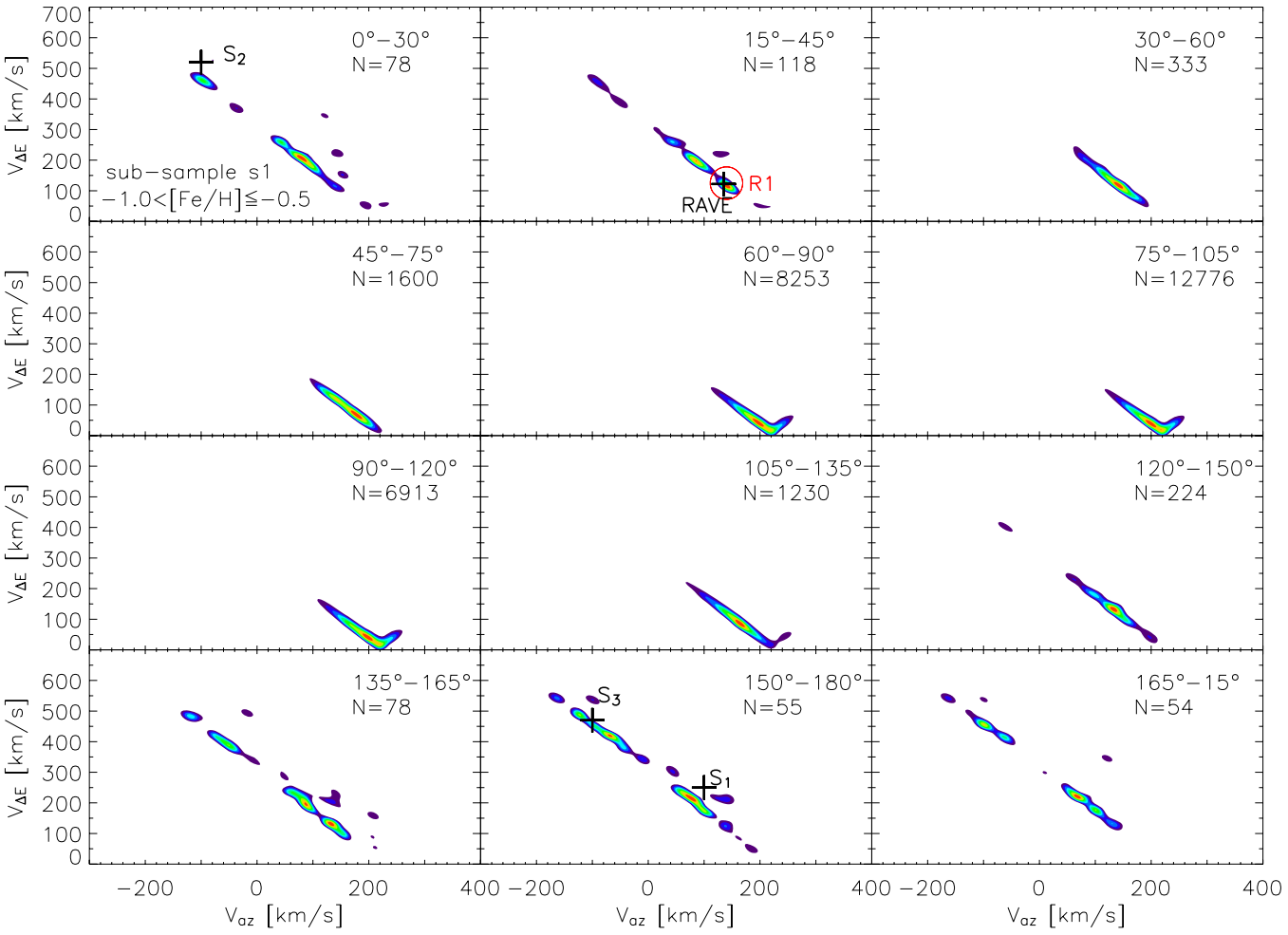

Figure 6. Wavelet transform of the distribution of SDSS stars from the metallicity subsample s1 (see text for definition) in (V_{az}, $V_{\Delta E}$) space, shown in bins of different orbital polar angles. The contours in each ν-bin range from 10% to 100% of the maximum value of the wavelet transform, and are color coded accordingly from purple to red (see Figure 10 for the colorbar). We have marked the positions of known stellar streams given in Table 1 with thick crosses and circled in red overdensities. See Section 7 for discussion.

3. s3: $-2.0 <$ [Fe/H] $\leqslant -1.5$ (1931),
4. s4: [Fe/H] $\leqslant -2.0$ (858).

The number in parenthesis is the number of stars in the corresponding subsample. We note that the typical metallicity estimates are uncertain to (at best) ∼0.25 dex, making adjacent subsamples not entirely independent. For each [Fe/H] bin, we collect the stars with similar orbital polar angles in small ν-slices. We bin the polar angles into 30° wide bins that overlap by 15°, thereby reducing bin-boundary effects on the results. We conduct the search for stellar streams within each ν-slice in the space spanned by angular momentum and eccentricity or (V_{az}, $V_{\Delta E}$). To amplify the overdensities, we use a wavelet transform technique with a skewed Mexican-hat-shaped analyzing wavelet (see Paper I for more details). We set the scale parameter of the wavelet to $a = 12$ km s^{-1}, comparable to the velocity errors, set the elongation parameter to $q = \sqrt{3}$, and employ cells in the (V_{az}, $V_{\Delta E}$) space of 3 km s^{-1} width on each side. The resulting contours of the wavelet transform are shown in Figures 6–9.

4. PLACING SOLAR NEIGHBORHOOD STREAMS IN THE (V_{az},$V_{\Delta E}$)-PLANE

As a first step in the analysis of the SDSS data, we explore whether we can find evidence in these data of the known streams believed to be of a tidal origin. We have taken the velocities of known halo streams from the literature and evaluated their velocities V_{az}, $V_{\Delta E}$, and orbital inclinations, ν. The results are given in Table 1 and marked with thick crosses in Figures 6–9. The feature marked "S_2,' found by Dettbarn et al. (2007) as an overdensity of stars in the (V_{az}, $V_{\Delta E}$,ν) space, has almost exactly the same properties as the "ω Cen"-stream; in fact, the signal of "S_2" in Figure 3 of Dettbarn et al. (2007) is extended across the ν range from 0 to ∼20°. Therefore, it is likely that "S_2" is in fact the "ω Cen"-stream, and we only label "ω Cen" in the plots.

We find strong evidence of the "H99," "S_3," and "RAVE" streams, which we discuss more in Section 7, but little or only minor hints for the existence of the other known streams.

5. THE EFFECTS OF SYSTEMATIC DISTANCE ERRORS AND UNRESOLVED BINARIES

To test for the possible effects of systematic distance errors on our results, we have added the −3.28% systematic distance error that we found through comparison of the photometric parallax relation to cluster fiducial sequences in Section 2.1.1 to each star and then recalculated their velocities and the wavelet transform for a subset of stars. As expected, the effect of the additional −3.28% errors is to slightly change the shape and

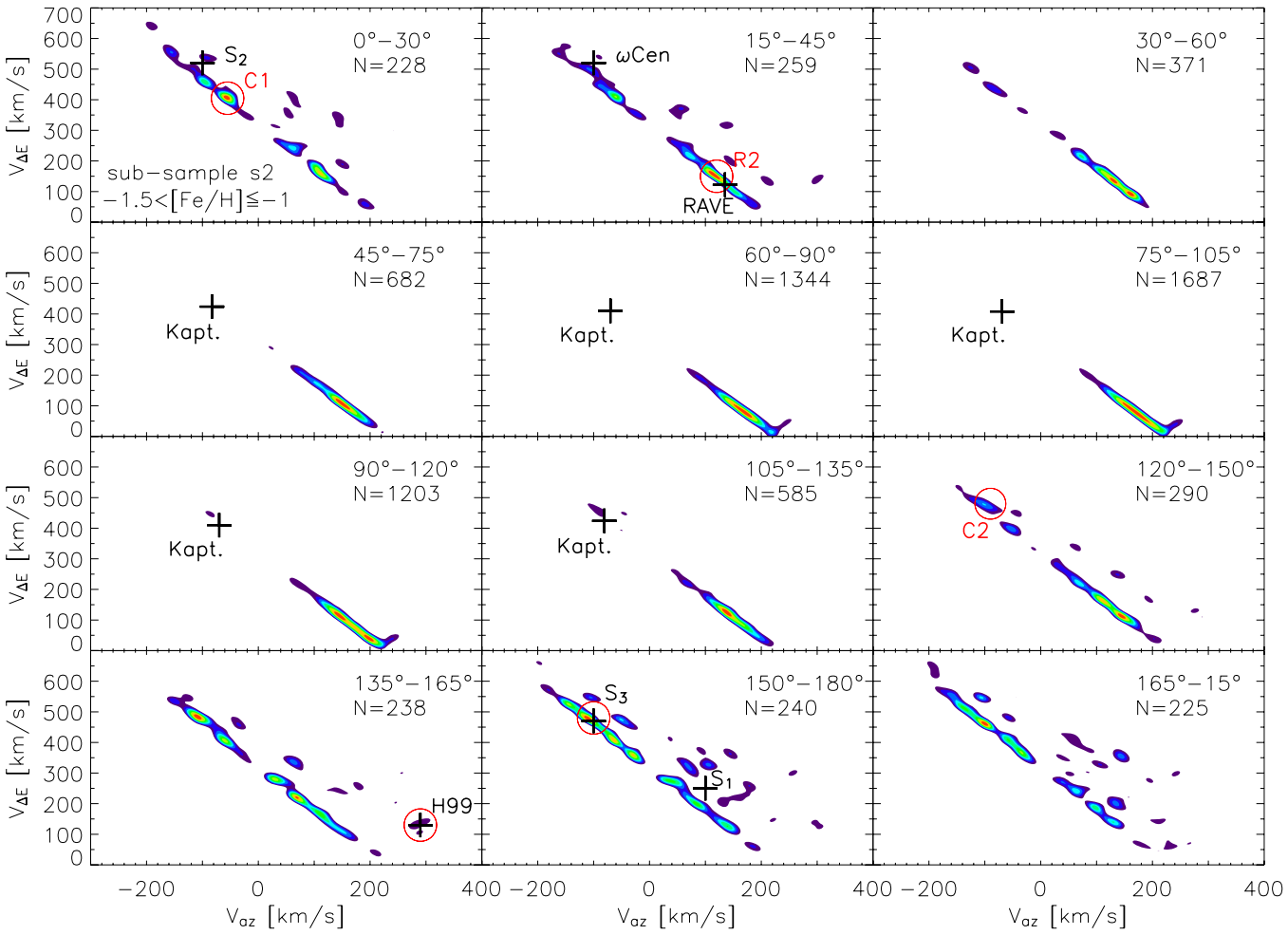

Figure 7. Same as Figure 6, but now for stars in the metallicity subsample s2.

relative "height" of some features, but the location of the overdensities does not change much. However, we also want to test if a much higher systematic error—say, −10%—would effect the location of the overdensities. While we have shown in Section 2.1.1 that a −10% error is very unlikely at the low-metallicty end of the photometric parallax relation, the error at the high-metallicity end ([Fe/H] $\gtrsim -1.0$) is much less constrained and a possibility for systematic errors on that level exists. This in turn may cause an overdensity that has a range of metallicities to be detected at varying positions in the ($V_{\rm az}$, $V_{\Delta E}$)-plane in different metallicity subsamples and be misinterpreted as multiple, adjacent, streams. As an example, Figure 10 shows contours of the wavelet transform for the distribution of stars from subsample s1 in the ν-slice 15°–45° (a) without and (b) with additional −10% distance errors. While the features remain close to their locations in ($V_{\rm az}$, $V_{\Delta E}$), they change their shape and relative "height." We have investigated other subsamples and ν-slices by adding similar distance errors (from 7% to 10%) and found that the change in relative height of the overdensities is more prominent for stars on retrograde orbits. However, such stars are more represented in the lower metallicity bins, where we expect the systematic distance errors to be less severe. Given that the positions of the peaks roughly remain where they are in all examples we investigated, we can assume that the location of stellar streams in the ($V_{\rm az}$, $V_{\Delta E}$)-plane is not very sensitive to the expected systematic distance errors.

However, problems can arise when we want to distinguish adjacent streams that span more than one metallicity bin. Because the systematic errors can change with metallicity, the signal of a single stream can too and in this way produce apparently distinct, but adjacent, peaks.

Unresolved binary stars may affect our analysis through their effect on the photometric parallax relation and hence the distance determination. The number of multiple stellar systems expected in our sample of mainly G and K stars might be taken to be around 57% (probably lower) according to recent determinations (Lada 2006, and references therein).[16] Unresolved multiple stars taken as single stars have too high observed luminosities and hence their distances are underestimated. Another effect arises, if the multiple stellar systems consists of stars of different masses, which leads to a shift in colors. To get a feeling of how the distances change when we mistake a binary system as a single star, we calculate by how much the apparent magnitude, m, changes. In the case of equal-mass binaries, the observed flux, F, would be only half as high for a single star.

$$m = -2.5 \log \frac{F}{F_0} \tag{14}$$

[16] We note, however, that in our case of metal-poor stars the expected fraction of multiple stars drops further, because these stars tend to be older; hence, the systems had more time to disperse.

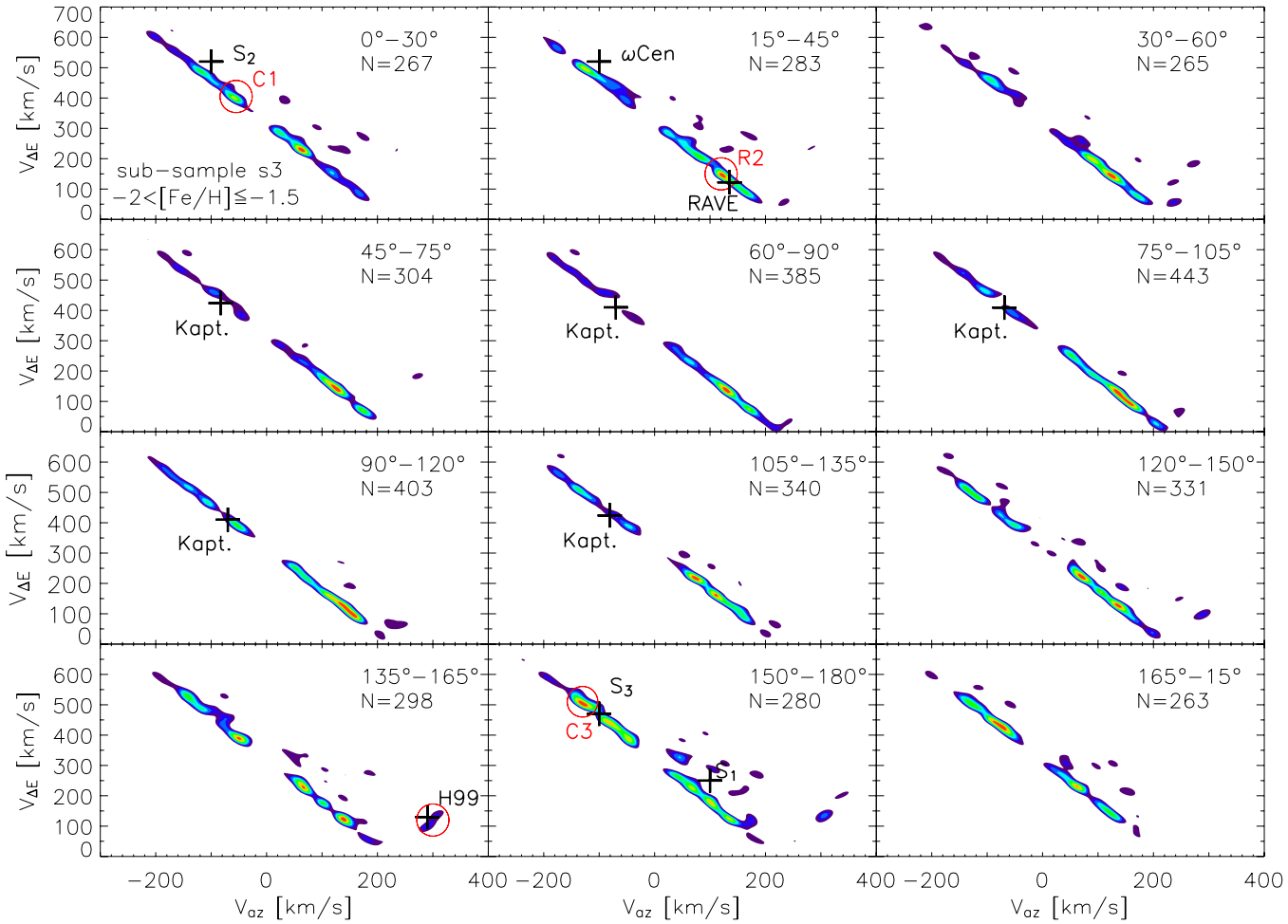

Figure 8. Same as Figure 6, but now for stars in the metallicity subsample s3.

is the definition of the apparent magnitude, where F_0 is some constant flux which gives $m = 0$. It follows that the apparent magnitude that would be assigned to only the single star from the binary system, m', is given by

$$m' = -2.5 \log \frac{0.5F}{F_0} \simeq m + 0.75. \quad (15)$$

Together with Equation (6), it follows that in the worst case (equal-mass binaries) the distances for part of our sample are underestimated by 29%. This is a systematic effect, and results in a change of the shape and relative "height" of the overdensities as discussed above. However, this effect might not be so severe, because (1) the change in distances has the opposite sign to the expected systematic error of the photometric parallax relation, (2) it affects approximately only half of our sample, and (3) most of nearby G-dwarf binary systems possess mass ratios that peak at much less than 1.0 (Duquennoy & Mayor 1991). In addition to the systematic underestimation of distances, the radial velocities for multiple systems are scattered around the value of the dominant component in a statistical way due to the additional Doppler shift in the spectrum of the bound system. Taken together, these effects are hard to describe quantitatively, but they certainly only dilute the signatures of real streams. Hence, this works to make the numbers we identify as stellar streams a lower limit of what might exist.

6. ESTIMATING THE SIGNIFICANCE OF OVERDENSITIES

It is clear that overdensities in $(V_{\rm az}, V_{\Delta E})$ can and will emerge through Poisson noise, especially in regions that are sparsely sampled by the data. As described in Paper I, Section 4.2, we can address this problem by performing Monte Carlo simulations with stars randomly drawn from a smooth distribution. From these we can build the residuals of the wavelet transforms of each individual simulation against the mean value for all wavelet transforms, which represents a smooth distribution over our search space. For each cell in $(V_{\rm az}, V_{\Delta E})$, we can calculate the variance and use it to obtain a significance map of the overdensities.[17]

For the smooth halo and thick-disk components, we adopt the results of Chiba & Beers (2000), who characterized the halo through a mean rotational velocity at $\langle\theta\rangle \approx 30$ km s^{-1}, with a radially elongated velocity ellipsoid $(\sigma_U, \sigma_V, \sigma_W) = (141 \pm 11, 106 \pm 9, 94 \pm 8)$ km s^{-1}. We further use $\langle\theta\rangle = 190$ km s^{-1} and $(\sigma_U, \sigma_V, \sigma_W) = (46 \pm 4, 50 \pm 4, 35 \pm 3)$ for the thick disk, and adopt their estimated fraction of thick-disk stars in our subsample s1 as 80%, in s2 as 30%, and in s3 as 10%. We are aware that the azimuthal drift for the thick-disk stars

[17] Artificially high significance levels can emerge if we divide the residuals by a standard deviation which is less than 1. For this reason, we set the variance to 1 in each cell where it is below this level.

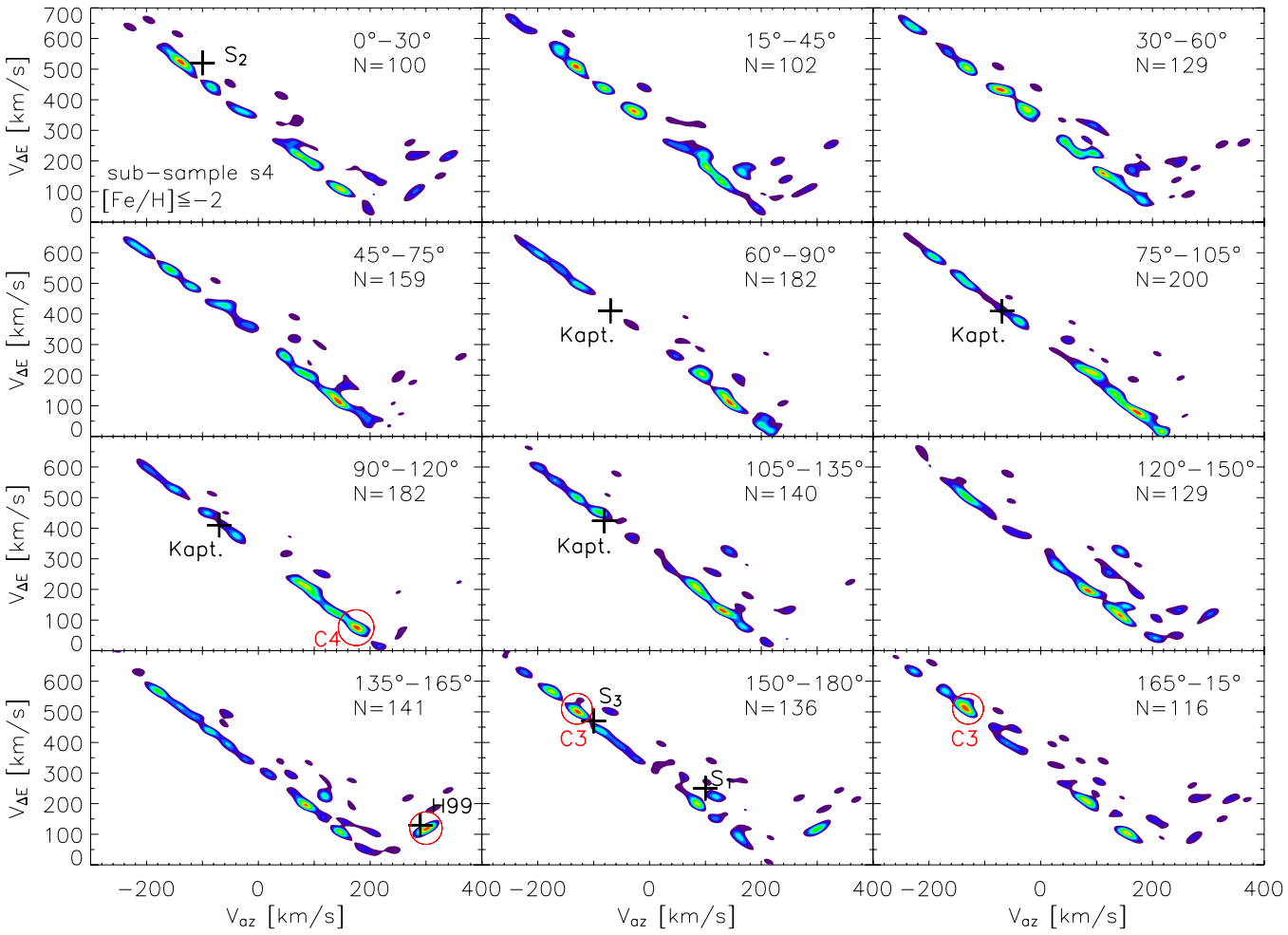

Figure 9. Same as Figure 6, but now for stars in the metallicity subsample s4.

Table 1
Velocities and Derived Effective Integrals of Motion for Known Solar Neighborhood Streams

Parameter	Kapteyn[a]	H99[b]	ω Cen[c]	RHLS[d]	S_1[e]	S_2[e]	S_3[e]	RAVE[f]
$\langle \lvert U \rvert \rangle$	63	84	···	294	···	···	···	24
$\sigma_{\lvert U \rvert}$	54	65	···	6	···	···	···	15
$\langle V \rangle + V_{\rm LSR}$	−69	130	···	99	···	···	···	61
σ_V	6	22	···	25	···	···	···	5
$\langle W \rangle$	−16	−240	···	239	···	···	···	121
σ_W	67	24	···	24	···	···	···	30
$\langle V_{\rm az} \rangle$	−71	273	−100	259	100	−100	−100	135
$\langle V_{\Delta E} \rangle$	416	128	520	302	250	520	470	122
$\langle \nu \rangle$	77	152	25	22	165	6	170	27
Expected in subsample	s1,s2,s3	s2,s3,s4	s2,s3	s3,s4	unknown	unknown	unknown	unknown

Notes. All velocities are given in km s^{-1} and the ν-angles in °. Note that "S_2" is probably the "ωCen" stream.
[a] Eggen (1996).
[b] Helmi et al. (1999); Kepley et al. (2007).
[c] Dinescu (2002); Brook et al. (2004).
[d] Re Fiorentin et al. (2005).
[e] Dettbarn et al. (2007).
[f] Paper I.

we adopt is at the lower end of values given in the literature; for example, Soubiran et al. (2003) found $\langle \theta \rangle = 159 \pm 5$ km s^{-1} from spectroscopic and kinematical analyses of nearly 400, mostly clump-giant, stars. However, their sample was limited to stars with abundances [Fe/H] > -0.65 and distances $d \lesssim$ 800 pc, so the Chiba & Beers (2000) data more closely resemble our own data. It should also be noted, for the purpose of this exercise, that we have not explicitly included the possible presence of stars from an outer-halo component. As Carollo et al. (2007) have argued, such stars only begin to dominate 15–20 kpc from the Galactic center and are not likely to comprise a major component in our solar neighborhood sample.

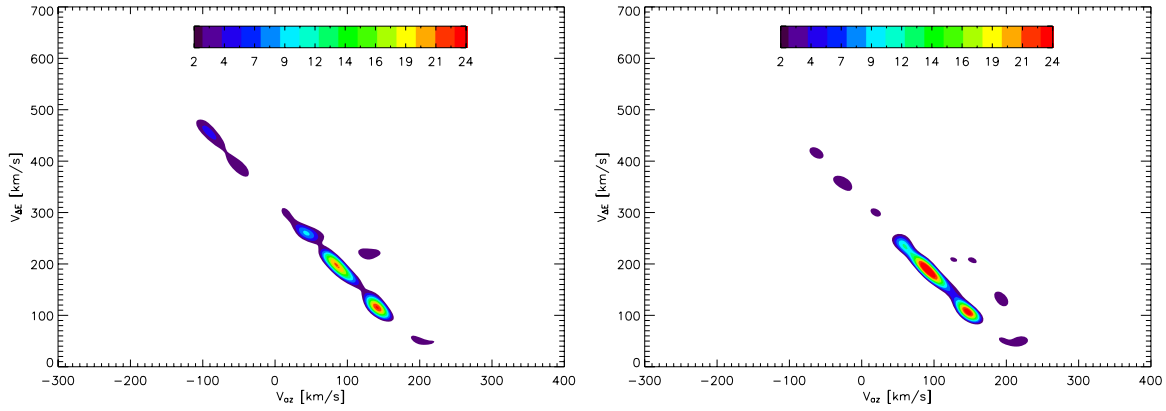

(a) without additional distance errors (b) with additional -10% distance errors

Figure 10. Contours of the wavelet transform for the distribution of stars from subsample s1 that lie in the ν range 15°–45° (b) The same distribution, but after adding a systematic distance error of −10% to the data. Note how the overdensities change shape and relative "height," but fairly keep their position. (a) Without additional distance errors and (b) with additional −10% distance errors.

To each velocity drawn from the smooth kinematic models (with Gaussian velocity ellipsoids) we assigned as an additional velocity error the mean velocity error of our data, that is, $\left(\langle\Delta U\rangle,\langle\Delta V\rangle,\ \langle\Delta W\rangle\right) = (14.9, 15.7, 12.2)$ km s^{-1}. For each metallicity subsample we built 30 Monte Carlo realizations with (by construction) smooth velocity distributions, consisting of the same number of stars as the subsample. The Monte Carlo samples were then analyzed in the same way as the real data, that is, by collecting the stars in different ν-bins and performing the wavelet analyses in these bins. Because the number of stars in each ν-bin is small, we expect a considerable amount of shot noise. Also, because the velocity dispersions are very large, small deviations from our choice of the velocity ellipsoid would probably result in large changes of the significance levels. In addition, a stellar stream populating a certain part of phase space with stars will increase the level of Poissonian fluctuations, which are proportional to $\sqrt{N}$. When we divide the residuals between our smooth model and these fluctuations by the expected sigma for the smooth model, it may lead to the appearance of apparently highly significant multiple, adjacent, peaks (while in fact they are a part of the same structure). We therefore treat the significances with care and keep in mind that one single stream can produce multiple close features. Figure 11 shows, as an example, the significance map for subsample s3, where we have only displayed areas with $\sigma \geqslant 2$. We inspected the significance maps for the other subsamples as well and derived significance levels for all putative stellar streams (for more details, see Klement 2009). Individual results are discussed in the following section.

7. THE RESULTS: STELLAR HALO STREAMS

Here we explore the best "slicing" in orbital parameter- and metallicity-space by using ($V_{\rm az}$, $V_{\Delta E}$, ν,[Fe/H]). Metallicity is an additional constraint to distinguish tidal and dynamical streams or different streams that occupy the same region in ($V_{\rm az}$, $V_{\Delta E}$, ν) space. Tidal debris still carries the chemical information of its progenitor, while dynamical streams are composed of stars that lack a common origin. In addition, the latter will contribute to our sample to a lesser extent as the metallicity decreases, because dynamical streams are dominated by disk stars. In the following, we will discuss all the "phase-space overdensities" that we identified either as previously known streams or likely candidates for new stellar halo streams.

Table 2
Main Characteristics of the Stellar Streams Considered Real

Stream	References	$V_{\rm az}$ (km s^{-1})	$V_{\Delta E}$ (km s^{-1})	ν (°)	σ	N	⟨[Fe/H]⟩	$\sigma_{\rm [Fe/H]}$
H99	Helmi et al. (1999)	300	120	150	12.0	21	−1.8	0.4
RAVE	Klement et al. (2008)	120	150	30	3.0	19	−1.4	0.3
S_3	Dettbarn et al. (2007)	−100	470	155	4.5	33	−1.6	0.4
C1	new	−60	410	15	2.9	32	−1.5	0.2
C2	new	−100	470	135	3.4	53	−1.6	0.4
C3	new	−130	510	170	3.7	44	−1.7	0.4
C4	new	175	75	100	4.8	20	−2.3	0.3

Notes. The parameter σ denotes the significance of the stream obtained as described in Section 6, N is the number of putative stream members, ⟨[Fe/H]⟩ is the mean metallicity of the stream, and $\sigma_{\rm [Fe/H]}$ is the standard deviation.

The preconditions for selecting these stream candidates included a sufficiently large number of stars ($N > 15$), a significance level $\sigma \geqslant 2$, and a metallicity distribution consistent with a tidal origin. Table 2 summarizes the main properties of the identified streams. Lists of the putative stream members, their stellar parameters, and their derived distances and kinematic parameters are provided in the appendix. We first consider any smooth components in the phase-space distribution and then concentrate on putative halo stars on non-disk-like orbits.

7.1. The Smooth Thick-Disk Component

We now discuss the phase-space distribution of the stars, starting with the highest metallicity bin, s1 (Figure 6). Stars in this metallicity range, between [Fe/H] = −0.5 and −1.0, should be dominated by members of the thick disk; this is clearly discernible as the smooth distribution of stars with polar angles around 90° that rotate with $\langle V_{\rm az}\rangle \approx 200$ km s^{-1} around the Galactic center. In the significance map, we have also found a hint of the "Hercules" stream at $(V_{\rm az}, V_{\Delta E}) \approx (169, 73)$ km s^{-1}.

For more highly inclined orbits, the distribution of stars peaks at lower azimuthal velocities (see Figure 6), indicating that the fraction of halo stars increases. In addition, at angles of $|\nu - 90°| \gtrsim 45°$, overdensities of stars on retrograde orbits begin to emerge. There is no longer a smooth stellar component on such orbits. At these orbital inclinations, a few stars are sufficient to create an artificially high signal, because the variances of the residuals between the single Monte Carlo realizations and their

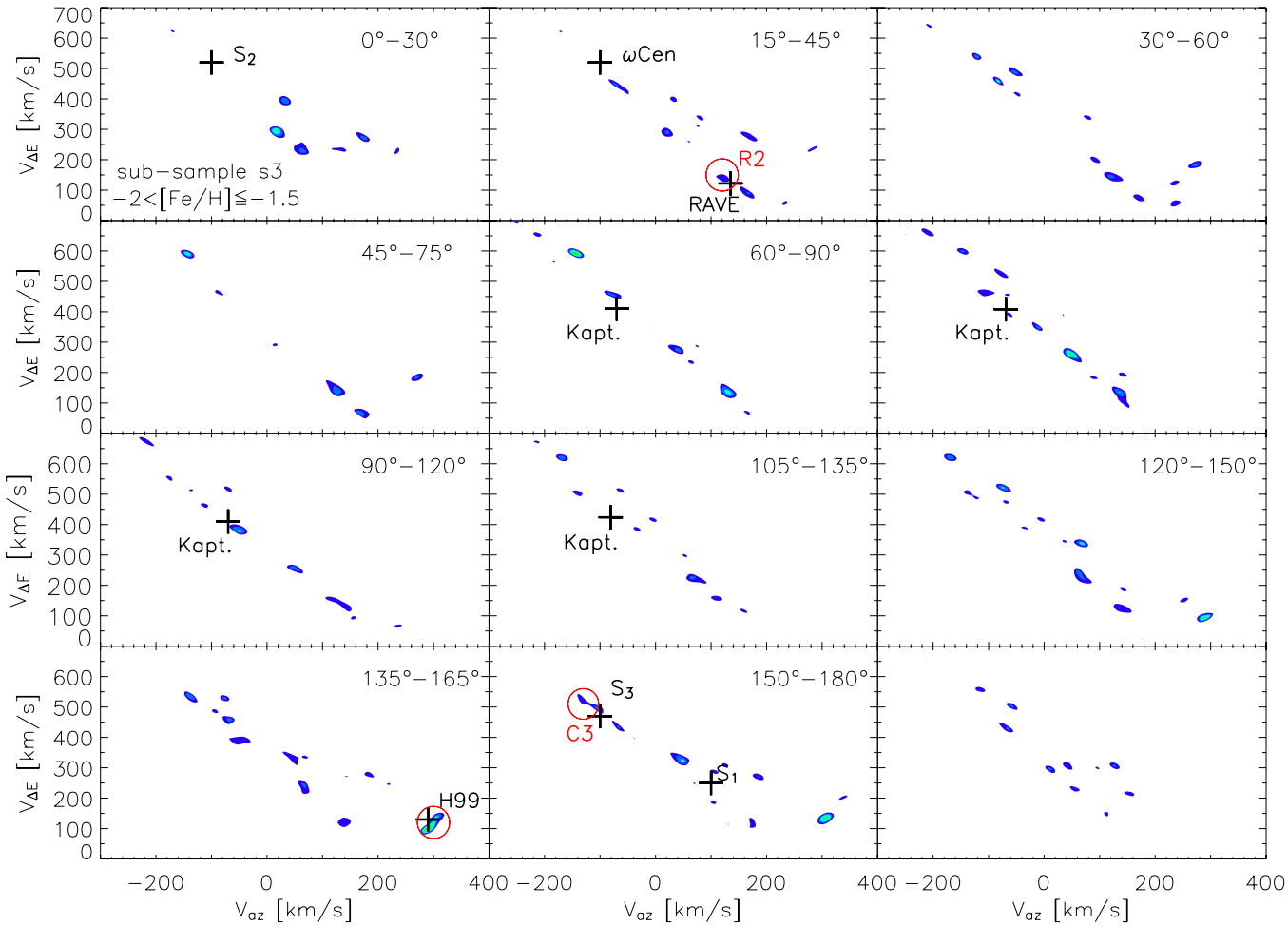

Figure 11. Significance map of the overdensities from Figure 8. Only areas with $\sigma \geqslant 2$ are shown. The contours range from 2 (blue) to 10 (red). Note the abundance of stars on disklike orbits. The crosses mark the expected position of already known stellar streams. Kapteyn's stream appears more than once, because it is well defined in (U, V), but not W, so it spans a broader range of orbital inclinations (because $\nu = \arctan \frac{V}{W}$).

smooth superposition are nominally very small. Therefore, we question whether such overdensities in s1 are real, unless they also show up in the other metallicity subsamples.

The amount of substructure increases for the subsample s2, which consists of stars in the metallicity range $-1.5 <$ [Fe/H] $\leqslant -1.0$ (Figure 7). There are still a large numbers of stars on disklike orbits, with 46% of the stars having orbital inclinations between 75° and 105°. The mean rotational lag with respect to the LSR increases further. According to Chiba & Beers (2000), $\langle\theta\rangle$ decreases linearly with [Fe/H] for [Fe/H] $\gtrsim -1.7$ and stays approximately constant below [Fe/H] $= -1.7$.

It is hard to make out substructure among the stars on disklike orbits, but we think we see a hint of the stream "AF06" detected by Arifyanto & Fuchs (2006) and Helmi et al. (2006). Its stars have orbital inclinations ranging from slightly below to slightly above the Galactic plane, depending on whether we take stars with positive or negative W velocities from the list of member stars given in Arifyanto & Fuchs (2006). We detect a signal of this stream at ($V_{\rm az}$, $V_{\Delta E}$) $\approx$ (140, 110) km s^{-1} in the ν-slice 90°–120°, maybe even extending toward 105°–135°.

In the subsample s3, at metallicities in the range $-2.0 <$ [Fe/H] $\leqslant -1.5$ (Figure 8), the fraction of halo stars dominates over thick-disk stars. In the regions of the dynamical streams "Hercules" and "AF06," we detect signals that are significant above $\sigma \geqslant 2$. These signals remain even for the subsample s4 (with [Fe/H] < -2.0), where the fraction of canonical thick-disk stars should be negligible, showing that still some (metal-weak) thick-disk stars are present.

7.2. *Confirming the Discovery of the RAVE DR-1 Stream*

We now consider the location of the stream discovered in the RAVE DR-1 data discussed in Paper I. This stream is centered at a mean of ($V_{\rm az}$, $V_{\Delta E}$) $\approx$ (135, 122) km s^{-1} and $\nu \approx 30°$.[18] The stars of this stream possess high vertical and low radial velocity components, $\langle W\rangle = 121 \pm 2$ km s^{-1} and $\langle U\rangle = 24 \pm 2$ km s^{-1} (Paper I, Section 6). Their V-velocities range from -180 km s$^{-1} \lesssim V \lesssim -140$ km s^{-1}, so their orbital plane is inclined at an angle of $\nu \approx 30°$. Indeed, in the ν-range 15°–45° there exist overdensities very close to the predicted position of the "RAVE" stream: one in subsample s1, at $V_{\rm az} \approx 140$ km s^{-1}, which we labeled as "R1" (Figure 6), and one in subsamples s2 and s3, at lower azimuthal velocities of $V_{\rm az} \approx 120$ km s^{-1}, which we labeled as "R2" (Figures 7 and 8). The fact that "R2" is located at the same position in s2 and s3 makes it unlikely that it

[18] In the analysis of the RAVE stars, Klement et al. (2009) projected their azimuthal motions onto the Galactic plane by adopting a cylindrical coordinate system and setting $V_{\rm az} = V$, $V_{\Delta E} = \sqrt{U^2 + 2(V_{\rm az} - V_{\rm LSR})^2}$. This worked because the RAVE sample did not contain many halo stars. The elongation of the stream in the RAVE sample, however, could be a hint that actually more than one stream on different orbital planes has been projected onto the Galactic midplane.

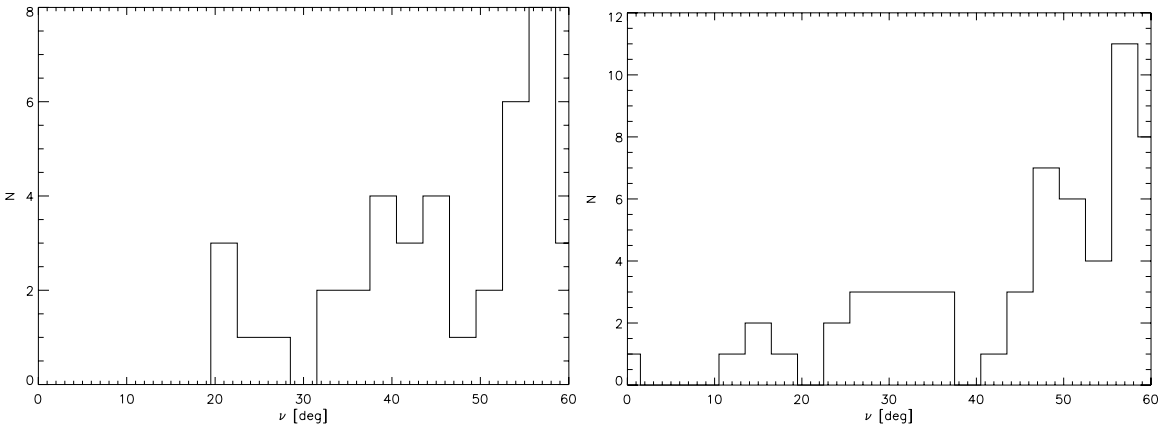

(a) 'R1' (b) 'R2'

Figure 12. Distribution of orbital inclinations ν of stars that lie at the same ($V_{\rm az}$, $V_{\Delta E}$)-position as the red contoured peaks of the overdensities "R1" in Figure 6(a) and "R2" in Figure 7(b). The distribution for "R1" is not clearly peaked around a distinct orbital polar angle, while "R2" is centered at $\nu \approx 30^\circ$. The ν range of 0°–60° is part of the preliminary condition for putative member stars of "R1" and "R2."

arises from Poisson noise. The possibility exists that "R1" and "R2," which possess slightly different angular momenta, are causally connected, perhaps resembling two distinct streams from a disrupted satellite.

To test this hypothesis, we proceed as follows. We first examine the distribution of ν-angles for all stars that lie at the positions of "R1" and "R2" in ($V_{\rm az}$, $V_{\Delta E}$) space, in order to check which orbital inclinations can be assigned to the overdensities, and if they differ for "R1" and "R2." Then we can pick stream member stars according to their positions in $V_{\rm az}$, $V_{\Delta E}$, and ν, and look at their metallicity distributions.

We select the ($V_{\rm az}$, $V_{\Delta E}$) position of the two streams in the following manner. For the stream at $V_{\rm az} \approx 140$ km s^{-1}, "R1," we require $|(V_{\rm az}, V_{\Delta E}) - (140, 120)| \leqslant (30, 30)$ km s^{-1}, $|\nu - 30^\circ| \leqslant 30^\circ$, and a value of the wavelet transform in s1 of at least 90% of its maximum value in that ν range (which corresponds to the red-colored contours in Figures 6–9). We also add stars from subsamples s2 and s3 that lie in this region of ($V_{\rm az}$, $V_{\Delta E}$) space as possible stream members at lower metallicities, although their signature is not visible in the significance maps. For the stream "R2," at $V_{\rm az} \approx 120$ km s^{-1}, we require $|(V_{\rm az}, V_{\Delta E}) - (120, 150)| \leqslant (30, 30)$ km s^{-1}, $|\nu - 30^\circ| \leqslant 30^\circ$, and a value of the wavelet transform in s2 of at least 90% of its maximum value in that ν range. We also add stars from s1 that lie at this position as possible stream members of higher metallicity. The distribution of ν-angles is shown in Figure 12

From inspection of Figure 12, we cannot clearly assign an orbital polar angle to the stream "R1"; stars distributed around both $\nu \approx 25^\circ$ and $\nu \approx 40^\circ$ contribute to the signal in the wavelet transform in Figure 6. In contrast, at the position of "R2" there is a group of stars that clump around $\nu = 30^\circ$, which is the polar angle of the "RAVE" stream. Assuming that "R1" and "R2" stem from the same progenitor, it is possible that the difference in the ν-distributions is caused by accelerations and decelerations of the stream stars by their precursor object's potential (Choi et al. 2007). However, in this case they still should exhibit the same metallicity distributions. The fact that "R1" is mostly present in the subsample s1, while "R2" shows up in s2 and s3, suggests that the [Fe/H] distributions are different. Figure 13 compares the [Fe/H] distributions, where we now confine the putative stream members into the ν range $|\nu - 30^\circ| \leqslant 15^\circ$. In the large panels, the stars are further selected to lie at the position where the wavelet transform takes on at least 90% of its maximum value in this ν range, while we lessen this requirement to 75% in the small panels to obtain more stars.

The two [Fe/H] distributions are not compatible with the hypothesis that both streams originate from the same precursor object. The [Fe/H] distribution of "R2" peaks at metallicities between -1.2 and -1.8, and the stream does not seem to contain stars more metal poor than [Fe/H] $= -0.5$. On the other hand, "R1" has one peak at [Fe/H] ≈ -1.6, and a broad plateau possibly continuing beyond [Fe/H] $= -0.5$. We have checked for a correlation between the double-peaked ν distribution and the [Fe/H] distribution of "R1," but it does not exist. We conclude from the ν- and [Fe/H] distributions that a tidal origin of "R1" is ruled out. "R1" and "R2" are not correlated, in the sense that they originate from a single progenitor, and the high significance of "R1" ($\sigma \approx 8$) could be a result of the small variance of our smooth reference model in this region of ($V_{\rm az}$, $V_{\Delta E}$, ν) space.

We retain "R2" as a likely tidal stream candidate and show its (U, V, W) distribution in Figure 14. Here, light blue dots represent stars in the metallicity range $-1.0 <$ Fe/H $\leqslant -0.5$, blue dots for stars with $-1.5 <$ Fe/H $\leqslant -1.0$, while green dots correspond to stars in the range $-2.0 <$ Fe/H $\leqslant -1.5$. The small black dots are stars in the range $-2.0 <$ Fe/H $\leqslant -0.5$ and $|\nu - 30^\circ| \leqslant 15^\circ$, and are displayed as the background population. The stars approximately show a "banana" shaped distribution in (U, V), which is typical for tidal streams near their apocenters (Helmi et al. 2006). The banana shape results from the condition $V_{\Delta E} =$ constant, which describes an ellipse in (U, $V_{\rm az}$), that is, in the radial and azimuthal velocities in the orbital plane of the stream. If the distribution in W is sufficiently narrow, this shape also appears in the (U, V) distribution.

The U,V, and W velocities are consistent with those found in the RAVE sample: $(\langle U\rangle, \langle V\rangle, \langle W\rangle) = (-5 \pm 13, 59 \pm 5, 98 \pm 3)$ km s^{-1}. We have good reason to believe that we have rediscovered their proposed new stream. The metallicity distribution, shown in Figure 13(b), suggests that the stream consists of stars mainly in the range $-1.8 \lesssim$ [Fe/H] $\lesssim -1.2$.

7.3. A New Stream Candidate

Centered at even lower orbital polar angles than the "RAVE" stream in subsample s2 ($-1.5 <$ [Fe/H] < -1.0) (Figure 7),

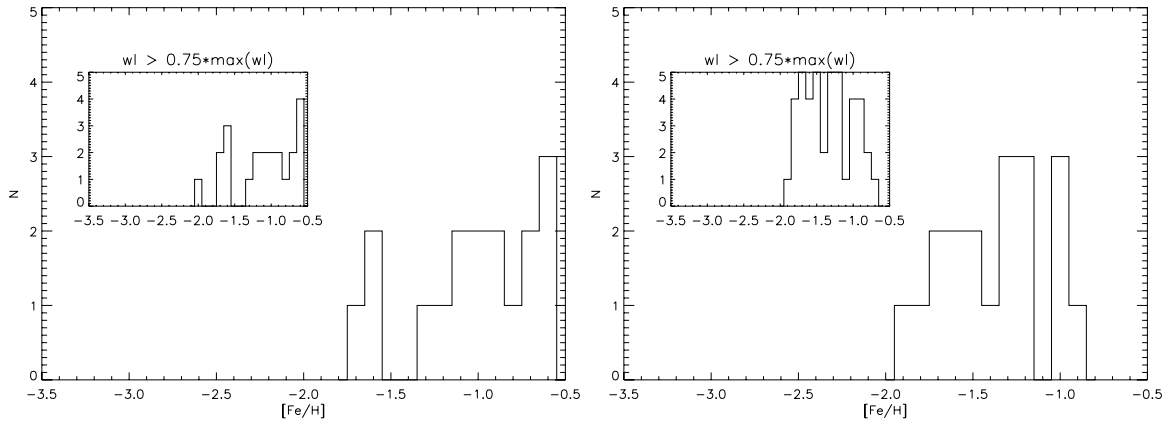

(a) 'R1' (b) 'R2'

Figure 13. Large panels: [Fe/H] distribution of stars that lie at the same (V_{az}, $V_{\Delta E}$)-position as the red contoured peaks (wl = 0.9·wl$_{max}$) of the overdensities "R1" in Figure 6(a) and "R2" in Figure 7(b). "R1" seems to peak at lower metallicity than "R2." Small panels: same as the large panels, but now stars have been selected from a larger region confined through wl= 0.75·wl$_{max}$. The difference between both [Fe/H] distributions is more pronounced.

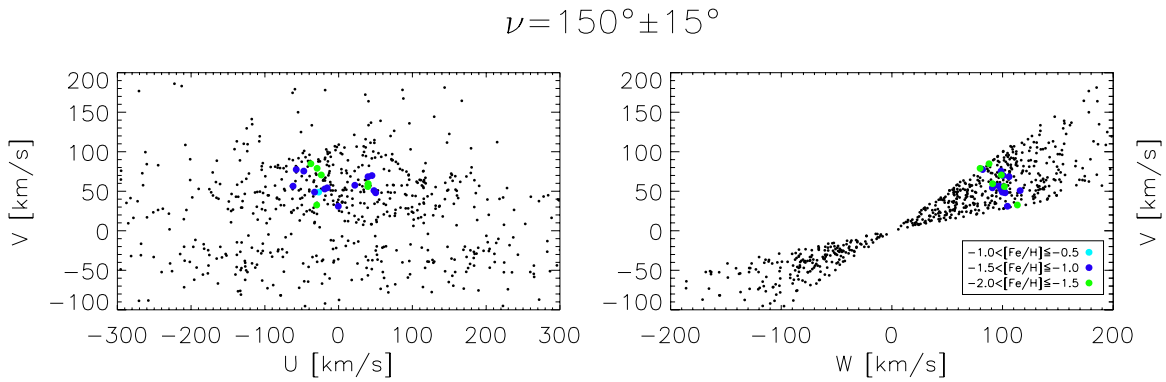

Figure 14. Distribution of putative members of the stream discovered in RAVE data (Paper I) in (U, V, W). Note the banana-shaped (U, V) distribution centered at $U = 0$, indicating that the stream stars are near their orbital apocenters.

(A color version of this figure is available in the online journal.)

we find an overdensity of stars around (V_{az}, $V_{\Delta E}$) ≈ (−60, 410). This overdensity extends toward the subsample s3, so it is unlikely to be caused by Poisson noise. Because we do not know of any stream in the literature with such kinematics, we have labeled this overdensity "C1" for our first new stream candidate. The significance of this feature is $\sigma \approx 2.9$. We analyze its [Fe/H], angular momentum, and velocity distribution in Figure 15.

Because the velocity distribution is symmetric around $U = 0$, these stars must be moving toward and away from their apocenters. The typical banana shape is indicated in the (U, V) distribution, but not perfectly so. Because of the high polar angle of the orbit, the banana shape in (U, V_{az}) (which is predicted by the condition $V_{\Delta E}$ =constant) does not perfectly translate into (U, V). The metallicity distribution is roughly symmetric around [Fe/H] = −1.5 and hints toward the distribution of tidal debris from a single metal-poor progenitor. We propose C1 to be a newly discovered halo stream passing through the solar vicinity.

7.4. Two Related Streams?

The retrograde stream labeled "S_3" was discovered by Dettbarn et al. (2007) as an overdensity centered at (V_{az}, $V_{\Delta E}$, ν) = (−100 km s^{-1}, 470 km s^{-1}, 170°). We also find an overdensity of stars at this position in subsample s2 (−1.5 < [Fe/H] < −1.0), but peaked at $\nu \approx 155°$. Nevertheless, we identify this overdensity with "S_3," because from Figure 3 in Dettbarn et al. (2007) we can see that the wavelet contours of their feature seem to extend toward $\nu \approx 155°$.

In the ν-slice 120°–150°, we detect another overdensity at nearly the same (V_{az}, $V_{\Delta E}$) values as "S_3," to which we assign the name "C2." This corresponds to a second peak in the ν distribution of stars in the (V_{az}, $V_{\Delta E}$) range centered at ≈ (−105, 480) km s^{-1}. We suspect that both "C2" and "S_3" contribute to the high signal of the wavelet transform in the ν-slice 135°–165° in Figure 7. This is confirmed in Figure 16, where we have plotted the ν distribution of all stars that are located at the same (V_{az}, $V_{\Delta E}$) position as the overdense region in this ν-slice. The two peaks at $\nu \approx 155°$ and $\nu \approx 135°$ correspond to the streams "S_3" and "C2," respectively.

Figure 16 seems to suggest that "S_3" and "C2" are two distinct streams that move with nearly the same orbital inclinations and eccentricities, but on different orbital planes that differ by only ∼20°. Such a double-peaked ν distribution could hint toward two tidal streams lost at different times from a progenitor whose orbital plane has precessed slightly during many orbits in the Milky Way. However, on a more careful look at Figure 16 we see that only a handful of stars are in each distinct peak. The apparent bimodality already becomes much less prominent when we increase the binsize of the histogram from 5° to 7°. If we consider all sources of errors and noise ([Fe/H]-determination, possible systematic distance errors, proper motion errors, unresolved

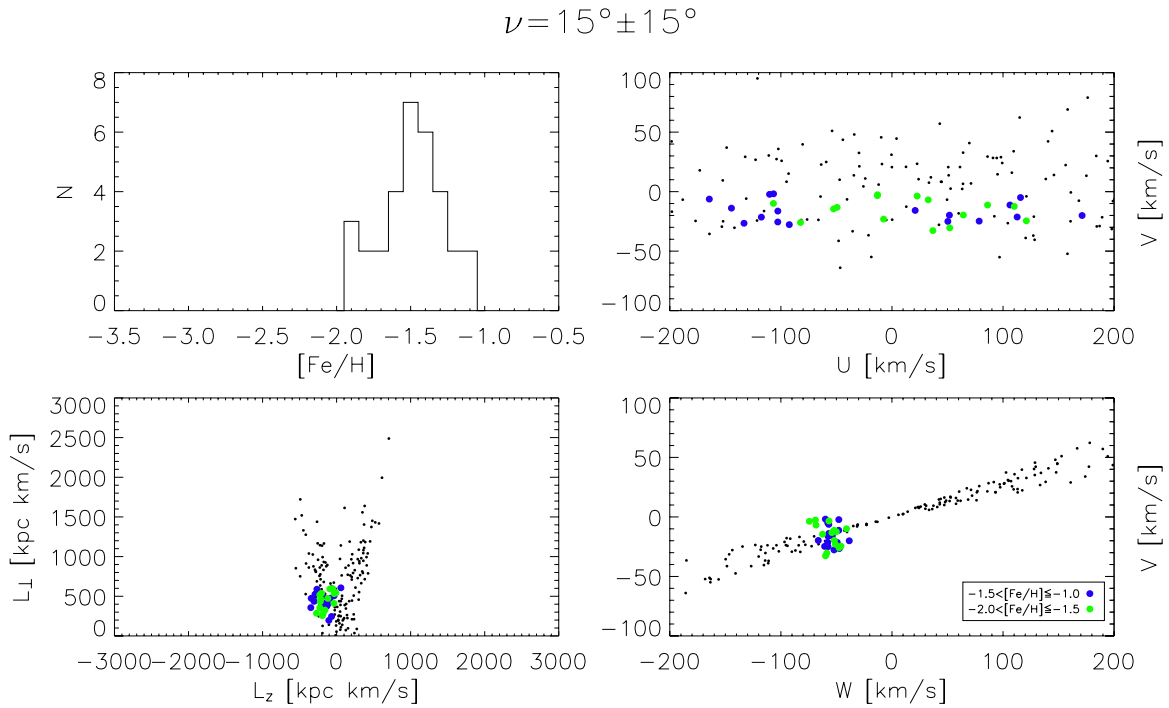

Figure 15. Distribution of members of the stream candidate "C1" in metallicity [Fe/H], angular momentum (L_z, $L_\perp$) and (U, V, W). Blue dots show stars in the range $-1.5 < \mathrm{Fe/H} \leqslant -1.0$, while green dots stars represent stars with $-2.0 < \mathrm{Fe/H} \leqslant -1.5$. The small black dots are all stars in our sample with $-2.0 < \mathrm{Fe/H} \leqslant -1.0$ and $|\nu - 15^\circ| \leqslant 15^\circ$. The ($U$, V) distribution is symmetric around $U = 0$, indicating that the stream stars are well mixed and near their orbital apocenters.

(A color version of this figure is available in the online journal.)

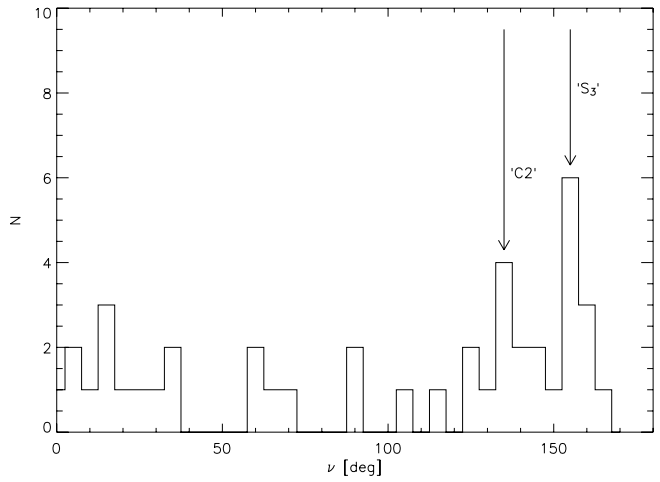

Figure 16. Distribution of orbital inclinations ν for all stars in subsample s2 that occupy the same region in (V_{az}, $V_{\Delta E}$) space as the overdensity labeled "S_3" in Figure 7, ν-slice 135°–165°. The location of the overdensity is selected from the appropriate ranges in V_{az} and $V_{\Delta E}$ and the condition that the wavelet transform has at least 50% of its maximum value (to select the green-framed "bump.")

binaries, Poisson noise), could it be that we are looking at a single stream that has just been smeared out in the ν space by the errors?

We test this hypothesis by analyzing the kinematical and chemical properties of both features.

Figures 17 and 18 show the [Fe/H], (L_z, $L_\perp$), and (U, V, W) distributions for "C2" and "S_3," respectively. Although it seems that "C2" does not contain stars in the range $-2.0 < \mathrm{[Fe/H]} \leqslant -1.5$ from the "gap" in the wavelet transform contours in Figure 8, we include stars from subsamples s3 and s4 that lie in the same region as the putative stream members from s2. This is justified from the [Fe/H] distribution shown in Figure 17, which peaks at [Fe/H] ≈ -1.5 and falls off along a tail toward lower metallicities. It resembles the distribution of a coeval tidally disrupted stellar population. We do the same for "S3," and include all stars in the range [Fe/H] $\leqslant -0.5$ and $|\nu - 155^\circ| < 15^\circ$. This stream also peaks around [Fe/H] ≈ -1.5 (Figure 18). We note that through these selection criteria, nine stars appear in both "C2" and "S_3."

The banana-shaped (U, V) distribution for the stream "C2" indicates that its stars are near their orbital apocenters. The velocity distribution of "S_3" is only slightly different. The stars appear to be not as close to their apocenters as the "C2" stars. Both the (U, V, W) and [Fe/H] as well as the similar L_z distributions seem to support the hypothesis that "C2" and "S_3" are in fact one single stellar stream. Taking into account the typical statistical velocity errors discussed in Section 2.1.1, we find that stars at such velocities as those of "C2" could well be misplaced by ±5° in ν and ±5 km s^{-1} in V_{az} and $V_{\Delta E}$, which would lead to a smearing out of one single stream in ν space (Figure 5.8(b); see also Klement 2009).

We conclude that there exists evidence from the (U, V, W) and [Fe/H] distributions that "C2" and "S_3" belong to one single stream which might has been smeared out in ν space and—to a lesser degree—in (V_{az}, $V_{\Delta E}$) space. In addition, the L_z distributions are similar enough to support this hypothesis.

7.5. The Helmi Stream

We again examine the metallicity range of subsample s2, $-1.5 < \mathrm{Fe/H} \leqslant -1.0$, and find an overdensity of stars on a highly prograde orbit inclined at $\nu \approx 150^\circ$. This is the stream discovered by Helmi et al. (1999), located at (V_{az}, $V_{\Delta E}$, ν) = (300, 120, 150°), in very good agreement with the signal of this stream in the data set of Dettbarn et al. (2007) (see Table 1). The stream, labeled "H99," was originally discovered

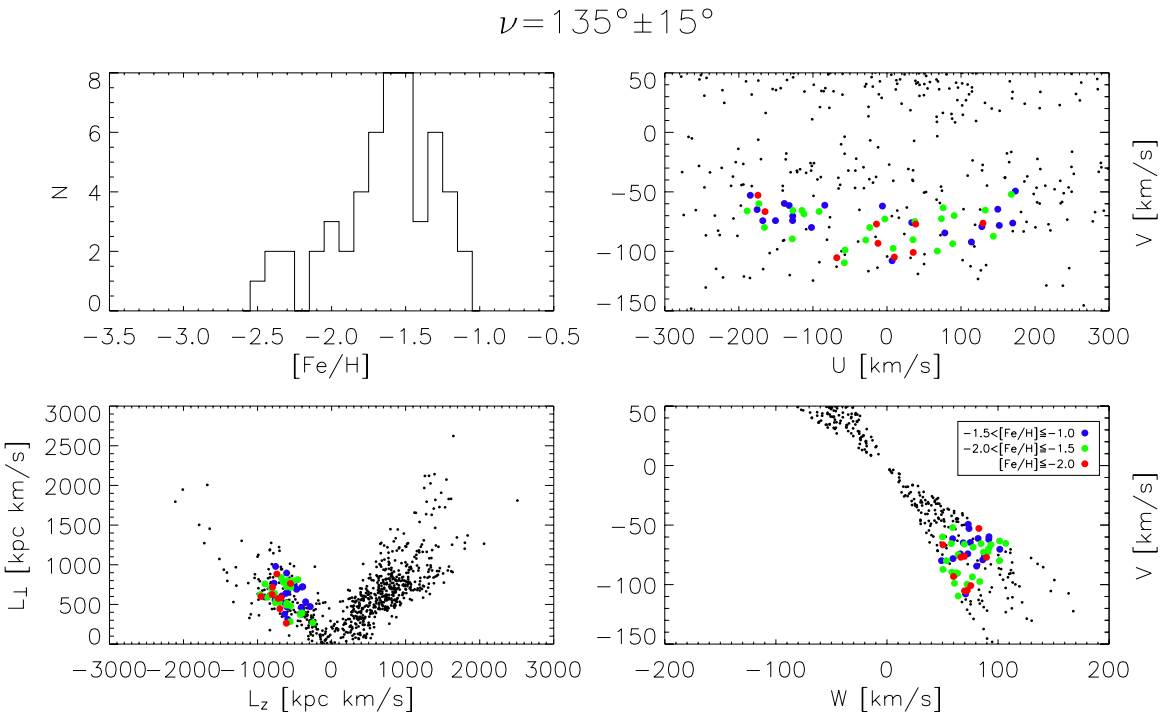

Figure 17. [Fe/H], (L_z, $L_\perp$), and (U, V, W) distributions for stars belonging to the stream candidate "C2." Light blue dots show stars in the metallicity range $-1.0 < \mathrm{Fe/H} \leqslant -0.5$, dark blue dots in the range $-1.5 < \mathrm{Fe/H} \leqslant -1.0$, and green dots show stars with $-2.0 < \mathrm{Fe/H} \leqslant -1.5$. The small black dots are all stars in our sample that occupy the same [Fe/H] and ν ranges as the member stars of "C2."

(A color version of this figure is available in the online journal.)

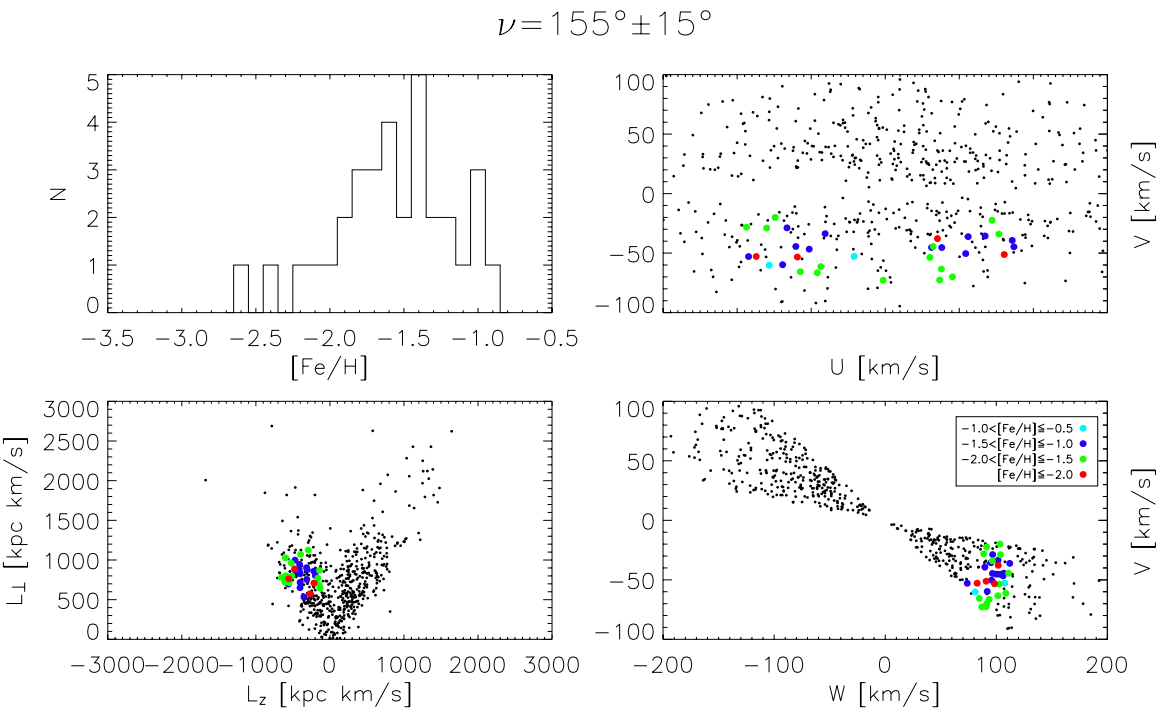

Figure 18. [Fe/H], (L_z, $L_\perp$), and (U, V, W) distributions for stars belonging to the stream "S_3." The colors have the same meaning as in Figure 17.

(A color version of this figure is available in the online journal.)

as an overdensity of stars in the angular momentum space. Later, Chiba & Beers (2000) confirmed the existence of this stream in their own data set and identified a possible extension toward higher azimuthal rotation. Although their data set was approximately thrice the size of the sample used by Helmi et al. (1999), the number of stream stars ($N = 10$) stayed constant. They hypothesized that the "H99" stream could be related to the "trail" extension, if this "trail" gained angular momentum from the interaction of the progenitor with the Milky Way's gravitational potential.

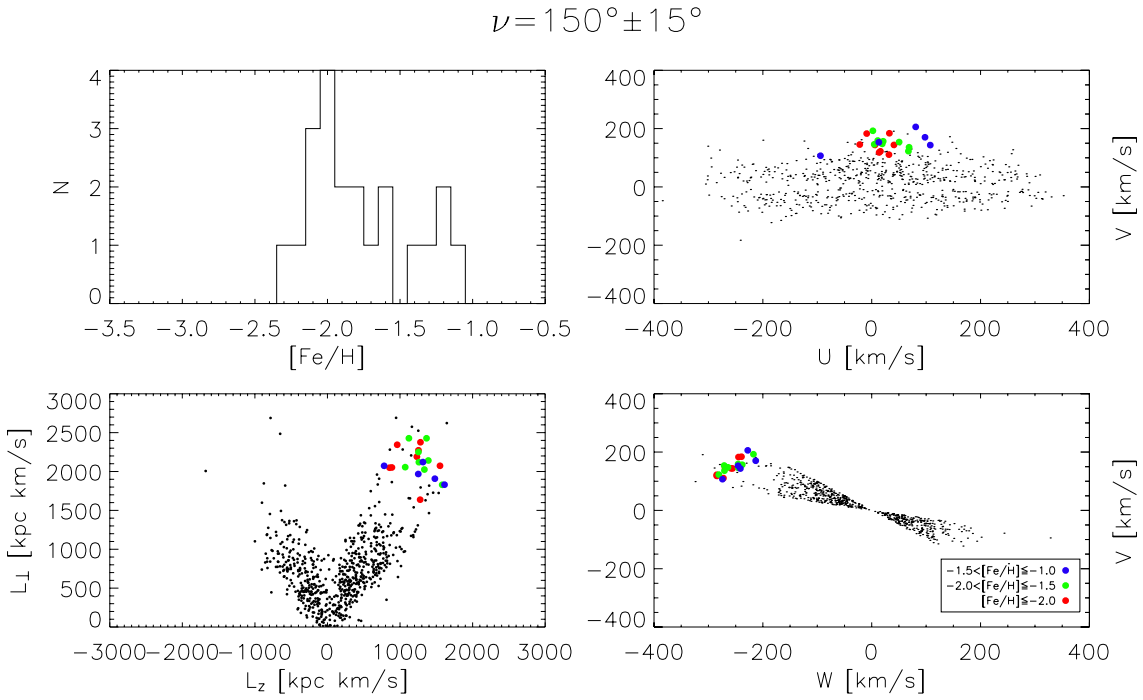

Figure 19. Distributions of members of the "H99" stream in [Fe/H], $(L_z, L_\perp)$, and (U, V, W). Blue dots show stars in the metallicity range $-1.5 < \mathrm{Fe/H} \leqslant -1.0$, green dots stars with $-2.0 < \mathrm{Fe/H} \leqslant -1.5$, and red dots stars with $\mathrm{Fe/H} \leqslant -2.0$. The small black dots are all stars in our sample with $\mathrm{Fe/H} \leqslant -1.0$ and $|\nu - 150°| \leqslant 15°$. The (U, V, W) distribution is in very good agreement to that shown by Helmi et al. (1999, their Figure 2).

(A color version of this figure is available in the online journal.)

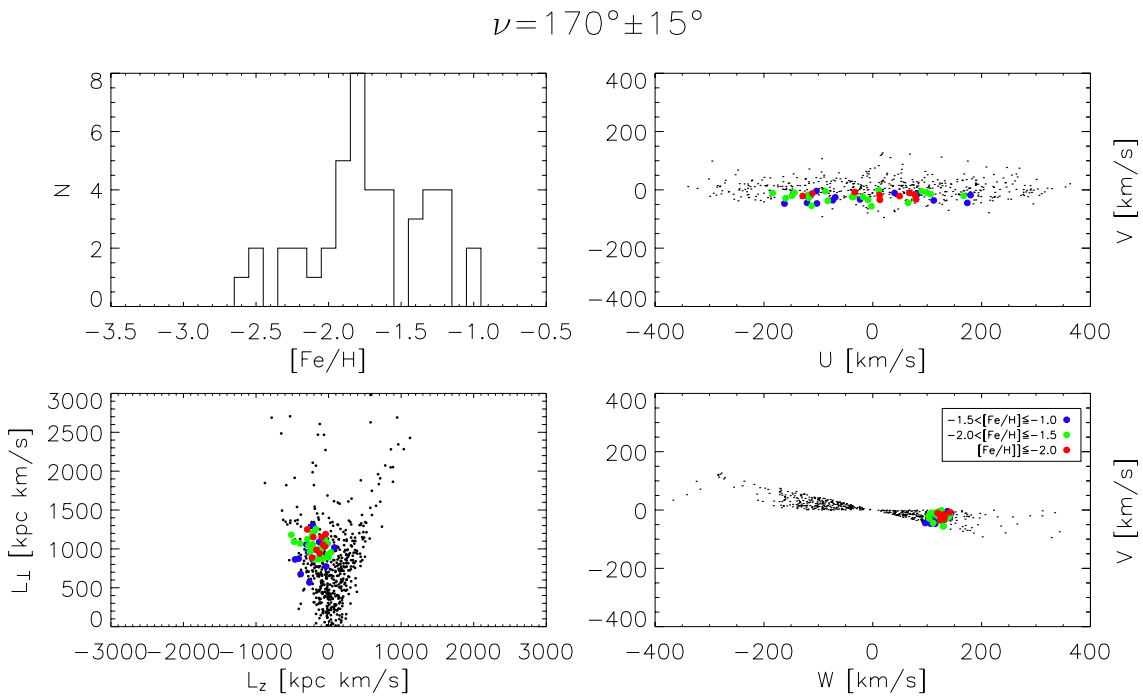

Figure 20. Distribution of members of the "C3" stream candidate in [Fe/H], $(L_z, L_\perp)$, and (U, V, W). Blue dots show stars in the metallicity range $-1.5 < \mathrm{Fe/H} \leqslant -1.0$, green dots stars with $-2.0 < \mathrm{Fe/H} \leqslant -1.5$, and red dots stars with $\mathrm{Fe/H} \leqslant -2.0$. The small black dots are all stars in our sample with $\mathrm{Fe/H} \leqslant -1.0$ and $|\nu - 170°| \leqslant 15°$.

(A color version of this figure is available in the online journal.)

Figure 19 shows the [Fe/H], $(L_z, L_\perp)$, and (U, V, W) distributions of all stars that we assign to the "H99" stream. The stream extends toward lower metallicities and is highly significant in the subsample s4. The (U, V, W) and $(L_z, L_\perp)$ distributions agree very well with those in the original work of Helmi et al. (1999, their Figure 2). The [Fe/H] distribution peaks at $[\mathrm{Fe/H}] \approx -2.0$ and does not extend beyond $[\mathrm{Fe/H}] \approx -2.3$. The range of [Fe/H] values that we find for the "H99" stream agrees well with the [Fe/H] values of the "H99" stream members given by Kepley et al. (2007), although they report two stream members with $[\mathrm{Fe/H}] < -2.3$. The number of stars in our sample that we identify as "H99" members is $N = 21$, approximately double that of previous studies. However, the number is too small to account for as much as one-tenth of the

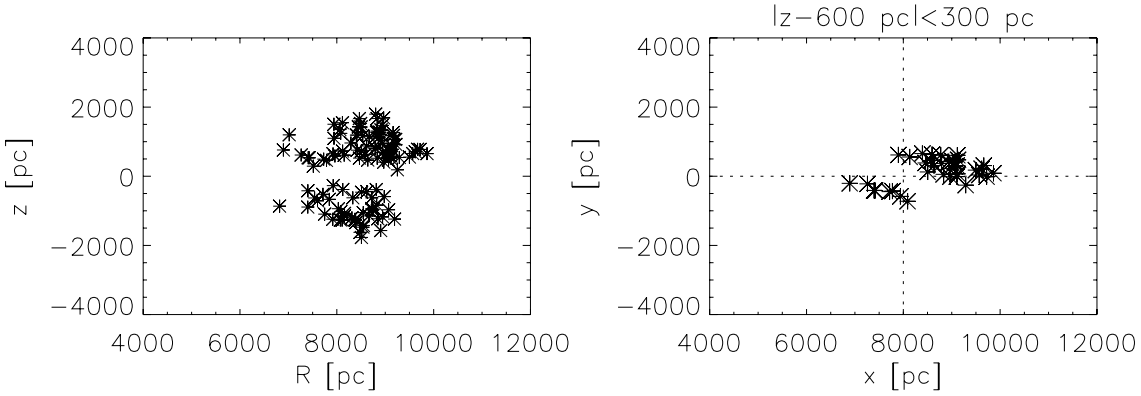

Figure 21. Spatial distribution of stars which we identify as members of the composite stream "S_3/C2/C3." In the left panel we show all 97 stars in the $(R - z)$ plane, while in the right panel we concentrate on a slice at $z = 600$ pc, analog to Figure 27 in Juric et al. (2008). Note the very similar location of the main overdensity in the $z = 600$ pc slice.

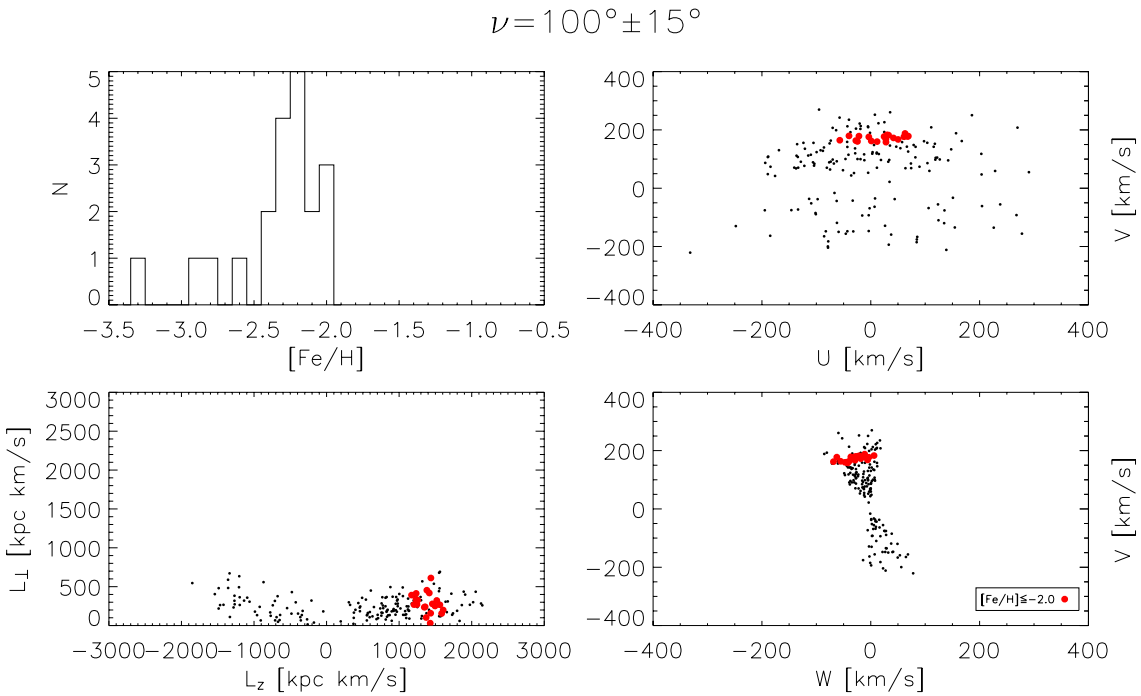

Figure 22. Distribution of members of the "C4" stream candidate in metallicity [Fe/H], $(L_z, L_\perp)$, and (U, V, W). The small black dots are all stars in our sample with Fe/H $\leqslant -2.0$ and $|\nu - 100^\circ| \leqslant 10^\circ$.

(A color version of this figure is available in the online journal.)

halo stars that are currently present in the solar neighborhood, as suggested by Helmi et al. (1999).

7.6. More Substructure at Very Low Metallicities

In the subsamples s3 ($-2.0 <$ [Fe/H] < -1.5) and s4 ([Fe/H] < -2.0), the amount of substructure increases further. We expect a contribution of only ∼10% thick-disk stars in s3 and 100% halo stars in s4 (Chiba & Beers 2000). While about 46% of the stars in subsample s2 move on disklike orbits ($75^\circ \leqslant \nu < 105^\circ$), this number drops to 23% for both s3 and s4. It seems that also for stars more metal poor than [Fe/H] $= -2$, a small fraction of stars with (metal-weak) thick-disk-like kinematics remains constant.

Besides the already discussed streams that are also visible in s3, "RAVE," "H99," and "C1," we find an overdensity centered at $(V_{\rm az}, V_{\Delta E}, \nu) = (-130\ {\rm km\ s^{-1}}, 510\ {\rm km\ s^{-1}}, 170^\circ)$, which we label as "C3." It is located near the stream "S_3" and—like "C2'—may be related to it. The peak in the ν distribution of stars in this region of $(V_{\rm az}, V_{\Delta E})$ space at $\nu = 170$ would fit exactly to the ν value originally assigned to "S_3" by Dettbarn et al. (2007). The [Fe/H] distribution peaks at [Fe/H] ≈ -1.8, and is consistent with that of "S_3" or "C2" (Figure 20). The velocity and L_z distribution of "C3" seem to differ slightly from those of the "S_3/C2" stream. However, like in the case of "C2" and "S_3," if we consider all possible error sources the possibility exists that one single stream manifests itself in several adjacent features. In particular, we refer to Section 5, where we have shown that a systematic distance error of 10% alone is able to cause such an effect by changing the relative "heights" of overdensities. In addition, as already noted in Section 6, the confidence levels for substructures the way we compute them depend on the priors we choose for the Monte Carlo simulations (smooth halo). But given the case that the "S_3/C2" stream is there, its existence increases the number of stars in that region of phase space, which increases the level of Poissonian fluctuations (as they are proportional to $\sqrt{N}$). When we divide the residuals between a smooth background and these fluctuations by the expected

sigma for the smooth background, it may lead to the appearance of apparently highly significant multiple, adjacent, peaks (while in fact they are a part of the same structure).

We gain confidence that "C3" is a not a feature created from Poisson noise from the fact that the wavelet transform at "C3's" position in the $(V_{\rm az}, V_{\Delta E})$ space has values greater than 90% of its maximum in both subsamples s3 and s4 (Figures 8 and 9). Furthermore, "C3" appears in the significance map of subsample s3 (Figure 11) at a significance level greater than 2.

Given its proximity to the "S_3/C2" stream and the uncertainties in our variables (in particular [Fe/H], systematic distance errors, and Poisson noise), we think that "C3" is part of that same stream. Taken together, the "S_3/C2/C3" stream consists of 97 stars whose spatial distribution shows similarities with the thick-disk overdensity found by Juric et al. (2008) at $(R, z) \approx (9.5, 0.8)$ kpc. We show this in Figure 21, where we have adopted the coordinate system used by Juric et al. (with the x-axis pointing toward the Sun). A comparison to their Figure 27 (left and right panels) reveals an intriguingly similar distribution in the Northern hemisphere plus a counterpart in the Southern hemisphere which—although less prominent—is also mapped by Juric et al. in their Figure 26 (second row, right panel). The (x, y)-distribution in the $z = 600$ pc slice reveals a main clump, whose position matches the rectangular region in the right panel of Juric et al.'s Figure 27. This is to our knowledge the first time that a six-dimensional phase-space overdensity has been first identified by its kinematics. If the similarity with the Juric et al. overdensity is not a coincidence, this would confirm this finding by an independent method. Further, the kinematics of the feature would rule out a ringlike feature of (thick) disk stars, instead supporting either a "localized clumpy overdensity" (Juric et al. 2008) or a spatially coherent stellar stream passing the plane in the northern direction. However, our survey volume is not large enough to distinguish between these two possibilities.

We note that the "S_3/C2/C3" stream is the only stream for which we have found signs of a spatial coherence.

In the most metal-poor subsample s4 ([Fe/H] < -2.0), where the fraction of halo stars is close to 100%, there exists a substantial amount of substructure; it is difficult to identify any smooth component. However, many of the overdensities in Figure 9 consist of only a few stars, and their reality is thus in doubt. We concentrate on a highly significant ($\sigma = 4.8$) feature located at $(V_{\rm az}, V_{\Delta E}, \nu) = (175, 75, 100^\circ)$ and labeled with "C4." In this region of $(V_{\rm az}, V_{\Delta E}, \nu$, [Fe/H]) space, a density enhancement of stars is not expected. The "C4" candidate stream is clumped around $(\nu$, [Fe/H]) $\approx (100^\circ, -2.2)$, which clearly distinguishes it from a smooth feature. Figure 22 shows the metallicity, angular momentum and (U, V, W) distribution of "C4."

The very low eccentricity, $e = V_{\Delta E}/\sqrt{2}V_{\rm LSR} \simeq 0.2$, of "C4" suggests that it belongs to a metal-weak thick disk. However, according to Chiba & Beers (2000) even the metal-weak tail of the thick disk should not contain stars as metal poor as [Fe/H] $\lesssim -2.2$, where the [Fe/H] distribution of "C4" peaks. These authors argued that the fraction of low-eccentricity stars with [Fe/H] $\leqslant -2.2$ remains the same regardless of their height $|z|$, implying that they purely belong to the halo. In addition, stars in the clump "C4" are not distributed symmetrically around $\nu = 90^\circ$, but are centered at an orbital polar angle of roughly 100°, with a longer tail toward higher inclinations.

On the other hand, the formation of the stellar halo and thick disk might underlie a common cause—the accretion of satellite galaxies. It has been shown that the metal-weak tail of the thick disk could consist of tidal debris stemming from a progenitor on a planar orbit that has been circularized prior to disruption through dynamical friction (Quinn et al. 1986, 1993; Abadi et al. 2003). The very low abundances of the "C4" stars favor this scenario. Even if these stars do not belong to a single progenitor exclusively, we have found evidence that tidal debris exists on disklike orbits, giving further support for the hierarchical buildup of the Milky Way and making "C4" the most intriguing of our newly detected streams.

8. CONCLUSIONS

We have used SDSS/SEGUE data from the seventh SDSS public data release to search for halo streams in a 2 kpc sphere centered on the Sun. Using the cataloged values for log g, $g-i$ color, and [Fe/H], together with distance estimates based on the photometric parallax relation from Ivezić et al. (2008), we assembled a sample of 22,321 subdwarfs with [Fe/H] $\leqslant -0.5$, excluding main-sequence turnoff stars. A comparison with fiducial sequences for 12 globular clusters from An et al. (2008) suggests that our distances are accurate to within systematic errors of less than 5%, although they are much less constrained on the high-metallicity end of the photometric parallax relation.

We divided our sample into four subsamples, equally spaced by 0.5 dex in metallicity. Assuming a spherical potential, we searched for stellar streams in each subsample in a space spanned by the quantities $V_{\rm az} = \sqrt{V^2 + W^2}$, $V_{\Delta E} = \sqrt{U^2 + 2(V_{\rm az} - V_{\rm LSR})^2}$, and $\nu = \arctan \frac{V+V_{\rm LSR}}{W}$. These quantities are approximations for a star's azimuthal velocity or angular momentum, eccentricity, and orbital angle with respect to the positive z-axis.

Our basic results can be summarized as follows.

1. Our sample is dominated by stars on disklike orbits; the fraction of these stars with orbital inclinations between 75° and 105° is 81% (80%) for stars with $-1.0 \leqslant$ [Fe/H] < -0.5, 46% (44%) for stars with $-1.0 \leqslant$ [Fe/H] < -0.5, and remains constant at 23% (16%–17%) for all stars more metal poor than [Fe/H] $= -1.5$ (the number in parenthesis gives the fraction of stars on prograde orbits). This implies that beyond [Fe/H] $\simeq -1.5$, the fraction of thick-disk stars remains constant.
2. In the metallicity range $-1.0 \leqslant$ [Fe/H] < -0.5, it is difficult to identify substructure among the thick-disk stars, because the smooth component dominates. As the fraction of thick-disk stars decreases, we detect signals of the stream first described by Arifyanto & Fuchs (2006) and Helmi et al. (2006).
3. We find an overdensity of stars moving with disklike kinematics, but too metal poor to belong to the classical metal-weak thick disk, which should not extend beyond [Fe/H] $\simeq -2.2$ (Chiba & Beers 2000). We interpret this clump, named "C4," as a tidal stream accreted on an orbit in the plane of the protodisk. Halo streams on such orbits are predicted from both numerical simulations of spiral galaxy formation (Quinn et al. 1986, 1993; Abadi et al. 2003) and the considerable (20%) fraction of halo stars on low-eccentricity orbits (Chiba & Beers 2000).
4. We confirm the existence of previously detected halo streams: the "RAVE" stream, which was discovered in data from the first RAVE data release (Paper I), the stream "S_3" found by Dettbarn et al. (2007), which crosses the solar

neighborhood from the direction of the South Galactic Pole on a diagonally retrograde orbit, and the "H99" stream discovered by Helmi et al. (1999) at high angular momentum. The latter is the most significant stream in our sample ($\sigma \approx 12.0$), which explains why Helmi et al. (1999) found it in a sample of only 275 stars. However, even with our much larger sample size the number of stars that belong to this stream is only approximately doubled. This speaks against the conclusion of Helmi et al. (1999) that as much as 10% of the nearby halo stars originated from a single progenitor.

The "S_3" stream lies very close to two other features, which we labeled "C2" and "C3," in ($V_{\rm az}$, $V_{\Delta E}$, ν). Both possess similar kinematics as "S_3," and the small differences could well be explained by the effects of statistical and systematic distance errors and by the way we compute statistical significances, which may lead to adjacent peaks as a stellar stream enhances the number of stars in a certain region of the phase space. The [Fe/H] distributions of "S_3," "C2," and "C3" give strong support for the hypotheses that all three features are one single stream. The composite "S_3/C2/C3" stream shows intriguing similarities in its spatial extent to an overdensity found by Juric et al. (2008) at $(R, z) \approx (9.5, 0.8)$ kpc. If this connection is real, this would be the first time that a six-dimensional coherent phase-space overdensity has been identified by its kinematics alone. Further, because the W velocities are too high for thick-disk stars, we could rule out a ringlike feature in the thick disk as its origin.

The fact that both the "RAVE" and the "S_3/C2/C3" streams have been found in two independent samples makes it very unlikely that they are "false positives." The latter is significant at a level of $\sigma \gtrsim 2.8$ in our data (the "S_3" peak; Figure 11) and in the data from Dettbarn et al. (2007), corresponding to a confidence level of 99.5%. In other words, the probability that this stream is created by chance in both samples is $(0.005)^2 = 0.0025\%$. The significance levels of the "RAVE" stream in the RAVE data and in the SDSS/SEGUE data are $\sigma \gtrsim 3$ (Paper I; Figure 10) and $\sigma \approx 3.0$ (Figure 11), respectively, which also makes it very unlikely that both streams are created through Poisson noise.

5. Besides the already known features, we find evidence of a large amount of substructure, especially in the most metal-poor bins. In particular, we identify one candidate for a genuine halo stream that has not yet been described in the literature. This stream, "C1," moves on highly inclined orbits nearly in the direction toward the north Galactic Pole.
6. We can roughly estimate the fraction of halo stars contained within the streams we detected. To obtain an upper limit, we simply treat all stars as halo stars that lie outside the range $75^\circ < \nu < 90^\circ$ and outside of $V_{\rm az} > 0$, [Fe/H] > -1.0. This results in 4388 stars, of which 53 (1.2%) account for the most well populated peak in our sample, "C2." The "H99" stream, with 21 members, only represents a 0.48% maximum fraction of halo stars. These results are fully consistent with statistical arguments made by Gould (2003) considering the fraction of halo stars in a single stream. He puts an upper limit on the granularity of the halo, concluding that if the halo would be fully composed of kinematically cold stellar streams, then at 95% confidence no single stream could contain more than a 5% fraction of the halo stars.
7. Metallicities are very helpful when it comes to deciding about the origin of a moving group. Our stream candidates exhibit a [Fe/H] distribution with a single peak, indicating that their progenitor had a well defined star-forming epoch.

This study shows the power of current and future large-scale surveys to probe substructure in the solar neighborhood and the Milky Way in general. Extensions of this technique to include additional chemical information, for example, [α/Fe] and [C/Fe] ratios, are being pursued at present.

We thank the anonymous referee for his very thorough report which highly improved our manuscript and contributed to some of our major findings.

Funding for the SDSS and SDSS-II has been provided by the Alfred P. Sloan Foundation, the Participating Institutions, the National Science Foundation, the U.S. Department of Energy, the National Aeronautics and Space Administration, the Japanese Monbukagakusho, the Max Planck Society, and the Higher Education Funding Council for England. The SDSS Web site is http://www.sdss.org/.

The SDSS is managed by the Astrophysical Research Consortium for the Participating Institutions. The Participating Institutions are the American Museum of Natural History, Astrophysical Institute Potsdam, University of Basel, University of Cambridge, Case Western Reserve University, University of Chicago, Drexel University, Fermilab, the Institute for Advanced Study, the Japan Participation Group, Johns Hopkins University, the Joint Institute for Nuclear Astrophysics, the Kavli Institute for Particle Astrophysics and Cosmology, the Korean Scientist Group, the Chinese Academy of Sciences (LAMOST), Los Alamos National Laboratory, the Max-Planck-Institute for Astronomy (MPIA), the Max-Planck-Institute for Astrophysics (MPA), New Mexico State University, Ohio State University, University of Pittsburgh, University of Portsmouth, Princeton University, the United States Naval Observatory, and the University of Washington.

T.C.B. and Y.S.L. acknowledge partial support from grants PHY 02-16783 and PHY 08-22648; Physics Frontier Center/Joint Institute for Nuclear Astrophysics (JINA). P.R.F. acknowledges support through the Marie Curie Research Training Network ELSA (European Leadership in Space Astrometry) under contract MRTN-CT-2006-033481. P.R.F. acknowledges support through the Marie Curie Research Training Network ELSA (European Leadership in Space Astrometry) under contract MRTN-CT-2006-033481.

APPENDIX

PROPERTIES OF STREAM MEMBERS

Table 3 lists the identifications and stellar atmospheric parameters from the SSPP for stars that we have assigned to individual streams. The errors on [Fe/H], $T_{\rm eff}$, and $\log g$ are internal estimates, obtained from averaging of multiple techniques. In the cases of independently observed stars, the results have been averaged. Note that in the current version of the SSPP, the astrophysical parameters have been updated to slightly different values with smaller intrinsic errors than those used in this study which are listed below.

Table 4 lists the SDSS photometry, distance estimates and errors, heliocentric radial velocities, and derived U, V, W used in this study.

Table 3
Putative Members of the Identified Streams: Astrophysical Parameters

STREAM	IAU NAME	PLATE-MJD-FIBER	α (°)	δ (°)	[Fe/H]	$\sigma_{[Fe/H]}$	T_{eff} (K)	$\sigma_{T_{eff}}$ (K)	log g	$\sigma_{log\ g}$
C1	SDSS J003929.56+143550.1	1896-53242-317	9.8731813	14.5972557	−1.532	0.032	5626	37	4.155	0.156
C1	SDSS J004044.06+143713.5	1896-53242-275	10.1835690	14.6204119	−1.821	0.008	4618	89	4.572	0.294
C1	SDSS J004209.94+004735.8	1905-53613-379	10.5414352	0.7932640	−1.643	0.008	4886	136	3.570	0.330
C1	SDSS J004209.94+004735.8	1905-53706-372	10.5414352	0.7932640	−1.888	0.078	4749	43	3.935	0.363
C1	SDSS J011202.72+244140.1	2040-53384-296	18.0113449	24.6944771	−1.457	0.054	5585	32	3.965	0.180
C1	SDSS J012737.07+385706.2	2042-53378-555	21.9044685	38.9517097	−1.209	0.082	5479	75	4.489	0.069
C1	SDSS J012737.07+385706.2	2043-53351-114	21.9044685	38.9517097	−1.345	0.071	5471	69	4.501	0.083
C1	SDSS J012823.46+375742.5	2062-53381-002	22.0977440	37.9618034	−1.417	0.061	5121	50	4.431	0.151
C1	SDSS J013010.48+144140.6	0425-51884-467	22.5436459	14.6946182	−1.435	0.029	5966	53	4.209	0.076
C1	SDSS J013010.48+144140.6	0425-51898-463	22.5436459	14.6946182	−1.572	0.034	5978	48	4.241	0.092
C1	SDSS J013249.36-091356.1	0662-52147-429	23.2056828	−9.2322512	−1.075	0.065	5727	43	4.571	0.031
C1	SDSS J013249.36-091356.1	0662-52178-426	23.2056828	−9.2322512	−1.207	0.029	5610	50	4.425	0.075
C1	SDSS J014657.63-002829.4	1907-53265-101	26.7401257	−0.4748370	−1.128	0.075	4841	92	4.310	0.215
C1	SDSS J014657.63-002829.4	1907-53315-106	26.7401257	−0.4748370	−1.417	0.052	4744	16	4.539	0.068
C1	SDSS J021054.90+224058.0	2046-53327-559	32.7287369	22.6827908	−1.465	0.055	5111	81	4.361	0.115
C1	SDSS J023454.42+285631.8	2442-54065-338	38.7267342	28.9421558	−1.416	0.043	5726	29	4.185	0.125
C1	SDSS J023736.38+261237.9	2399-53764-626	39.4015694	26.2105236	−1.513	0.115	5183	63	4.392	0.053
C1	SDSS J024458.22-003204.3	1664-52965-230	41.2425804	−0.5345300	−1.523	0.111	5475	48	3.884	0.286
C1	SDSS J024458.22-003204.3	1664-52973-230	41.2425804	−0.5345300	−1.774	0.059	5465	41	3.809	0.270
C1	SDSS J025751.30+053706.0	2307-53710-238	44.4637566	5.6183391	−1.851	0.150	5235	118	3.474	0.348
C1	SDSS J025751.30+053706.0	2322-53727-216	44.4637566	5.6183391	−1.706	0.085	5177	86	4.401	0.120
C1	SDSS J032649.09+054858.9	2334-53713-518	51.7045364	5.8163528	−1.622	0.065	5501	53	4.149	0.072
C1	SDSS J032649.09+054858.9	2334-53730-505	51.7045364	5.8163528	−1.557	0.024	5578	59	3.708	0.267
C1	SDSS J060816.47+652237.7	2299-53711-417	92.0686188	65.3771362	−1.337	0.053	5442	22	4.213	0.135
C1	SDSS J081851.60+010153.2	2057-53816-584	124.7150116	1.0314490	−0.992	0.142	5561	105	4.358	0.146
C1	SDSS J084558.30+542552.5	2316-53757-628	131.4929047	54.4312553	−1.616	0.008	5956	28	4.330	0.070
C1	SDSS J085520.23+105431.9	2671-54141-594	133.8342743	10.9088564	−1.569	0.085	5189	50	4.349	0.107
C1	SDSS J094333.81+614255.3	2383-53800-178	145.8908539	61.7153473	−1.606	0.067	4950	52	4.591	0.037
C1	SDSS J102023.87+484211.4	0873-52674-497	155.0994568	48.7031708	−1.260	0.031	5809	39	4.101	0.106
C1	SDSS J102023.87+484211.4	0874-52338-305	155.0994568	48.7031708	−1.218	0.044	5784	23	4.081	0.134
C1	SDSS J103806.73+452054.3	2557-54178-606	159.5280457	45.3484192	−1.458	0.056	4749	78	4.408	0.115
C1	SDSS J113643.00+245755.1	2501-54084-636	174.1791840	24.9653091	−1.354	0.011	5819	24	4.206	0.118
C1	SDSS J124629.08+285028.7	2457-54180-089	191.6211548	28.8413162	−1.849	0.030	5772	40	4.234	0.107
C1	SDSS J124656.06+305644.2	2457-54180-526	191.7335815	30.9456024	−1.418	0.044	5672	39	3.947	0.235
C1	SDSS J144844.46+254959.5	2143-54184-459	222.1852570	25.8332062	−1.696	0.042	5269	27	3.948	0.157
C1	SDSS J150940.61+005724.1	0311-51665-409	227.4191895	0.9567060	−1.183	0.040	5881	3	4.448	0.109
C1	SDSS J160819.86+522800.9	2176-54243-500	242.0827789	52.4669037	−1.217	0.057	5532	42	4.218	0.156
C1	SDSS J162753.45+480813.1	0625-52145-132	246.9727173	48.1369705	−1.973	0.061	5987	28	4.282	0.070
C1	SDSS J164228.88+371457.9	2174-53521-623	250.6203156	37.2494125	−1.626	0.035	6002	58	3.569	0.163
C1	SDSS J164800.02+224725.9	1414-53135-008	252.0000610	22.7905293	−1.948	0.056	6050	29	4.070	0.068
C1	SDSS J174211.76+245806.5	2183-53536-272	265.5490112	24.9684715	−1.526	0.045	5563	57	4.230	0.105
C1	SDSS J233936.27+001812.8	1902-53271-391	354.9011536	0.3035480	−1.552	0.071	5263	46	4.558	0.053
C1	SDSS J234150.16-011412.8	1903-53357-241	355.4590149	−1.2369000	−1.875	0.039	5195	61	3.592	0.447
C1	SDSS J235033.41+371115.7	1880-53262-469	357.6391907	37.1876831	−1.209	0.014	5856	19	4.189	0.084
C2	SDSS J003315.18+083239.6	2312-53709-367	8.3132315	8.5443439	−1.530	0.069	5794	61	4.237	0.103
C2	SDSS J003335.38+064204.8	2327-53710-260	8.3974247	6.7013278	−1.218	0.044	5902	26	4.333	0.098
C2	SDSS J003951.37+241507.1	2038-53327-228	9.9640341	24.2519588	−1.960	0.021	5921	35	4.067	0.066
C2	SDSS J014003.43+224737.3	2044-53327-087	25.0142994	22.7936897	−1.808	0.046	5811	38	3.907	0.232
C2	SDSS J024606.36-011303.6	1664-52965-211	41.5265083	−1.2176800	−1.587	0.059	4992	101	4.396	0.128
C2	SDSS J024606.36-011303.6	1664-52973-203	41.5265083	−1.2176800	−1.428	0.120	5027	75	4.399	0.125
C2	SDSS J024606.36-011303.6	1511-52946-207	41.5265121	−1.2176770	−1.753	0.089	4958	102	4.291	0.215
C2	SDSS J061510.77+634737.4	2299-53711-156	93.7948837	63.7937355	−1.418	0.032	5672	35	3.503	0.262
C2	SDSS J072805.35+363536.8	2053-53446-442	112.0222778	36.5935669	−2.396	0.043	6076	41	3.742	0.142
C2	SDSS J072957.64+404615.9	1734-53034-425	112.4901810	40.7710724	−1.362	0.042	5683	28	4.378	0.081
C2	SDSS J073626.44+215322.5	2078-53378-352	114.1101532	21.8895817	−1.333	0.101	5242	62	4.517	0.056
C2	SDSS J074829.13+234423.8	0927-52577-590	117.1213913	23.7399406	−1.296	0.053	5465	40	4.192	0.205
C2	SDSS J075411.14+344532.4	0756-52577-538	118.5464325	34.7590065	−2.245	0.067	5907	43	4.233	0.124
C2	SDSS J083939.81+064948.7	1298-52964-283	129.9158630	6.8301821	−2.080	0.013	6033	37	4.080	0.037
C2	SDSS J084737.08+070118.2	2317-54152-362	131.9044952	7.0217328	−1.267	0.088	5003	93	4.546	0.040
C2	SDSS J090533.11+432639.5	0831-52294-447	136.3879395	43.4443016	−1.729	0.049	5938	28	4.319	0.081
C2	SDSS J091720.56+020254.3	0473-51929-423	139.3356781	2.0484250	−1.605	0.009	5971	20	4.300	0.127
C2	SDSS J092013.59+284917.4	1937-53388-574	140.0566254	28.8214874	−2.243	0.025	6119	53	4.083	0.066
C2	SDSS J092213.39+225504.1	2304-53762-573	140.5557861	22.9178085	−1.191	0.087	4964	85	4.553	0.050
C2	SDSS J093632.83+473706.4	0834-52316-487	144.1368103	47.6184464	−1.724	0.024	5859	42	3.894	0.056

Table 3
(Continued)

STREAM	IAU NAME	PLATE-MJD-FIBER	α (°)	δ (°)	[Fe/H]	$\sigma_{[Fe/H]}$	T_{eff} (K)	$\sigma_{T_{eff}}$ (K)	log g	$\sigma_{log\ g}$
C2	SDSS J094018.33-003356.5	0476-52314-010	145.0763855	−0.5657040	−1.917	0.039	5883	52	4.319	0.092
C2	SDSS J095506.81+114300.7	1743-53054-144	148.7783813	11.7168503	−1.357	0.050	5959	38	4.349	0.114
C2	SDSS J095908.86+005645.0	0500-51994-087	149.7869110	0.9458360	−1.706	0.083	5584	77	4.303	0.102
C2	SDSS J101455.05+253710.0	2386-54064-034	153.7293854	25.6194496	−0.989	0.114	5263	92	4.419	0.084
C2	SDSS J104621.93+004321.8	2559-54208-362	161.5913849	0.7227150	−1.512	0.053	5425	54	4.594	0.043
C2	SDSS J105039.60-004524.8	2559-54208-050	162.6649933	−0.7568800	−1.520	0.106	4812	31	4.492	0.073
C2	SDSS J105338.83+481716.5	2390-54094-469	163.4117889	48.2879257	−2.126	0.062	5077	65	3.734	0.422
C2	SDSS J105338.83+481716.5	2410-54087-474	163.4117889	48.2879257	−2.261	0.038	5086	70	3.614	0.344
C2	SDSS J105649.28+014446.2	0507-52353-029	164.2053528	1.7461530	−1.713	0.049	5637	35	3.709	0.303
C2	SDSS J111101.99+103838.3	2393-54156-322	167.7583160	10.6439629	−1.216	0.077	5145	49	4.396	0.092
C2	SDSS J113811.21+482056.1	1444-53054-378	174.5467072	48.3489304	−1.244	0.027	5748	47	3.986	0.158
C2	SDSS J115028.60+015703.2	0514-51994-034	177.6191711	1.9508801	−1.749	0.051	5839	43	4.315	0.102
C2	SDSS J122249.57+010247.7	2558-54140-408	185.7065430	1.0465870	−1.305	0.091	4800	68	4.638	0.088
C2	SDSS J124601.97+285517.0	2239-53726-293	191.5082245	28.9213829	−1.606	0.030	6020	36	4.215	0.072
C2	SDSS J124601.97+285517.0	2457-54180-131	191.5082245	28.9213829	−1.738	0.015	6002	35	4.337	0.093
C2	SDSS J152938.97+483843.7	2449-54271-087	232.4123840	48.6454735	−2.367	0.031	5934	91	3.896	0.230
C2	SDSS J161143.97+534352.6	2176-54243-526	242.9332123	53.7312889	−1.712	0.127	4690	82	4.609	0.301
C2	SDSS J161513.53+070012.5	1731-53884-492	243.8063660	7.0034800	−2.150	0.017	5938	44	3.922	0.103
C2	SDSS J161513.53+070012.5	1732-53501-282	243.8063660	7.0034800	−2.245	0.030	5860	60	4.030	0.147
C2	SDSS J163043.32+633133.6	2550-54206-451	247.6804962	63.5260124	−1.173	0.089	5237	95	4.495	0.085
C2	SDSS J172425.97+265121.1	2193-53888-182	261.1082153	26.8558598	−1.885	0.259	4437	72	4.700	0.157
C2	SDSS J220031.01+001657.2	1106-52912-506	330.1292114	0.2825420	−1.313	0.040	5107	64	4.536	0.109
C2	SDSS J223948.41+232244.7	2252-53565-364	339.9516907	23.3790913	−1.742	0.085	4939	87	4.050	0.317
C2	SDSS J223948.41+232244.7	2252-53613-382	339.9516907	23.3790913	−1.848	0.132	4954	79	3.937	0.381
C2	SDSS J224213.28+222015.7	2252-53565-278	340.5553284	22.3376904	−1.693	0.116	5421	98	3.505	0.237
C2	SDSS J224213.28+222015.7	2252-53613-251	340.5553284	22.3376904	−1.547	0.028	5512	54	3.172	0.209
C2	SDSS J224514.28-003350.8	1900-53262-168	341.3094788	−0.5641130	−1.820	0.050	5144	40	3.680	0.381
C2	SDSS J224738.34+234631.6	2261-53612-620	341.9097595	23.7754459	−1.630	0.021	5493	64	3.783	0.325
C2	SDSS J233651.29+462505.0	1886-53237-472	354.2137146	46.4180641	−1.545	0.012	5615	61	3.569	0.073
C2	SDSS J233819.91+000557.3	1902-53271-344	354.5829468	0.0992420	−2.070	0.018	5582	44	3.499	0.285
C2	SDSS J233835.27+075729.9	2622-54095-139	354.6469727	7.9583020	−1.358	0.038	5481	30	4.418	0.098
C2	SDSS J234345.10+002735.9	1487-52964-550	355.9379272	0.4599800	−1.527	0.072	4670	103	4.631	0.217
C3	SDSS J003149.73-004244.2	1134-52644-318	7.9571881	−0.7122680	−1.134	0.074	4813	94	4.580	0.110
C3	SDSS J003542.54+061441.9	2312-53709-123	8.9272423	6.2449832	−1.286	0.064	5517	47	4.363	0.092
C3	SDSS J003609.72-004756.4	1135-53024-095	9.0404949	−0.7989910	−2.043	0.065	5870	63	4.332	0.140
C3	SDSS J003947.76+003919.3	1904-53682-340	9.9490118	0.6553600	−1.758	0.032	5626	49	3.953	0.242
C3	SDSS J003947.76+003919.3	1134-52644-636	9.9490156	0.6553640	−1.959	0.036	5634	80	3.974	0.277
C3	SDSS J003947.76+003919.3	1086-52525-624	9.9490166	0.6553640	−1.965	0.042	5533	54	4.052	0.176
C3	SDSS J004647.08+143012.0	1896-53242-160	11.6961498	14.5033445	−1.646	0.012	6076	47	3.472	0.053
C3	SDSS J014710.34+145458.9	1898-53260-538	26.7930737	14.9163523	−1.092	0.074	5383	38	4.414	0.074
C3	SDSS J021022.12+214531.8	2046-53327-097	32.5921631	21.7588329	−1.638	0.050	5356	31	4.030	0.149
C3	SDSS J022958.15-075952.6	2047-53732-487	37.4922867	−7.9979420	−1.847	0.019	5561	48	3.796	0.257
C3	SDSS J032120.59+060355.3	2334-53713-326	50.3357887	6.0653648	−2.004	0.039	5376	34	3.724	0.271
C3	SDSS J032120.59+060355.3	2334-53730-339	50.3357887	6.0653648	−1.987	0.036	5318	54	3.510	0.274
C3	SDSS J081525.99+362755.8	0892-52378-616	123.8583069	36.4654922	−1.886	0.052	5744	63	4.269	0.056
C3	SDSS J082533.57+182230.9	2271-53726-612	126.3898697	18.3752556	−2.527	0.026	6229	49	3.550	0.294
C3	SDSS J082533.57+182230.9	2273-53709-479	126.3898697	18.3752556	−2.213	0.023	6259	41	3.683	0.270
C3	SDSS J084043.12+095140.2	2573-54061-093	130.1796570	9.8611660	−1.895	0.007	5886	40	4.445	0.108
C3	SDSS J092032.03+231836.5	2290-53727-450	140.1334534	23.3101311	−1.608	0.028	6080	35	4.187	0.112
C3	SDSS J092032.03+231836.5	2291-53714-124	140.1334534	23.3101311	−1.569	0.009	6116	47	4.209	0.124
C3	SDSS J092824.65+064514.5	2382-54169-103	142.1027069	6.7540302	−1.765	0.065	4894	75	3.847	0.316
C3	SDSS J094030.57+381706.9	1276-53035-430	145.1273651	38.2852554	−2.276	0.029	5954	28	3.983	0.082
C3	SDSS J094934.58+001711.5	0267-51608-359	147.3940735	0.2865320	−1.555	0.028	6165	63	3.380	0.140
C3	SDSS J100406.88+060336.0	0996-52641-311	151.0286560	6.0600109	−2.005	0.026	5815	58	4.019	0.134
C3	SDSS J100908.52+013225.0	0502-51957-231	152.2854919	1.5402700	−2.224	0.024	6035	42	4.212	0.064
C3	SDSS J101140.34+354038.8	2387-53770-520	152.9180756	35.6774483	−2.218	0.107	4801	83	3.693	0.340
C3	SDSS J101749.41+404601.6	1357-53034-557	154.4558868	40.7671013	−2.233	0.038	5410	61	3.885	0.208
C3	SDSS J103459.70+082335.9	1240-52734-254	158.7487640	8.3933039	−1.787	0.039	6014	31	4.256	0.111
C3	SDSS J103658.20+163609.3	2594-54177-392	159.2425232	16.6025944	−2.659	0.036	5658	154	3.029	0.441
C3	SDSS J104827.81+005524.0	2389-54213-444	162.1158905	0.9233330	−1.083	0.036	5321	65	3.442	0.115
C3	SDSS J104838.61+005839.4	2389-54213-443	162.1608887	0.9776190	−1.888	0.022	6063	36	4.351	0.140
C3	SDSS J104838.61+005839.4	2409-54210-508	162.1608887	0.9776190	−1.930	0.049	6071	64	4.274	0.118
C3	SDSS J104838.61+005839.4	2559-54208-443	162.1608887	0.9776190	−1.827	0.031	6038	53	4.098	0.044

Table 3
(Continued)

STREAM	IAU NAME	PLATE-MJD-FIBER	α (°)	δ (°)	[Fe/H]	$\sigma_{[Fe/H]}$	T_{eff} (K)	$\sigma_{T_{eff}}$ (K)	log g	$\sigma_{log\ g}$
C3	SDSS J104838.61+005839.4	2569-54234-442	162.1608887	0.9776190	−1.914	0.043	6099	50	4.290	0.121
C3	SDSS J105236.88-004816.8	2389-54213-003	163.1536865	−0.8046550	−0.805	0.088	5343	109	4.614	0.094
C3	SDSS J105236.88-004816.8	2559-54208-002	163.1536865	−0.8046550	−0.808	0.098	5395	26	4.395	0.136
C3	SDSS J105643.51+480559.6	2410-54087-160	164.1813049	48.0998764	−1.513	0.110	5039	104	4.340	0.120
C3	SDSS J124923.70+291857.5	2457-54180-103	192.3487396	29.3159676	−1.395	0.032	5830	42	4.329	0.083
C3	SDSS J160840.68+524221.9	2176-54243-487	242.1694946	52.7060776	−1.484	0.025	5554	30	4.266	0.137
C3	SDSS J161247.16+194440.3	2205-53793-018	243.1965179	19.7445164	−2.100	0.012	5990	41	4.079	0.142
C3	SDSS J161247.16+194440.3	2206-53795-252	243.1965179	19.7445164	−1.982	0.027	6062	33	4.326	0.141
C3	SDSS J171058.39+430326.4	2256-53613-338	257.7432861	43.0573235	−1.501	0.192	4497	101	4.352	0.095
C3	SDSS J172433.72+260332.6	2182-53905-214	261.1405029	26.0590591	−2.267	0.026	4943	151	3.319	0.482
C3	SDSS J204435.17-005117.0	1908-53239-135	311.1465454	−0.8547190	−1.808	0.028	5453	46	3.236	0.179
C3	SDSS J233626.78+100057.5	2622-54095-361	354.1115723	10.0159616	−1.274	0.023	5416	64	3.087	0.252
C3	SDSS J233912.75-004742.7	1902-53271-304	354.8031311	−0.7952000	−1.730	0.048	6029	34	4.075	0.070
C3	SDSS J012450.36+074506.9	2314-53712-483	21.2098351	7.7519059	−1.489	0.020	5620	36	4.109	0.174
C3	SDSS J012450.36+074506.9	2314-53713-483	21.2098351	7.7519059	−1.433	0.054	5638	36	4.102	0.188
C4	SDSS J011441.01+010914.8	0695-52202-414	18.6708698	1.1541060	−2.389	0.011	5799	45	3.691	0.114
C4	SDSS J023158.11+255029.1	2379-53762-460	37.9921417	25.8414059	−2.267	0.064	5907	48	4.052	0.255
C4	SDSS J023435.85-084755.9	2047-53732-024	38.6493759	−8.7988482	−2.055	0.023	6030	40	3.326	0.179
C4	SDSS J024418.33-000947.9	1664-52965-277	41.0763893	−0.1633020	−1.343	0.030	5820	135	4.280	0.215
C4	SDSS J024418.33-000947.9	1664-52973-274	41.0763893	−0.1633020	−1.230	0.044	5926	34	4.376	0.088
C4	SDSS J081918.72+390006.5	2670-54115-522	124.8280106	39.0018082	−0.551	0.106	5452	34	4.516	0.070
C4	SDSS J103649.93+121219.8	1600-53090-378	159.2080383	12.2055120	−3.037	0.047	5938	77	3.355	0.324
C4	SDSS J105230.56+314419.2	2026-53711-213	163.1273499	31.7386761	−2.187	0.012	5835	51	3.852	0.121
C4	SDSS J105424.31+372221.2	2007-53474-120	163.6012878	37.3725662	−2.153	0.014	5492	72	3.848	0.298
C4	SDSS J113626.47+020433.3	0513-51989-118	174.1102905	2.0759060	−2.158	0.027	5927	78	4.116	0.109
C4	SDSS J124342.45+101708.0	1789-54259-475	190.9268799	10.2855501	−2.179	0.034	5850	46	4.232	0.089
C4	SDSS J124615.79-090738.0	2707-54144-050	191.5657806	−9.1272278	−2.059	0.164	4900	11	3.497	0.310
C4	SDSS J142255.29+125353.1	1708-53503-438	215.7303925	12.8980789	−2.537	0.025	5982	60	3.882	0.108
C4	SDSS J143149.30+243552.0	2136-53494-410	217.9554138	24.5977669	−2.051	0.007	5696	40	3.209	0.223
C4	SDSS J151555.14+135708.8	2752-54533-610	228.9797363	13.9524469	−2.601	0.047	6060	54	3.562	0.114
C4	SDSS J151555.14+135708.8	2766-54242-087	228.9797363	13.9524469	−2.723	0.022	5989	68	3.869	0.235
C4	SDSS J163713.47+632122.9	2550-54206-585	249.3061218	63.3563538	−0.532	0.078	5217	107	4.428	0.073
C4	SDSS J174259.25+244823.2	2183-53536-290	265.7468567	24.8064518	−2.150	0.028	5431	40	3.009	0.300
C4	SDSS J200336.15+600006.9	2554-54263-279	300.9006348	60.0019035	−0.441	0.092	4931	88	3.472	0.121
C4	SDSS J211011.44+002324.9	1918-53240-522	317.5476685	0.3902380	−2.143	0.037	5318	41	3.077	0.275
C4	SDSS J215433.88-071000.4	0716-52203-323	328.6411438	−7.1667900	−2.222	0.013	6025	26	4.328	0.095
C4	SDSS J234017.29-003337.6	1902-53271-278	355.0720215	−0.5604550	−1.111	0.099	5457	61	4.511	0.068
C4	SDSS J235651.91-004758.0	0387-51791-247	359.2162781	−0.7994560	−0.741	0.019	5791	6	4.253	0.072
C4	SDSS J235651.91-004758.0	1091-52902-279	359.2162781	−0.7994560	−0.748	0.020	5762	12	4.235	0.118
C4	SDSS J235651.91-004758.0	1489-52991-255	359.2162781	−0.7994560	−0.731	0.022	5786	23	4.204	0.116
H99	SDSS J004500.91+134546.1	1896-53242-129	11.2538118	13.7627974	−2.155	0.037	5855	49	4.353	0.070
H99	SDSS J004606.09+005812.0	1904-53682-563	11.5253792	0.9699940	−1.273	0.049	5602	34	4.184	0.175
H99	SDSS J004755.30+143355.6	1896-53242-109	11.9804010	14.5654478	−1.659	0.049	5194	54	4.076	0.235
H99	SDSS J012316.16-001508.5	0696-52209-172	20.8173447	−0.2523500	−2.168	0.057	5423	59	3.786	0.301
H99	SDSS J014552.75+134648.5	1898-53260-176	26.4698048	13.7801332	−2.168	0.012	5328	73	3.801	0.229
H99	SDSS J014858.66+001851.5	1906-53293-633	27.2444191	0.3143000	−1.913	0.133	4952	70	4.373	0.046
H99	SDSS J015218.06-003227.2	1076-52914-085	28.0752354	−0.5408920	−1.032	0.047	5151	30	4.420	0.130
H99	SDSS J021139.03+060824.3	2306-53726-188	32.9126167	6.1400919	−1.736	0.061	5464	52	4.049	0.205
H99	SDSS J022207.13+011345.2	0406-51817-369	35.5297279	1.2292100	−1.711	0.029	5395	55	3.829	0.341
H99	SDSS J022207.13+011345.2	0406-51869-373	35.5297279	1.2292100	−1.747	0.031	5378	51	3.741	0.368
H99	SDSS J022207.13+011345.2	0406-51876-367	35.5297279	1.2292100	−1.781	0.025	5339	44	3.729	0.358
H99	SDSS J022207.13+011345.2	0406-51900-364	35.5297279	1.2292100	−1.838	0.040	5338	48	3.819	0.369
H99	SDSS J022207.13+011345.2	0406-52238-367	35.5297279	1.2292100	−1.761	0.022	5357	60	3.805	0.353
H99	SDSS J022207.13+011345.2	1558-53271-361	35.5297279	1.2292100	−1.729	0.028	5351	51	3.684	0.366
H99	SDSS J024809.01-005121.7	1664-52965-135	42.0375404	−0.8560400	−1.726	0.031	5813	49	4.320	0.068
H99	SDSS J024809.01-005121.7	1664-52973-137	42.0375404	−0.8560400	−1.723	0.042	5846	44	4.308	0.071
H99	SDSS J081654.87+265422.0	1266-52709-395	124.2286072	26.9061050	−1.999	0.037	6038	25	4.279	0.094
H99	SDSS J092940.69+410552.2	0939-52636-160	142.4195404	41.0978432	−2.217	0.032	5977	67	3.877	0.088
H99	SDSS J101829.06+650218.9	0488-51914-532	154.6210632	65.0385818	−1.870	0.028	5907	31	3.866	0.152
H99	SDSS J103611.02+131457.9	1748-53112-221	159.0458984	13.2494249	−2.193	0.060	5911	74	4.193	0.103
H99	SDSS J111131.57+000336.0	0279-51608-349	167.8815155	0.0599980	−1.515	0.034	5675	50	4.229	0.115
H99	SDSS J111131.57+000336.0	0279-51984-351	167.8815155	0.0599980	−1.476	0.080	5653	55	4.191	0.126
H99	SDSS J125635.48+403725.3	2021-53475-369	194.1478271	40.6236916	−1.668	0.032	5913	51	4.225	0.078
H99	SDSS J163516.45+143604.5	2209-53907-540	248.8185272	14.6012478	−2.297	0.011	5744	34	3.771	0.242

Table 3
(Continued)

STREAM	IAU NAME	PLATE-MJD-FIBER	α (°)	δ (°)	[Fe/H]	$\sigma_{[Fe/H]}$	T_{eff} (K)	$\sigma_{T_{eff}}$ (K)	log g	$\sigma_{log\ g}$
H99	SDSS J172312.11+275319.5	2182-53905-409	260.8004761	27.8887577	−1.855	0.049	5307	79	3.806	0.222
H99	SDSS J211224.90+002453.8	1918-53240-565	318.1037598	0.4149530	−2.154	0.026	6054	31	4.122	0.146
H99	SDSS J211224.91+002453.8	0985-52431-625	318.1037903	0.4149580	−2.124	0.017	6083	40	3.934	0.097
H99	SDSS J211224.91+002453.8	0986-52443-418	318.1037903	0.4149580	−2.249	0.027	6060	30	4.214	0.067
H99	SDSS J211224.91+002453.8	1025-53239-622	318.1037903	0.4149580	−2.364	0.023	6016	45	4.038	0.101
H99	SDSS J211224.91+002453.8	1026-52558-387	318.1037903	0.4149580	−2.100	0.028	6124	37	3.977	0.185
H99	SDSS J211224.91+002453.8	1112-53180-432	318.1037903	0.4149580	−2.156	0.070	6134	47	3.919	0.141
H99	SDSS J211224.91+002453.8	1523-52937-427	318.1037903	0.4149580	−2.091	0.032	6118	22	3.859	0.188
H99	SDSS J222048.55+132527.1	0736-52221-628	335.2022705	13.4241829	−1.477	0.020	5754	18	3.956	0.216
H99	SDSS J224938.70-083003.6	0723-52201-568	342.4112244	−8.5010118	−1.100	0.052	5694	17	4.210	0.134
H99	SDSS J234742.49+000253.1	1902-53271-595	356.9270325	0.0480870	−1.249	0.027	5839	35	4.422	0.087
RAVE	SDSS J013839.30-093045.6	1914-53729-147	24.6637535	−9.5126638	−1.371	0.068	5369	29	4.423	0.106
RAVE	SDSS J013839.30-093045.6	2816-54400-233	24.6637535	−9.5126638	−1.300	0.122	5356	49	4.126	0.243
RAVE	SDSS J013839.30-093045.6	2850-54461-239	24.6637535	−9.5126638	−1.424	0.055	5380	24	4.114	0.231
RAVE	SDSS J014203.92-090422.8	1914-53729-627	25.5163231	−9.0730104	−0.671	0.040	5401	60	4.657	0.026
RAVE	SDSS J014203.92-090422.8	2816-54400-518	25.5163231	−9.0730104	−0.616	0.083	5349	72	4.579	0.036
RAVE	SDSS J014203.92-090422.8	2850-54461-519	25.5163231	−9.0730104	−0.636	0.085	5388	63	4.640	0.039
RAVE	SDSS J014710.87-001335.3	0402-51793-264	26.7952995	−0.2264600	−1.172	0.019	5402	58	2.972	0.187
RAVE	SDSS J014710.87-001335.3	1076-52914-296	26.7952995	−0.2264600	−1.302	0.033	5453	28	3.318	0.147
RAVE	SDSS J014710.87-001335.3	1504-52940-318	26.7952995	−0.2264600	−1.422	0.041	5313	45	2.850	0.111
RAVE	SDSS J015905.74-003222.3	2045-53350-183	29.7739105	−0.5395300	−1.919	0.025	5512	41	4.421	0.083
RAVE	SDSS J015905.74-003222.3	2851-54485-195	29.7739105	−0.5395300	−1.623	0.053	5546	66	3.991	0.185
RAVE	SDSS J033942.37-060709.4	2050-53401-426	54.9265633	−6.1192760	−1.162	0.073	4849	22	4.628	0.069
RAVE	SDSS J082021.79+391100.7	2670-54115-529	125.0907822	39.1835175	−1.684	0.078	5333	40	4.115	0.227
RAVE	SDSS J085211.24+372747.5	2380-53759-343	133.0468292	37.4631844	−0.996	0.055	5655	61	4.040	0.247
RAVE	SDSS J095955.31-002950.1	0268-51633-057	149.9804688	−0.4972440	−1.405	0.041	5506	39	3.415	0.110
RAVE	SDSS J103554.79+454500.5	2567-54179-521	158.9782867	45.7501335	−1.792	0.067	5408	46	3.972	0.278
RAVE	SDSS J103739.10+383729.0	1998-53433-338	159.4129333	38.6247101	−1.483	0.025	5373	40	4.145	0.167
RAVE	SDSS J111311.63-164457.4	2690-54211-029	168.2984467	−16.7492657	−1.899	0.057	5976	38	4.082	0.075
RAVE	SDSS J111434.17+094641.6	2393-54156-496	168.6423645	9.7782183	−0.914	0.055	5066	52	4.408	0.066
RAVE	SDSS J122210.68+002445.2	2568-54153-467	185.5444946	0.4125620	−1.023	0.073	4775	59	4.354	0.078
RAVE	SDSS J123456.17+515326.2	0884-52374-038	188.7340240	51.8906097	−1.108	0.131	5443	77	4.556	0.054
RAVE	SDSS J132647.54+295741.2	2110-53467-247	201.6981049	29.9614429	−2.036	0.053	5504	37	4.357	0.100
RAVE	SDSS J154838.74+445401.8	1333-52782-555	237.1614380	44.9004936	−1.654	0.007	5967	14	4.336	0.103
RAVE	SDSS J212730.72+103653.3	1960-53289-292	321.8780212	10.6148062	−1.265	0.073	5384	43	3.381	0.091
RAVE	SDSS J224018.33-000629.9	1900-53262-269	340.0763855	−0.1082920	−1.423	0.069	5392	53	4.197	0.176
RAVE	SDSS J224616.22+001513.5	1900-53262-557	341.5675964	0.2537480	−1.303	0.040	5679	39	4.321	0.087
RAVE	SDSS J225744.52+061315.4	2310-53710-259	344.4355164	6.2209420	−1.374	0.046	5412	30	3.261	0.145
S3	SDSS J002331.83+005338.6	0390-51816-563	5.8826432	0.8940620	−1.320	0.047	5994	32	3.828	0.106
S3	SDSS J002331.83+005338.6	0390-51900-571	5.8826432	0.8940620	−1.439	0.041	5951	42	3.808	0.082
S3	SDSS J002331.83+005338.6	1088-52929-571	5.8826432	0.8940620	−1.237	0.033	6004	46	3.781	0.095
S3	SDSS J002331.83+005338.6	1118-52559-569	5.8826432	0.8940620	−1.406	0.020	5920	47	3.697	0.092
S3	SDSS J002331.83+005338.6	1119-52581-575	5.8826432	0.8940620	−1.468	0.078	5952	36	3.820	0.091
S3	SDSS J002331.83+005338.6	1120-52589-570	5.8826432	0.8940620	−1.436	0.053	5853	50	3.670	0.130
S3	SDSS J002331.83+005338.6	1121-52873-571	5.8826432	0.8940620	−1.328	0.029	5979	34	3.940	0.151
S3	SDSS J002331.83+005338.6	1122-52876-563	5.8826432	0.8940620	−1.336	0.011	5988	30	3.781	0.109
S3	SDSS J002331.83+005338.6	1492-52932-563	5.8826432	0.8940620	−1.323	0.039	5905	48	3.593	0.071
S3	SDSS J002331.83+005338.6	1542-53734-618	5.8826432	0.8940620	−1.447	0.025	5938	46	3.803	0.099
S3	SDSS J014400.30+231504.1	2044-53327-026	26.0012436	23.2511330	−1.705	0.039	5480	54	4.111	0.214
S3	SDSS J025220.13+335550.4	2378-53759-193	43.0838547	33.9306755	−1.481	0.043	5616	35	4.252	0.179
S3	SDSS J035419.29-045941.0	2051-53738-334	58.5803757	−4.9947348	−1.106	0.049	5839	51	4.368	0.030
S3	SDSS J035419.29-045941.0	2071-53741-365	58.5803757	−4.9947348	−1.098	0.040	5884	49	4.410	0.102
S3	SDSS J063233.61+273645.5	2696-54167-448	98.1400604	27.6126442	−1.603	0.162	4742	88	4.172	0.164
S3	SDSS J071848.45+313202.6	2677-54180-432	109.7018814	31.5340672	−1.018	0.044	5510	75	4.493	0.084
S3	SDSS J072100.85+411425.4	1864-53313-241	110.2535477	41.2403831	−0.924	0.038	5907	24	4.475	0.090
S3	SDSS J073614.44+411329.5	2683-54153-546	114.0601578	41.2248535	−1.502	0.062	5658	55	4.340	0.096
S3	SDSS J084702.66+105403.2	2667-54142-274	131.7610931	10.9008980	−1.650	0.010	5505	28	4.283	0.141
S3	SDSS J090104.49+393309.6	1198-52669-629	135.2687073	39.5526695	−1.532	0.032	5727	55	4.212	0.050
S3	SDSS J092513.14+071055.3	2382-54169-166	141.3047333	7.1820359	−1.901	0.091	5011	71	4.243	0.044
S3	SDSS J111847.11+090301.0	2393-54156-075	169.6963043	9.0502911	−0.885	0.017	5264	48	4.375	0.092
S3	SDSS J170051.55+390528.4	2181-53524-143	255.2147980	39.0912323	−1.244	0.075	5666	43	4.343	0.100
S3	SDSS J180538.01+241532.1	2195-54234-462	271.4083862	24.2589111	−1.902	0.068	4761	50	3.880	0.332
S3	SDSS J215703.65+003723.0	1474-52933-429	329.2651978	0.6230650	−2.485	0.107	4843	125	3.455	0.605
S3	SDSS J224417.24+001749.1	1900-53262-487	341.0718384	0.2969680	−1.797	0.041	4519	97	4.609	0.301

Table 3
(Continued)

STREAM	IAU NAME	PLATE-MJD-FIBER	α (°)	δ (°)	[Fe/H]	$\sigma_{[Fe/H]}$	T_{eff} (K)	$\sigma_{T_{eff}}$ (K)	log g	$\sigma_{log\ g}$
S3	SDSS J224650.01+004000.4	1900-53262-547	341.7084045	0.6667650	−1.387	0.043	4753	48	4.668	0.068
S3	SDSS J230110.77+054925.9	2310-53710-098	345.2948608	5.8238521	−2.464	0.055	5965	47	3.985	0.214
S3C2	SDSS J014430.48+010052.3	1906-53293-522	26.1270161	1.0145240	−1.662	0.122	5002	90	4.377	0.150
S3C2	SDSS J021049.15+064131.3	2306-53726-232	32.7048035	6.6920271	−1.633	0.074	5531	50	3.958	0.227
S3C2	SDSS J024116.14+291410.5	2442-54065-565	40.3172493	29.2362576	−1.727	0.092	4931	69	4.258	0.208
S3C2	SDSS J075917.15+191709.9	1922-53315-180	119.8214569	19.2860889	−1.652	0.027	5917	39	4.309	0.102
S3C2	SDSS J084011.10+130755.4	2426-53795-587	130.0462646	13.1320667	−1.400	0.056	5398	9	4.523	0.062
S3C2	SDSS J085412.39+054042.3	2332-54149-069	133.5516205	5.6784272	−1.351	0.032	5005	57	4.378	0.105
S3C2	SDSS J111556.02+103009.7	2393-54156-531	168.9834290	10.5026827	−1.688	0.012	6044	57	4.301	0.107
S3C2	SDSS J204541.61-050231.6	1916-53269-520	311.4233704	−5.0421152	−1.917	0.038	5977	34	4.384	0.059
S3C2	SDSS J214325.56-001037.6	0990-52465-157	325.8565063	−0.1771210	−2.201	0.031	6229	23	3.933	0.044
S3C2	SDSS J214325.56-001037.6	1030-52914-177	325.8565063	−0.1771210	−2.592	0.084	6154	56	4.049	0.120
S3C2	SDSS J214325.56-001037.6	1108-53227-176	325.8565063	−0.1771210	−2.412	0.032	6167	35	4.005	0.062
S3C3	SDSS J003043.47-002056.2	1134-52644-284	7.6811280	−0.3489460	−1.759	0.017	6055	31	4.359	0.104
S3C3	SDSS J003837.46-001822.8	1133-52993-070	9.6560965	−0.3063290	−1.077	0.048	5585	35	4.139	0.108
S3C3	SDSS J010042.57-010319.3	0395-51783-001	15.1773758	−1.0553480	−1.209	0.043	6029	45	3.793	0.096
S3C3	SDSS J010042.57-010319.3	1083-52520-050	15.1773758	−1.0553480	−1.225	0.023	5892	26	3.718	0.077
S3C3	SDSS J010042.57-010319.3	1497-52886-049	15.1773758	−1.0553480	−1.311	0.029	5889	36	3.735	0.103
S3C3	SDSS J080541.88+065800.1	2056-53463-483	121.4245224	6.9667039	−1.663	0.086	5276	44	4.152	0.203
S3C3	SDSS J083752.33+422801.9	0895-52581-531	129.4680328	42.4672012	−1.163	0.054	5621	31	4.316	0.074
S3C3	SDSS J101409.40+395431.0	1357-53034-194	153.5391846	39.9086037	−1.739	0.020	5980	45	4.249	0.095
S3C3	SDSS J162108.52+010433.3	0346-51693-601	245.2855072	1.0759110	−1.337	0.051	5727	46	4.432	0.061
S3C3	SDSS J213146.48+120942.4	1960-53289-574	322.9436951	12.1617880	−1.520	0.037	5616	27	3.501	0.162

Notes. The last two entries in the bottom of the list are stars that appear in both "S_3" and "C2", and both "S_3" and "C3", respectively. The reason is that our selection criteria for "C2", "C3" and "S_3" show some overlap. Also, we already noted in Section 7.4 and Section 7.6 that a connection between these streams probably exists.

Table 4
Putative Members of the Identified Streams: Photometry and Velocities

STREAM	IAU NAME	u (mag)	g (mag)	r (mag)	i (mag)	z (mag)	d (kpc)	σ_d (kpc)	v_{rad} (km s^{-1})	U (km s^{-1})	V (km s^{-1})	W (km s^{-1})
C1	SDSS J003929.56+143550.1	16.845	15.809	15.329	15.132	15.116	0.708	0.044	−110.1	50.3	−25.0	−57.6
C1	SDSS J004044.06+143713.5	19.647	17.808	16.987	16.655	16.459	0.798	0.032	−112.5	52.0	−30.4	−58.7
C1	SDSS J011202.72+244140.1	18.173	17.193	16.721	16.543	16.501	1.421	0.080	−152.8	115.7	−4.9	−57.8
C1	SDSS J012737.07+385706.2	17.568	16.406	15.943	15.733	15.684	0.966	0.056	−58.15	−106.6	−1.8	−59.9
C1	SDSS J012823.46+375742.5	20.032	18.645	18.039	17.814	17.738	1.933	0.114	−95.7	−52.6	−14.5	−62.5
C1	SDSS J013249.36-091356.1	18.394	17.225	16.781	16.602	16.536	1.712	0.170	59.9	−102.8	−16.3	−57.5
C1	SDSS J014657.63-002829.4	20.847	19.088	18.343	18.044	17.879	1.854	0.107	49.2	−110.2	−2.3	−47.8
C1	SDSS J021054.90+224058.0	19.032	17.664	17.037	16.805	16.738	1.204	0.080	37.4	−144.5	−13.9	−56.8
C1	SDSS J023454.42+285631.8	17.75	16.792	16.363	16.194	16.101	1.397	0.084	−151	106.3	−11.2	−47.9
C1	SDSS J023736.38+261237.9	19.791	18.546	17.96	17.763	17.628	1.973	0.091	17.5	−106.7	−9.9	−40.9
C1	SDSS J024458.22-003204.3	19.081	17.962	17.467	17.276	17.189	1.763	0.124	−14.35	86.1	−11.3	−52.1
C1	SDSS J032649.09+054858.9	18.594	17.534	17.089	16.92	16.892	1.723	0.126	45.95	−7.6	−23.1	−50.9
C1	SDSS J060816.47+652237.7	18.791	17.651	17.139	16.938	16.862	1.615	0.064	−32.5	−117.6	−21.4	−49.3
C1	SDSS J081851.60+010153.2	19.076	17.915	17.525	17.243	17.247	1.997	0.055	66.8	112.7	−21.3	−57.8
C1	SDSS J084558.30+542552.5	17.475	16.569	16.212	16.068	16.037	1.513	0.103	−112.7	32.6	−6.9	−68.4
C1	SDSS J085520.23+105431.9	19.721	18.567	18.008	17.776	17.666	1.982	0.112	26.7	110.1	−12.4	−50.1
C1	SDSS J094333.81+614255.3	19.271	17.862	17.207	16.94	16.808	1.195	0.075	−217.1	171.2	−20.1	−38.5
C1	SDSS J102023.87+484211.4	17.84	16.856	16.431	16.291	16.256	1.554	0.073	5.2	−133.2	−26.6	−47.4
C1	SDSS J103806.73+452054.3	19.208	17.488	16.697	16.422	16.306	0.835	0.069	16.9	−164.4	−6.2	−56.9
C1	SDSS J113643.00+245755.1	18.347	17.336	16.907	16.757	16.72	1.856	0.130	−18.6	20.9	−15.8	−53.8
C1	SDSS J124629.08+285028.7	17.732	16.845	16.453	16.306	16.266	1.445	0.095	−64.3	64.2	−19.6	−51.9
C1	SDSS J124656.06+305644.2	17.078	16.096	15.66	15.504	15.415	0.946	0.058	−70.1	121.0	−24.5	−45.9
C1	SDSS J144844.46+254959.5	19.145	17.989	17.45	17.241	17.13	1.600	0.094	−140.3	−49.4	−13.2	−54.1
C1	SDSS J150940.61+005724.1	17.844	16.901	16.522	16.387	16.397	1.895	0.107	−30.7	51.7	−19.8	−66.4
C1	SDSS J160819.86+522800.9	18.303	17.178	16.669	16.512	16.438	1.374	0.112	−215.5	78.5	−24.8	−60.6
C1	SDSS J162753.45+480813.1	17.027	16.162	15.818	15.703	15.693	1.292	0.083	−222.8	36.8	−32.7	−59.8
C1	SDSS J164228.88+371457.9	17.088	16.199	15.887	15.707	15.661	1.285	0.083	−200.3	22.7	−3.7	−74.4
C1	SDSS J164800.02+224725.9	17.822	16.941	16.589	16.468	16.415	1.777	0.120	−177.2	−13.2	−3.4	−56.7
C1	SDSS J174211.76+245806.5	18.672	17.644	17.204	17	16.931	1.778	0.116	−260	−92.4	−27.7	−52.2

Table 4
(Continued)

STREAM	IAU NAME	u (mag)	g (mag)	r (mag)	i (mag)	z (mag)	d (kpc)	σ_d (kpc)	v_{rad} (km s^{-1})	U (km s^{-1})	V (km s^{-1})	W (km s^{-1})
C1	SDSS J233936.27+001812.8	19.056	17.801	17.24	17.039	16.911	1.476	0.102	−89.3	−82.3	−25.9	−47.6
C1	SDSS J234150.16-011412.8	20.048	18.811	18.173	17.928	17.839	1.761	0.107	−51.6	−12.9	−2.6	−68.9
C1	SDSS J235033.41+371115.7	17.652	16.706	16.308	16.149	16.133	1.502	0.096	−154.9	−102.8	−25.5	−48.6
C2	SDSS J003315.18+083239.6	18.101	17.158	16.805	16.613	16.59	1.759	0.182	−244.7	88.8	−93.5	76.9
C2	SDSS J003335.38+064204.8	18.054	17.061	16.662	16.508	16.488	1.779	0.127	−219.7	7.0	−107.9	70.7
C2	SDSS J003951.37+241507.1	18.137	17.259	16.908	16.777	16.764	1.975	0.113	−248.6	37.7	−74.9	64.1
C2	SDSS J014003.43+224737.3	18.302	17.494	17.072	16.954	16.933	1.982	0.164	−284.7	132.8	−65.4	107.0
C2	SDSS J024606.36-011303.6	19.279	17.883	17.227	16.982	16.849	1.222	0.066	−19.95	−57.6	−109.6	64.1
C2	SDSS J024606.36-011303.6	19.279	17.883	17.227	16.982	16.849	1.183	0.068	−17.4	−56.6	−98.9	60.8
C2	SDSS J061510.77+634737.4	18.381	17.327	16.866	16.664	16.636	1.561	0.072	−233.9	151.7	−78.2	59.4
C2	SDSS J072805.35+363536.8	17.637	16.843	16.542	16.393	16.367	1.701	0.107	20.6	38.7	−77.1	89.6
C2	SDSS J072957.64+404615.9	18.502	17.462	17.037	16.857	16.793	1.887	0.114	111.4	−84.0	−61.2	82.1
C2	SDSS J073626.44+215322.5	19.28	17.977	17.438	17.229	17.127	1.676	0.138	243	−127.3	−70.3	101.6
C2	SDSS J074829.13+234423.8	19.036	17.906	17.4	17.189	17.152	1.842	0.114	263.6	−167.7	−74.2	66.1
C2	SDSS J075411.14+344532.4	17.121	16.243	15.895	15.775	15.7	1.268	0.076	131.9	−67.8	−105.3	69.8
C2	SDSS J083939.81+064948.7	17.43	16.573	16.255	16.104	16.098	1.495	0.079	121.2	129.7	−76.3	69.7
C2	SDSS J084737.08+070118.2	18.739	17.19	16.569	16.277	16.147	0.964	0.063	269.8	−101.9	−79.9	49.1
C2	SDSS J090533.11+432639.5	17.532	16.632	16.237	16.158	16.172	1.591	0.144	159.3	−173.0	−59.9	50.1
C2	SDSS J091720.56+020254.3	17.408	16.571	16.185	16.056	16.027	1.448	0.066	320	−175.3	−64.9	68.7
C2	SDSS J092013.59+284917.4	17.008	16.197	15.9	15.765	15.777	1.377	0.092	128.2	−14.2	−77.0	66.5
C2	SDSS J092213.39+225504.1	19.352	17.699	17.051	16.748	16.629	1.206	0.093	259.5	−150.6	−74.2	88.0
C2	SDSS J093632.83+473706.4	17.65	16.745	16.386	16.276	16.237	1.722	0.117	−22.2	68.0	−99.7	72.1
C2	SDSS J094018.33-003356.5	18.044	17.169	16.816	16.657	16.632	1.846	0.123	286.5	−127.1	−65.6	58.0
C2	SDSS J095506.81+114300.7	16.954	15.984	15.606	15.479	15.474	1.219	0.105	181	33.5	−75.8	67.1
C2	SDSS J095908.86+005645.0	18.673	17.697	17.273	17.092	17.012	1.935	0.143	255.8	−28.7	−90.5	63.5
C2	SDSS J101455.05+253710.0	19.442	18.033	17.534	17.281	17.166	1.794	0.155	202.4	−127.4	−74.1	72.8
C2	SDSS J104621.93+004321.8	18.732	17.526	17.035	16.848	16.749	1.551	0.130	228.4	78.1	−84.5	80.7
C2	SDSS J105039.60-004524.8	19.866	18.249	17.527	17.244	17.1	1.260	0.044	265.4	−188.8	−66.0	69.7
C2	SDSS J105338.83+481716.5	19.716	18.422	17.792	17.508	17.368	1.337	0.053	79.8	−164.7	−66.6	50.4
C2	SDSS J105649.28+014446.2	18.816	17.806	17.358	17.143	17.079	1.788	0.127	247.1	8.4	−97.4	83.5
C2	SDSS J111101.99+103838.3	19.354	18.097	17.517	17.29	17.33	1.641	0.148	167.4	169.8	−76.2	87.8
C2	SDSS J113811.21+482056.1	18.549	17.557	17.104	16.934	16.937	1.990	0.143	45.1	−132.1	−61.4	59.2
C2	SDSS J115028.60+015703.2	17.476	16.629	16.263	16.125	16.06	1.419	0.095	202.2	35.1	−90.2	62.8
C2	SDSS J122249.57+010247.7	18.865	17.033	16.269	15.988	15.801	0.727	0.061	199.2	114.0	−92.1	60.8
C2	SDSS J124601.97+285517.0	17.059	16.194	15.842	15.733	15.737	1.351	0.097	70.25	−112.1	−68.6	77.5
C2	SDSS J152938.97+483843.7	18.045	17.067	16.794	16.61	16.573	1.890	0.224	−145	9.9	−104.8	72.3
C2	SDSS J161143.97+534352.6	19.465	17.707	16.894	16.585	16.458	0.831	0.023	−180.1	143.7	−87.3	50.4
C2	SDSS J161513.53+070012.5	16.542	15.658	15.332	15.207	15.155	1.003	0.056	−31.95	35.4	−100.9	75.5
C2	SDSS J163043.32+633133.6	18.503	17.143	16.608	16.387	16.306	1.143	0.077	−189.9	149.7	−64.6	75.0
C2	SDSS J172425.97+265121.1	21.473	19.181	18.201	17.845	17.655	1.066	0.025	−199.4	−12.1	−93.2	59.9
C2	SDSS J220031.01+001657.2	18.092	16.612	15.991	15.775	15.682	0.802	0.044	−163.2	173.5	−49.3	73.2
C2	SDSS J224514.28-003350.8	19.582	18.27	17.688	17.395	17.275	1.437	0.061	−172.9	167.9	−52.1	59.1
C2	SDSS J224738.34+234631.6	19.528	18.587	18.049	17.807	17.864	1.981	0.227	−309.7	−23.3	−79.9	101.3
C2	SDSS J233651.29+462505.0	18.4	17.417	17.003	16.795	16.786	1.775	0.114	−335.9	128.2	−79.2	86.2
C2	SDSS J233819.91+000557.3	18.492	17.555	17.102	16.9	16.847	1.501	0.101	−214.2	−127.8	−89.5	58.4
C2	SDSS J233835.27+075729.9	18.685	17.534	17.038	16.829	16.725	1.482	0.093	−245.7	−6.1	−61.9	91.6
C2	SDSS J234345.10+002735.9	20.884	19.152	18.333	18.006	17.826	1.500	0.044	−200	−165.4	−79.9	53.5
C3	SDSS J003149.73-004244.2	19.951	18.106	17.405	17.121	16.948	1.349	0.056	−225.4	40.1	−10.7	144.0
C3	SDSS J003542.54+061441.9	15.83	14.652	14.174	14.019	13.909	0.462	0.039	−207.5	−73.5	−35.6	126.8
C3	SDSS J003609.72-004756.4	17.972	17.123	16.789	16.619	16.554	1.816	0.115	−229.7	77.8	−30.8	133.8
C3	SDSS J003947.76+003919.3	18.479	17.432	16.99	16.765	16.706	1.435	0.085	−204.9	−38.1	−24.2	133.9
C3	SDSS J003947.76+003919.3	18.479	17.432	16.99	16.765	16.706	1.406	0.097	−210.7	−34.9	−23.2	140.2
C3	SDSS J003947.76+003919.3	18.479	17.432	16.99	16.765	16.706	1.417	0.079	−209.6	−35.9	−24.0	138.8
C3	SDSS J004647.08+143012.0	17.39	16.474	16.133	15.974	15.954	1.409	0.111	−244.3	90.1	−4.6	123.3
C3	SDSS J012450.36+074506.9	18.715	17.674	17.205	17.045	16.972	1.936	0.106	−184.6	−36.0	−21.3	141.0
C3	SDSS J014710.34+145458.9	18.969	17.748	17.229	17.015	16.965	1.640	0.122	−269.8	179.6	−17.8	110.4
C3	SDSS J021022.12+214531.8	17.186	16.138	15.625	15.444	15.347	0.760	0.039	−283.4	167.1	−20.1	127.5
C3	SDSS J022958.15-075952.6	18.252	17.291	16.803	16.624	16.558	1.325	0.072	−138.7	98.8	−9.2	114.0
C3	SDSS J032120.59+060355.3	17.996	16.927	16.396	16.188	16.165	0.956	0.042	−9.95	−87.1	−4.8	120.9
C3	SDSS J081525.99+362755.8	16.983	16.069	15.684	15.523	15.494	0.986	0.038	193.3	−112.4	−54.9	130.3
C3	SDSS J082533.57+182230.9	17.006	16.184	15.906	15.773	15.784	1.406	0.141	243.9	−111.4	−12.3	121.2
C3	SDSS J084043.12+095140.2	17.733	16.952	16.584	16.444	16.358	1.625	0.107	217.5	−2.6	−56.3	129.2
C3	SDSS J092032.03+231836.5	17.562	16.782	16.417	16.316	16.319	1.747	0.148	253.9	−143.7	−9.5	119.2

Table 4
(Continued)

STREAM	IAU NAME	u (mag)	g (mag)	r (mag)	i (mag)	z (mag)	d (kpc)	σ_d (kpc)	v_{rad} (km s^{-1})	U (km s^{-1})	V (km s^{-1})	W (km s^{-1})
C3	SDSS J092824.65+064514.5	19.166	17.633	16.888	16.612	16.491	0.855	0.040	169.8	106.3	−14.5	141.7
C3	SDSS J094030.57+381706.9	17.43	16.608	16.238	16.122	16.137	1.380	0.075	64.6	79.7	−32.3	131.0
C3	SDSS J094934.58+001711.5	17.74	16.853	16.522	16.403	16.38	1.951	0.158	281.7	−118.8	−17.1	116.4
C3	SDSS J100406.88+060336.0	18.322	17.471	17.1	16.927	16.868	1.849	0.141	281.8	−117.5	−27.5	126.4
C3	SDSS J100908.52+013225.0	16.839	16.019	15.686	15.55	15.512	1.095	0.085	227.3	49.1	−21.2	132.3
C3	SDSS J101140.34+354038.8	19.622	18.046	17.298	16.974	16.82	0.894	0.019	200.3	−128.8	−20.7	127.2
C3	SDSS J101749.41+404601.6	19.029	17.96	17.462	17.263	17.149	1.619	0.094	61	67.5	−10.7	118.9
C3	SDSS J103459.70+082335.9	17.285	16.431	16.074	15.964	15.933	1.472	0.110	257.9	−82.8	−37.5	124.6
C3	SDSS J103658.20+163609.3	19.262	18.701	18.132	17.969	17.935	1.985	0.214	219.5	−33.1	−7.5	141.7
C3	SDSS J104827.81+005524.0	19.054	17.716	17.197	17.012	16.898	1.844	0.106	261.9	−103.5	−4.0	137.3
C3	SDSS J104838.61+005839.4	17.467	16.663	16.3	16.184	16.212	1.539	0.150	227	11.2	−1.0	126.3
C3	SDSS J105236.88-004816.8	19.407	18.166	17.642	17.427	17.409	1.989	0.136	271.7	−69.0	−25.5	141.5
C3	SDSS J105643.51+480559.6	20.535	18.923	18.319	18.068	17.983	1.960	0.128	74.9	−18.1	−23.9	121.4
C3	SDSS J124923.70+291857.5	17.79	16.82	16.437	16.254	16.252	1.550	0.104	104.8	−162.3	−47.0	114.7
C3	SDSS J160840.68+524221.9	18.45	17.345	16.871	16.694	16.644	1.538	0.078	−99	−23.3	−32.8	123.4
C3	SDSS J161247.16+194440.3	17.582	16.791	16.463	16.345	16.289	1.739	0.126	−28.6	13.1	−34.1	123.7
C3	SDSS J171058.39+430326.4	20.343	18.35	17.408	17.03	16.819	0.781	0.022	−90.1	76.7	−15.4	130.8
C3	SDSS J172433.72+260332.6	19.787	18.311	17.585	17.305	17.161	1.078	0.031	−101.4	12.4	−18.0	125.8
C3	SDSS J204435.17-005117.0	17.366	16.374	15.913	15.767	15.664	0.979	0.029	−317.8	−184.0	−10.6	106.3
C3	SDSS J233626.78+100057.5	18.29	17.188	16.708	16.508	16.413	1.433	0.156	−262.3	83.3	−11.9	142.8
C3	SDSS J233912.75-004742.7	16.962	16.075	15.722	15.571	15.563	1.102	0.080	−240.4	−8.6	−34.0	129.9
C4	SDSS J011441.01+010914.8	17.393	16.515	16.125	15.997	15.905	1.193	0.118	31.4	−40.0	179.6	−26.2
C4	SDSS J023158.11+255029.1	17.304	16.462	16.044	15.936	15.889	1.176	0.070	20.3	1.0	162.1	−68.6
C4	SDSS J023435.85-084755.9	17.447	16.566	16.224	16.133	16.099	1.616	0.171	62.6	−24.4	160.5	−43.9
C4	SDSS J024418.33-000947.9	17.013	16.067	15.712	15.597	15.563	1.061	0.080	−14.05	29.8	183.0	6.0
C4	SDSS J081918.72+390006.5	19.515	18.108	17.576	17.397	17.367	1.582	0.089	−37.9	41.7	172.6	−18.3
C4	SDSS J103649.93+121219.8	16.452	15.58	15.248	15.12	15.085	0.880	0.057	−35.3	69.0	178.7	−36.6
C4	SDSS J105230.56+314419.2	17.532	16.631	16.268	16.135	16.069	1.396	0.100	−29.9	32.7	182.3	−21.5
C4	SDSS J105424.31+372221.2	18.669	17.667	17.175	16.974	16.891	1.392	0.065	−23	−3.6	176.1	−27.0
C4	SDSS J113626.47+020433.3	17.444	16.59	16.286	16.135	16.039	1.552	0.118	−38	67.7	177.6	−62.4
C4	SDSS J124342.45+101708.0	17.175	16.307	15.964	15.779	15.707	1.101	0.070	−27.5	27.9	158.0	−42.2
C4	SDSS J124615.79-090738.0	20.739	19.415	18.747	18.442	18.307	1.988	0.073	−10.6	11.6	159.9	−47.3
C4	SDSS J142255.29+125353.1	16.902	16.075	15.766	15.626	15.629	1.189	0.059	−8.5	66.2	179.6	−27.3
C4	SDSS J143149.30+243552.0	18.603	17.571	17.179	17.027	16.983	1.876	0.147	−32.4	50.2	167.4	−28.8
C4	SDSS J151555.14+135708.8	17.522	16.656	16.338	16.217	16.214	1.569	0.109	7	63.0	188.0	−11.2
C4	SDSS J163713.47+632122.9	18.845	17.223	16.6	16.43	16.292	0.897	0.050	−53.7	27.8	168.1	−5.8
C4	SDSS J174259.25+244823.2	19.035	17.94	17.46	17.24	17.152	1.534	0.086	−66.4	−21.7	178.8	−29.8
C4	SDSS J200336.15+600006.9	17.922	15.798	15.035	14.784	14.675	0.325	0.005	−50.1	24.5	177.2	−3.5
C4	SDSS J211011.44+002324.9	17.282	16.24	15.715	15.512	15.447	0.672	0.026	−30.6	−27.5	163.3	−55.2
C4	SDSS J215433.88-071000.4	16.756	15.911	15.572	15.438	15.375	1.045	0.051	−32.7	−56.9	164.7	−39.0
C4	SDSS J234017.29-003337.6	17.895	16.573	16.051	15.861	15.804	0.788	0.031	−11.3	61.0	176.6	−8.5
H99	SDSS J004500.91+134546.1	17.999	17.122	16.724	16.587	16.528	1.550	0.117	173.4	−9.2	183.0	−244.7
H99	SDSS J004606.09+005812.0	18.223	17.114	16.648	16.475	16.417	1.466	0.107	150.7	98.0	170.3	−213.1
H99	SDSS J004755.30+143355.6	19.062	17.865	17.266	17.019	16.877	1.236	0.071	140.6	21.1	156.6	−237.9
H99	SDSS J012316.16-001508.5	18.753	17.818	17.341	17.144	17.102	1.594	0.105	199.4	40.9	144.0	−258.3
H99	SDSS J014552.75+134648.5	18.248	17.193	16.659	16.434	16.339	1.012	0.056	161.6	5.9	143.8	−255.8
H99	SDSS J014858.66+001851.5	19.806	18.348	17.689	17.428	17.302	1.347	0.074	201.2	4.7	146.2	−245.4
H99	SDSS J015218.06-003227.2	19.016	17.602	16.974	16.738	16.663	1.254	0.060	201.5	13.1	153.1	−245.6
H99	SDSS J021139.03+060824.3	18.527	17.468	16.954	16.748	16.688	1.331	0.067	177.3	50.4	153.9	−271.1
H99	SDSS J022207.13+011345.2	17.876	16.733	16.17	15.981	15.868	0.836	0.053	203.18333	19.3	147.7	−264.1
H99	SDSS J081654.87+265422.0	16.326	15.514	15.165	15.038	15.05	0.893	0.048	−109.5	11.2	159.2	−245.4
H99	SDSS J092940.69+410552.2	16.417	15.544	15.241	15.106	15.082	0.995	0.102	−215.8	31.7	110.7	−272.4
H99	SDSS J101829.06+650218.9	17.452	16.552	16.151	16.069	16.021	1.434	0.113	−278.4	67.5	122.6	−280.9
H99	SDSS J103611.02+131457.9	17.782	16.979	16.65	16.533	16.489	1.897	0.111	−181.5	−22.0	145.3	−269.4
H99	SDSS J125635.48+403725.3	17.742	16.86	16.523	16.388	16.36	1.825	0.163	−224	2.2	192.6	−217.3
H99	SDSS J163516.45+143604.5	18.338	17.466	17.066	16.92	16.888	1.733	0.078	−149.6	32.5	184.1	−239.3
H99	SDSS J172312.11+275319.5	16.936	15.826	15.309	15.122	15.073	0.628	0.033	−170.4	68.7	136.1	−270.5
H99	SDSS J211224.90+002453.8	17.287	16.491	16.168	16.073	16.046	1.640	0.083	78.1	13.6	118.1	−284.8
H99	SDSS J211224.91+002453.8	17.287	16.491	16.168	16.073	16.046	1.627	0.086	82.12	16.0	122.2	−284.7
H99	SDSS J222048.55+132527.1	18.432	17.371	16.947	16.792	16.725	1.815	0.105	96.8	107.6	143.4	−241.3
H99	SDSS J224938.70-083003.6	18.356	17.261	16.814	16.671	16.625	1.861	0.106	203.9	80.8	205.9	−227.8
H99	SDSS J234742.49+000253.1	17.74	16.806	16.417	16.248	16.201	1.566	0.111	181.4	−94.1	107.0	−274.3

Table 4
(Continued)

STREAM	IAU NAME	u (mag)	g (mag)	r (mag)	i (mag)	z (mag)	d (kpc)	σ_d (kpc)	v_{rad} (km s^{-1})	U (km s^{-1})	V (km s^{-1})	W (km s^{-1})
RAVE	SDSS J013839.30-093045.6	18.762	17.655	17.127	16.964	16.859	1.606	0.102	−82.4	−61.8	56.5	97.2
RAVE	SDSS J014203.92-090422.8	18.646	17.313	16.802	16.656	16.551	1.649	0.144	−136.4	48.0	50.8	115.9
RAVE	SDSS J015905.74-003222.3	19.221	18.192	17.691	17.499	17.421	1.914	0.133	−118.1	40.1	59.5	91.0
RAVE	SDSS J033942.37-060709.4	19.042	17.363	16.661	16.397	16.288	1.011	0.064	18.9	−57.4	77.5	82.0
RAVE	SDSS J082021.79+391100.7	18.864	17.739	17.207	16.989	16.905	1.411	0.094	79.1	−29.2	79.0	79.7
RAVE	SDSS J085211.24+372747.5	18.707	17.627	17.127	16.971	16.918	1.984	0.153	103.3	−27.1	48.9	101.7
RAVE	SDSS J095955.31-002950.1	18.681	17.519	17.048	16.858	16.752	1.685	0.106	180	−47.2	75.5	98.7
RAVE	SDSS J103554.79+454500.5	19.487	18.355	17.815	17.562	17.52	1.729	0.130	92.7	−29.7	32.6	113.4
RAVE	SDSS J103739.10+383729.0	18.388	17.214	16.672	16.434	16.356	1.123	0.066	97.8	−18.9	52.8	98.3
RAVE	SDSS J111311.63-164457.4	17.117	16.199	15.821	15.671	15.626	1.166	0.072	176.1	−23.5	70.6	99.0
RAVE	SDSS J111434.17+094641.6	17.686	16.196	15.548	15.341	15.3	0.659	0.050	149.9	39.9	68.4	105.9
RAVE	SDSS J122210.68+002445.2	20.363	18.655	17.925	17.666	17.482	1.790	0.182	156.3	45.1	69.8	100.6
RAVE	SDSS J123456.17+515326.2	18.722	17.496	17.032	16.836	16.776	1.707	0.155	38.5	−32.6	48.9	99.8
RAVE	SDSS J132647.54+295741.2	19.199	18.169	17.68	17.465	17.434	1.819	0.117	59.2	−37.6	84.8	87.8
RAVE	SDSS J154838.74+445401.8	16.761	15.899	15.529	15.428	15.402	1.161	0.073	−23.9	39.5	55.9	101.7
RAVE	SDSS J212730.72+103653.3	17.878	16.667	16.153	15.989	15.918	1.107	0.072	−184.9	−15.4	54.3	90.8
RAVE	SDSS J224018.33-000629.9	18.206	17.102	16.582	16.388	16.325	1.178	0.079	−171.4	50.2	48.1	102.3
RAVE	SDSS J224616.22+001513.5	17.428	16.419	15.987	15.762	15.718	1.039	0.054	−165.6	22.0	57.6	92.6
RAVE	SDSS J225744.52+061315.4	17.105	15.917	15.409	15.189	15.11	0.708	0.043	−203.1	−0.4	31.0	104.4
S3	SDSS J014400.30+231504.1	18.543	17.495	16.981	16.774	16.676	1.352	0.072	−151.7	−86.9	−61.3	108.6
S3	SDSS J025220.13+335550.4	17.326	16.299	15.839	15.682	15.636	1.007	0.053	−33.6	−132.7	−28.8	96.7
S3	SDSS J035419.29-045941.0	17.211	16.268	15.896	15.763	15.778	1.469	0.093	−118.8	171.5	−39.3	89.7
S3	SDSS J063233.61+273645.5	19.76	18.389	17.672	17.455	17.295	1.274	0.041	173.9	−118.6	−53.3	98.3
S3	SDSS J071848.45+313202.6	19.187	17.994	17.531	17.227	17.135	1.990	0.165	215.8	−156.6	−60.2	80.9
S3	SDSS J072100.85+411425.4	16.833	15.797	15.398	15.243	15.234	1.053	0.079	111.7	−81.2	−33.7	101.5
S3	SDSS J073614.44+411329.5	17.405	16.369	15.959	15.817	15.722	1.225	0.085	−12.7	62.6	−45.2	100.1
S3	SDSS J084702.66+105403.2	18.282	17.279	16.799	16.6	16.491	1.365	0.084	158.9	60.3	−53.6	102.6
S3	SDSS J090104.49+393309.6	18.056	17.082	16.684	16.505	16.417	1.618	0.110	−2.2	108.6	−50.4	95.7
S3	SDSS J092513.14+071055.3	19.042	17.683	17.07	16.789	16.697	1.039	0.046	303.6	−187.4	−28.2	88.7
S3	SDSS J111847.11+090301.0	19.593	18.237	17.628	17.404	17.329	1.896	0.070	220.5	−42.0	−52.7	107.5
S3	SDSS J170051.55+390528.4	16.809	15.751	15.333	15.132	15.08	0.814	0.066	−88.9	135.0	−35.6	95.2
S3	SDSS J180538.01+241532.1	19.25	17.712	16.962	16.65	16.511	0.839	0.033	−75.4	153.4	−34.0	96.4
S3	SDSS J215703.65+003723.0	20.247	18.72	17.934	17.579	17.36	1.109	0.034	−180.2	160.7	−51.2	90.9
S3	SDSS J224417.24+001749.1	18.236	16.323	15.453	15.098	14.923	0.360	0.011	−187.5	144.3	−22.4	91.3
S3	SDSS J224650.01+004000.4	19.254	17.516	16.738	16.436	16.299	0.882	0.042	−226.9	76.3	−45.3	103.1
S3	SDSS J230110.77+054925.9	17.747	16.999	16.642	16.52	16.504	1.683	0.162	−238.4	70.5	−37.8	101.7
S3C2	SDSS J014430.48+010052.3	18.443	16.953	16.301	16.034	15.9	0.727	0.039	−183.3	75.8	−63.4	101.4
S3C2	SDSS J021049.15+064131.3	18.334	17.235	16.786	16.539	16.449	1.256	0.068	−176.5	73.5	−72.6	90.9
S3C2	SDSS J024116.14+291410.5	19.415	18.037	17.357	17.137	17.002	1.260	0.067	−155.1	−2.8	−72.8	86.9
S3C2	SDSS J075917.15+191709.9	18.188	17.235	16.879	16.723	16.694	1.972	0.106	241.7	−114.7	−65.6	84.7
S3C2	SDSS J084011.10+130755.4	18.854	17.7	17.174	16.948	16.869	1.483	0.087	307.7	−184.6	−52.9	73.8
S3C2	SDSS J085412.39+054042.3	20.205	18.708	18.048	17.784	17.674	1.771	0.111	305.7	−138.6	−59.7	91.8
S3C2	SDSS J111556.02+103009.7	15.635	14.821	14.475	14.344	14.35	0.691	0.095	185.2	90.8	−69.9	91.5
S3C2	SDSS J204541.61-050231.6	18.002	17.164	16.814	16.666	16.569	1.863	0.102	−282.1	−91.7	−66.5	93.5
S3C2	SDSS J214325.56-001037.6	17.174	16.345	16.014	15.927	15.875	1.465	0.108	−310.66667	−174.2	−52.8	82.8
S3C3	SDSS J003043.47-002056.2	18.002	17.161	16.8	16.679	16.669	1.992	0.144	−161.2	−148.6	−20.0	103.3
S3C3	SDSS J003837.46-001822.8	18.259	17.074	16.605	16.414	16.378	1.503	0.154	−222.5	173.8	−44.7	96.6
S3C3	SDSS J080541.88+065800.1	18.949	17.745	17.212	16.995	16.876	1.398	0.085	303	−160.2	−28.8	103.7
S3C3	SDSS J083752.33+422801.9	18.252	17.205	16.752	16.541	16.54	1.527	0.112	162.9	−120.8	−44.4	106.8
S3C3	SDSS J101409.40+395431.0	17.446	16.601	16.246	16.118	16.123	1.554	0.126	59.9	64.8	−44.5	111.0
S3C3	SDSS J162108.52+010433.3	17.746	16.693	16.282	16.112	16.045	1.378	0.137	80.8	112.0	−36.2	112.1
S3C3	SDSS J213146.48+120942.4	17.96	16.916	16.465	16.299	16.225	1.354	0.083	−306.5	−102.7	−46.6	106.1

Notes. The last two entries in the bottom of the list are stars that appear in both "S_3" and "C2," and both "S_3" and "C3," respectively. The reason is that our selection criteria for "C2," "C3," and "S_3" show some overlap. Also, we already noted in Sections 7.4 and 7.6 that a connection between these streams probably exists.

REFERENCES

Abadi, M. G., Navarro, J. F., Steinmetz, M., & Eke, V. R. 2003, ApJ, 597, 21
Abazajian, K., et al. 2009, ApJS, in press (arXiv:0812.0649)
Allende Prieto, C., et al. 2008, AJ, 136, 2070
An, D., et al. 2008, ApJS, 179, 326
Antoja, T., Figueras, F., Fernández, D., & Torra, J. 2008, A&A, 490, 135
Arifyanto, M. I., & Fuchs, B. 2006, A&A, 499, 533
Binney, J., & Tremaine, S. 1987, Galactic Dynamics (Princeton: Princeton Univ. Press)
Bochanski, J. J. 2008, PhD Thesis, Univ. Washington
Brook, C. B., Kawata, D., & Gibson, B. K. 2004, in ASP Conf. Ser. 327, Satellites and Tidal Streams, ed. F. Prada, D. Martinez-Delgado, & T. Mahoney (San Francisco, CA: ASP), 100
Carollo, D., et al. 2007, Nature, 450, 1020
Chereul, E., & Grenon, M. 2001, in ASP Conf. Ser. 228, Dynamics of Star Clusters and the Milky Way, ed. S. Deiters et al. (San Francisco, CA: ASP), 398
Chiba, M., & Beers, T. C. 2000, AJ, 119, 2843
Choi, J.-W., Weinberg, M. D., & Katz, N. 2007, MNRAS, 381, 987
Clem, J.-L., Vanden Berg, D. A., & Stetson, P. B. 2008, AJ, 135, 682
De Silva, G. M., et al. 2007, AJ, 133, 694
De Simone, R., Wu, X., & Tremaine, S. 2004, MNRAS, 350, 627
Dehnen, W. 1998, AJ, 115, 2384
Dehnen, W. 2000, AJ, 119, 800
Dekker, E. 1976, Phys. Reports, 24, 315
Dettbarn, C., Fuchs, B., Flynn, C., & Williams, M. 2007, A&A, 474, 857
Dinescu, D. I. 2002, in ASP Conf. Ser. 265, ω Centauri, A Unique Window into Astrophysics, ed. F. van Leeuwen, J. D. Hughes, & G. Piotto (San Francisco, CA: ASP), 365
Duquennoy, A., & Mayor, M. 1991, A&A, 248, 485
Eggen, O. J. 1996, AJ, 112, 1595
Famaey, B., Jorissen, A., Luri, X., Mayor, M., Udry, S., Dejonghe, H., & Turon, C. 2004, A&A, 430, 165
Finlator, K., et al. 2000, AJ, 120, 2615
Fukugita, M., et al. 1996, AJ, 111, 1748
Fux, R. 2001, A&A, 373, 511
Girardi, L., Bressan, A., Bertelli, G., & Chiosi, C. 2000, A&AS, 141, 371
Girardi, L., Grebel, E. K., Odenkirchen, M., & Chiosi, C. 2004, A&A, 422, 205
Gould, A. 2003, ApJ, 592, L63
Grillmair, C. J., & Dionatos, O. 2006, ApJ, 641, L37
Gunn, J. E., et al. 1998, AJ, 116, 3040
Gunn, J. E., et al. 2006, AJ, 131, 2332
Harris, W. E. 1996, AJ, 112, 1487
Helmi, A., & de Zeeuw, P. T. 2000, MNRAS, 319, 657
Helmi, A., Navarro, J. F., Nordström, B., Holmberg, J., Abadi, M. G., & Steinmetz, M. 2006, MNRAS, 365, 1309
Helmi, A., & White, S. D. M. 1999, MNRAS, 307, 495
Helmi, A., White, S. D. M., de Zeeuw, P. T., & Zhao, H. 1999, Nature, 402, 53
Hogg, D. W., Finkbeiner, D. P., Schlegel, D. J., & Gunn, J. E. 2001, AJ, 122, 2129
Holmberg, J., Flynn, C., & Portinari, L. 2006, MNRAS, 367, 449
Ivezić, Ž., et al. 2001, AJ, 122, 2749
Ivezić, Ž., et al. 2003, Mem. Soc. Astron. Ital., 74, 978
Ivezić, Ž., et al. 2008, ApJ, 684, 287
Juric, M., et al. 2008, ApJ, 673, 864
Kalnajs, A. J. 1991, in Dynamics of Disc Galaxies, ed. B. Sundelius (Göteborg: Göteborg Univ.), 323
Kepley, A. A., et al. 2007, AJ, 134, 1579
Klement, R. 2009, Stellar Phase-Space Structure and Dynamics in the Solar Neighbourhood: Kinematic Studies of Nearby Stars (Suetwestdeutscher: Verlag)
Klement, R., Fuchs, B., & Rix, H. W. 2008, ApJ, 685, 261
Lada, C. J. 2006, ApJ, 640, L63
Lee, Y. S., et al. 2008a, AJ, 136, 2022
Lee, Y. S., et al. 2008b, AJ, 136, 2050
Lindblad, B. 1925, ApJ, 62, 191
Lupton, R. H., et al. 2002, Proc. SPIE, 4836, 350
Mayor, M. 1972, A&A, 18, 97
Munn, J. A., Monet, D. G., & Levine, S. E. 2008, AJ, 136, 895
Navarro, J. F., Helmi, A., & Freeman, K. C. 2004, ApJ, 601, L43
Odenkirchen, M., et al. 2001, ApJ, 548, L165
Peñarrubia, J., Benson, A. J., Martínez-Delgado, D., & Rix, H. W. 2006, ApJ, 645, 240
Pier, J. R., et al. 2003, AJ, 125, 1559
Proctor, R. A. 1869, R. Soc. London Proc. Ser. I, 18, 169
Quillen, A. C., & Minchev, I. 2005, AJ, 130, 576
Quinn, P. J., & Goodman, J. 1986, ApJ, 309, 472
Quinn, P. J., et al. 1993, ApJ, 403, 74
Re Fiorentin, P., Helmi, A., Lattanzi, M. G., & Spagna, A. 2005, A&A, 439, 551
Sellwood, J. A., & Binney, J. J. 2002, MNRAS, 336, 785
Soubiran, C., Bienaymé, O., & Siebert, A. 2003, A&A, 398, 141
Tucker, D. L., et al. 2006, Astron. Nachr., 327, 821
Vandenberg, D. A., & Clem, J. L. 2003, AJ, 126, 778
Yanny, B., et al. 2009, AJ, 137, 4377
York, D. G., et al. 2000, AJ, 120, 1579